TRANSPORT, REACTION MECHANISM, AND HYSTERESIS STUDIES OF IRON-BASE CONVERSION FLUORIDES

by

JONATHAN KAIWEI KO

A Dissertation submitted to the

Graduate School-New Brunswick

Rutgers, The State University of New Jersey

in partial fulfillment of the requirements

for the degree of

Doctor of Philosophy

Graduate Program in the Materials Science and Engineering

written under the direction of

Professor Glenn G. Amatucci

and approved by

_____

_____

_____

_____

New Brunswick, New Jersey

January, 2015

ABSTRACT OF THE DISSERTATION

Transport, Reaction Mechanism, and Hysteresis Studies of Iron-base Conversion Fluorides

By JONATHAN KAIWEI KO

Dissertation Director:
Professor Glenn G. Amatucci

Iron-base metal fluorides have been a particular interest as a positive electrode material in Li-ion batteries because of their high energy density and lower cost than commercial intercalation materials. During lithiation, these materials undergo a conversion reaction forming two separate phases, LiF and reduced Fe. Near theoretical capacities are reached when these materials are made into nanocomposites. However, they experience a capacity fade with low cycling rates. In addition, it is not clear on the reaction pathway these materials take during lithiation and delithiation as well as the large hysteresis in its cycling profile. This thesis investigate three candidate materials, FeF_2, FeF_3, and $FeO_{0.67}F_{1.33}$ by looking at the ionic and electronic transport, reaction mechanism, and hysteresis and link them to their electrochemical performance.

Previous studies indicated a percolated structure of Fe^0-LiF forming during lithiation. However, there was not quantitative proof that the network of Fe^0 was electronically supporting. During the course of the study, it was discovered how surprisingly high it was conductive that it led to new testing that utilized its conductive properties.

Acknowledgment

I would like to thank my Ph.D thesis advisor, Prof. Glenn Amatucci for his guidance over the past four years. He has not only provided an opportunity to do my research but has allowed me to have hands-on experience with a variety of specialized instruments at the Energy Storage Research Group (ESRG). From reviewing my manuscripts to discussing future work, Prof. Amatucci has been a great mentor to me. Words cannot express my gratitude for him and his perseverance for high quality work. I would like show my appreciation to my thesis committee members, Prof. Lisa Klein, Prof. Stephen Garofalini, and Prof. Martha Greenblatt.

I would like to thank the current and past staff members of ESRG, Dr. Aurelien Dupasquier, Dr. Nathalie Pereira, Ms. Irene Plitz, Ms. Fadwa Badway, Ms. Anna Halajko, Ms. Linda Sung, Mr. John Gural, Mr. Barry Vanning for their support and assistance in the research group. I would like to thank the current and past graduate students, Dr. William Yourey, Dr. Andrew Gmitter, Dr. Matthew Parkinson, Dr. Kimberly Scott, Mr. James Kantor, Mr. Anthony Ferrer, Mr. Joshua Kim, and Mr. Nicholas Faenza. I've enjoyed the many discussions we had, friendly and technical. Also thanks to our current and past undergraduate students, Charlie, Mike, Sheel, Greg, and Matt. Without their help around the lab, most of the research in our group would have taken much longer to complete.

I would like to extend my gratitude to our talented machinist, J. Gural and B. Vanning. Gural helped with the in-situ cell design used for electrochemical lithiation. He

has machined out parts and even created a small custom contact tab which required both delicate work and precision to make. Vanning has helped in both as a machinist and an electrician specialist. From making circuit boards or wiring up test leads to money weeks long machining out intricate designs on masks for deposition, Vanning has the knowledge and skills to perform any tasks.

I would like to acknowledge my housemates and friends in the Piscataway area, Achalanka, Jess, and Joseph, for their encouragement and conversations we had over a shared meal.

I would like to thank my girlfriend, Shanna Li, for standing by me all this time. Though we are both dedicated to our own work, we manage to spare some time to spend with each other. From the long trips we take to see each other to long conversations over the phone, she has helped me along the way.

I acknowledge the U.S. Government and the Northeastern Center for Chemical Energy Storage (NECCES), an Energy Frontier Research Center funded by the U.S. Department of Energy, Office of Science, Office of Basic Energy Sciences under Award Number DE-SC0001294, for their financial support.

All work of Chapter 3 was originally published as “Transport, Phase Reactions, and Hysteresis of Iron Fluoride and Oxyfluoride Conversion Electrode Materials for Lithium Batteries,” J. K. Ko, K. M. Wiaderek, N. Pereira, T. L. Kinnibrugh, J. R. Kim, P. J. Chupas, K. W. Chapman, and G. G. Amatucci. *ACS Appl. Mater. Interfaces* 2014, **8**, 10858-10869. <http://dx.doi.org/10.1021/am500538b>. Wiaderek, Kinnibrugh, Chupas,

and Chapman provided the PDF analysis of the physical structure change of iron (II) fluoride during delithiation. Pereira contributed the iron oxyfluoride materials. Kim provided EMS electrolytes for high temperature experiments.

Chapter 4 was submitted to *J. Electrochem. Soc.* in September, 2014, as "Electronic Transport in Lithiated Iron and Bismuth Fluoride," authored by J. K. Ko, A. Halajko, M. F. Parkinson, and G. G. Amatucci. Halajko contributed films made by thermal evaporation. Parkinson contributed iron (II) fluoride films during the initial stages of this work.

The work in Chapter 5 has yet to be submitted for publication as of October, 2014. M. F. Parkinson contributed iron (II) fluoride films during the initial stages of this work.

Dedication

I would like to dedicate this thesis to my parents, Chen and Suk-yee Ko, for their love and support to me and my siblings. They have always encouraged us to pursue our own career and that they would support us no matter what direction we take. I am thankful for the many excuses they come up with to come and visit me. They are always worried more about my well-being over their own. Because of this, I would not have gotten this far without their help.

Table of Contents

List of Tables

List of Figures

1 Introduction

With the increase of telecommunications, portable electronics have been incorporated to daily life. Tablets and phones enable access to information on the World Wide Web without being tethered to any single location. With higher demand in portable electronics, there have been higher specification requirements: faster processor, bigger screen, more memory, and longer battery life. None of these technologies can be achieved without a medium to store usable energy. Rechargeable secondary batteries have been the choice over primary batteries because of their life-cycle cost ($/kWh) and higher power output (W). One of the famous secondary battery that is still used in automotive is the lead-acid battery developed by Raymond Faston Planté in 1860. Li-ion batteries have risen because their higher energy density and higher cell voltage. As shown in Figure 1.1, lithium-ion batteries are light weight and small size compare to other secondary batteries. Li metal batteries are rarely used as secondary batteries because of safety issues as it would be explain later. In addition, Li-ion batteries have a longer shelf life with up to 5 – 10 years as oppose to conventional rechargeable (3 - 6 months). [1] [2]

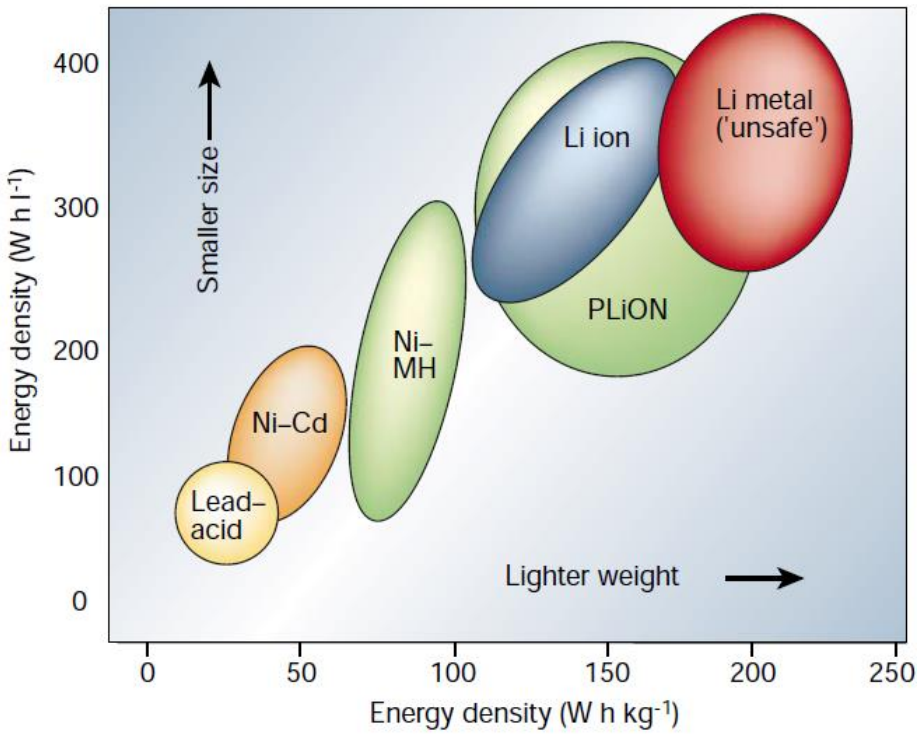

Figure 1.1. Comparison of different secondary batteries in terms of volumetric and gravimetric energy density. Reprinted by permission from Macmillan Publishers Ltd: [Nature] Ref. [1], Copyright (2001).

1.1 *Battery Components*

A battery is the energy storage device that converts chemical energy to usable electrical energy through electrochemical oxidation-reduction (redox) reactions. It contains several electrochemical cells that are connected in series/parallel to increase the operating potential or increase capacity of the battery.

Electrochemical cells consist of an anode and cathode electrode that is separated by a separator and electrolyte. Anode is where oxidation occurs and electrons flow out. Cathode is where reduction occurs, electrons flow into the cathode where the reactant is reduced. The electrolyte is an ionic conductor but electronically insulating

material and most importantly, nonreactive with either anode or cathode. Typically, it is a liquid with dissolved salts, acids, or alkalis and is soaked in a separator that also separates the anode from the cathode. Alternatively, there are solid electrolytes that do not require a separator. Under normal operation, electrons and ions separate from the reactant and ions flow through the electrolyte while electrons travel through an external circuit. In a galvanic cell when the cell is under a load, the negative electrode is the anode and the positive electrode is the cathode. In an electrolytic cell the roles are reverse, as electrons are driven in the opposite direction, the positive electrode is the anode and the negative electrode is the cathode. Figure 1.2 is an example of an electrochemical cell.

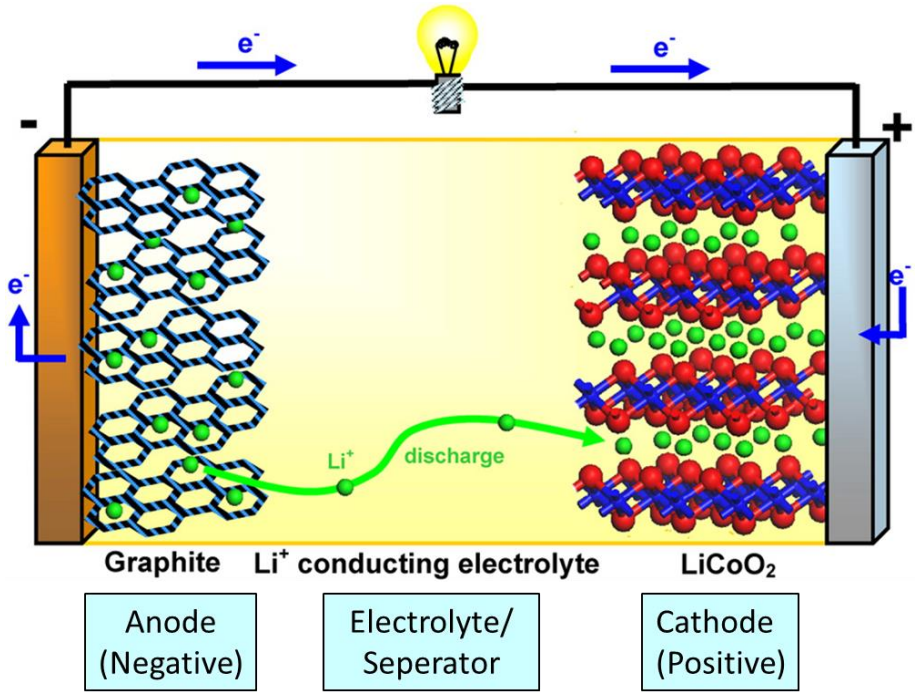

Figure 1.2. A typical electrochemical cell. Adapted from Solid State Ionics, 179, P. G. Bruce, Energy storage beyond the horizon: Rechargeable lithium batteries , 752-760, Copyright (2008), with permission from Elsevier. [3]

In this depiction, a Li-ion cell is under a load and the anode is Li_xC_6 Graphite and $LiCoO_2$ is the cathode. The reaction mechanism is as follows:

$$LiC_6 \rightarrow Li_{1-x}C_6 + xLi^+ + xe^- \qquad \text{Anode}$$

$$Li_{1-x}CoO_2 + xLi^+ + xe^- \rightarrow LiCoO_2 \qquad \text{Cathode}$$

$$LiC_6 + Li_{1-x}CoO_2 \rightarrow Li_{1-x}C_6 + LiCoO_2 \qquad \text{Overall}$$

In secondary batteries, an electrode can be the anode and cathode depending on if the cell is charging or discharging. Thus, they are referred as the negative and positive electrode, where the negative and positive electrode are the anode and cathode respectively during discharge. The standard potential of a cell is determine by the active materials. Gibbs free energy (G) is related to the cell potential by the following equation:

$$\Delta G^0 = -nFE^0 \qquad \textbf{(1.1)}$$

G^0 is the free energy at standard state, n is the number of moles of electrons transfer, F is Faraday's constant, and E^0 is the cell potential in which there is no current flow. A positive cell potential will have a negative change in Gibbs free energy. When E^0 is positive, the reaction is spontaneous in which when a load is applied, useable energy can be extracted from the cell. When E^0 is negative, the reaction is non-spontaneous. This is base off of the free energy potential for any given reaction: [2]

$$\Delta G^0 = -RTln\left(\frac{a_{Products}}{a_{reactants}}\right) \quad \textbf{(1.2)}$$

R is the universal gas constant, T is the absolute temperature, a is the active of species that when ΔG^0 is negative, the reaction will push forward to for products without the need of extra energy. When ΔG^0 is positive, work will need to be put into the system to drive the reaction forward. In a battery, ΔG^0 is determined by the half-cell reactions in both the anode and cathode. As an example, consider a Daniell cell consisting of 2 half cells where copper cathode and zinc anode metal electrodes are immersed in a solution of copper sulfate and zinc sulfate respectively. The cell potential is found as such:

$Zn_{(s)} \rightarrow Zn^{2+}_{(aq)} + 2e^-$ G=-147.005 kJ (0.7618 V) Anode

$Cu^{2+}_{(aq)} + 2e^- \rightarrow Cu_{(s)}$ G=-65.610 kJ (0.340 V) Cathode

$Zn_{(s)} + Cu^{2+}_{(aq)} \rightarrow Zn^{2+}_{(aq)} + Cu_{(s)}$ G=-212.615 kJ (1.1018 V) Overall

1.2 *Negative electrode*

Ideally lithium metal would be use as the positive electrode to use in a lithium battery. It is the lightest and most electropositive. However lithium is an alkali metal which is highly reactive and flammable. This makes it a huge safety concern when used in a battery thus have been limited to coin cells for low power portable electronics and primary batteries. Another concern is its reactivity with the electrolyte and morphological changes during charge and discharge. When lithium is deposited onto the negative electrode during charge, it forms a mossy and sometimes dendritic structures

on the surface of the electrode. This is caused by the random orientation of the particles and non-uniformity charge distribution. This formation will increase the surface area which will increase the non-uniformity of the electrode. After several cycles of lithium stripping and replating, these structures break off and become isolated. In other cases, it can grow until it touches the positive electrode causing a short-circuit in the battery. Instead of electrons flowing through the external circuit, it flows through the electrolyte and directly to the positive electrode. Heat is generated and can cause the battery to expand through gaseous reactions or catch on fire. As lithium is being consumed during discharge, new lithium surfaces are exposed and are then passivated with a mossy layer film during charge when lithium is redeposited onto the surface. The mossy layer that forms makes some of the lithium areas electrochemically inert. Thus, 3 – 5 times of the normal amount of lithium is required to maintain decent cyclability. [2] Despite these shortcomings, much research is devoted in preventing the formation of dendrites. N. Balsara developed a polyethylene oxide (PEO) based copolymer electrolyte that is hard enough to mechanically stop dendrite growth. [4] However, the electrolyte needed to be at elevated temperature in order to get acceptable conductivities. Ding et al. proposed a self-healing electrostatic shield (SHES) to prevent dendritic growth using a non-Li additive. [5] By applying a potential higher than the reduction potential of the additive but slightly lower than Li, the additive will absorb onto the dendrite tip essentially shielding it from Li deposition. However, this is has a limited current rate. High applied current may induce a large voltage drop which may cause both additive and Li-ions to deposit onto the surface reducing the effectiveness. [6]

Lithiated carbon (LiC_6) has been the safe alternative negative electrode for lithium-ion batteries. Lithium ions (Li-ions) are still used but under the idea of the "rocking-chair" method. [7] The electrodes would contain structures that can accommodate Li-ions and that no lithium metal is ever formed at either site. Its chemical potential is nearly the same as lithium metal. Thus, the electrochemical cell will be able to maintain the same high open-circuit voltage without much compromise. Graphitic carbons can accommodate one lithium atom to 6 carbons atoms and will stack interplanar to graphene sheets, as shown in Figure 1.3. It also have a small volume change (<9%) when fully lithiated. This is beneficial to a cell by providing minimal expansion and contraction. An electrode with a large volume change can cause huge amounts of stress and strain on the material during cycling. This can lead to particle fracture which is a loss in capacity and ultimately battery failure. In addition to graphitic carbons, there are carbon materials that are non-graphitic with different crystallinity. Generally there are two main types: soft carbons and hard carbons. Soft carbons are considered to have relatively low crystallinity such as carbon black and acetylene black. These are formed from heat-treating petroleum and coal. Coke-type carbons are soft carbons with intermediate crystallinity. Because of the low ordering these materials they cannot accommodate the same amount of lithium as graphitic carbons. Thus, their theoretical capacities are generally lower. However, they can be doped with nitrogen, boron, or phosphorus which will increase their capacities to the same level as graphitic carbons. Hard carbons such as glassy carbon are made from heat-treating organic polymer materials. They have been shown to have higher capacities than graphitic

carbons. [8] Several models were proposed to explain this increase of capacity. Some suggested the lithium is being absorbed on both sides of the graphene sheet, or that Li-ions are accumulating at the edges and surfaces. Another difference with hard carbons is that is has a sloping voltage profile from 1 V to 0 V instead of a flat profile from 0.3 V to 0 V as seen with other carbon materials. This can greatly lower the overall potential of the cell. In addition, it has a high irreversible loss in capacity and a risk of lithium metal depositing on the surface during charge. [9] Regardless, one of the major advantages is that it can be used with propylene carbonate (PC) which normally would lead to gas formation around 1 V in graphitic carbon. [7] In all cases of lithiated carbon, there is a irreversible loss on the first cycle which can vary between carbon type. [10] This is from electrolyte decomposition and forming a solid electrolyte interface (SEI) layer. After this layer is formed, the second and subsequent cycles remain the same giving a near 100% reversibility. One of the major issues of using lithiated carbon is its small capacity compare to lithium metal (Table 1.1). This has led many researchers into developing a safer yet high capacity negative electrode. [11] [12] [13]

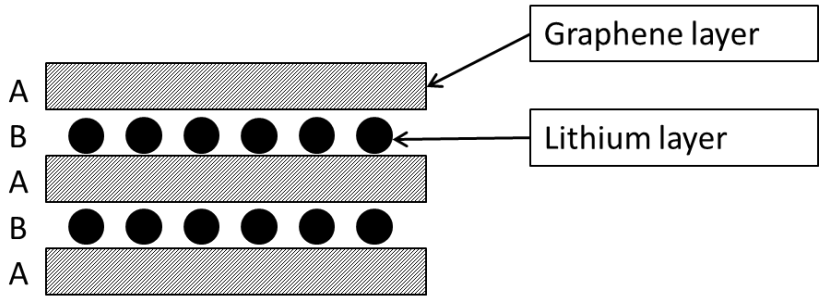

Figure 1.3. Lithium stack between the graphene layers. Adapted with permission from Ref. [14].

Negative electrode material	Voltage range vs lithium (V)	Theoretical capacity (Ah/g)
Li metal	0.0	3.86
$Li_{0.5}C_6$ (coke)	0.0-1.3	0.185
LiC_6	0.0-0.1	0.372

Table 1.1. Voltage and theoretical capacity of some negative electrodes. [2]

1.3 *Electrolyte*

Choosing a good electrolyte is important in a lithium-ion battery as it provides a medium for ions to flow through but block electrons. A decent electrolyte should have the following characteristics [2] [14]:

- Good ionic conductivity (> 10^{-3} S/cm) to lower ohmic polarization
- A lithium ion transference number approaching unity to limit concentration polarization
- Large voltage stability range to prevent electrolyte decomposition
- Thermal stability
- Non-reactive to other cell components
- Low vapor pressure

In addition, it would be ideal that they are low toxicity and low cost. Because lithium is reactive to water, nonaqueous electrolytes are used. In addition, they have

better charge retention and have a larger range temperature change then aqueous electrolyte. Some nonaqueous solvents used in electrochemistry are as follows [9]:

1. Ethers

   Diethyl ether, dimethoxyethene, tetrahydrofuran, and 1-3 dioxolane.

2. Esters

   methyl formate, methyl and ethyl acetate.

3. Alkyl carbonates

   Cyclic carbonates such as ethylene and propylene carbonate, as well as linear carbonates such as dimethyl and diethyl carbonate.

4. Inorganic Solvents

   Sulfer oxide, thionychloride, and sulfuryl chloride.

5. Miscellaneous

   Acetonitrile, nitromethane, dimethyl sulfoxide, and sulfolane.

2, 4, and 5 are typically ignored because of the limited electrochemical windows, electrode surface reactivity, and the lack of electrode passivity. Ethers are also a problem because they tend to oxidize at low potentials. Alkyl carbonates have been the most promising solvent. They are chosen because of their acceptable anodic stability above 5 V. This is important as positive electrode such as $LiNiO_2$, $LiCoO_2$, and $LiMn_2O_4$ may reach to 4.5 V. A typical electrolyte is $LiPF_6$ salt dissolved in a mixture of ethylene carbonate and dimethyl carbonate (EC and DMC). EC has a high dielectric constant which is beneficial in dissolving lithium salts. However, it also has a high viscosity which

can have a negative impact on ionic conductivity as it puts resistance in ion mobility. Thus, it is mix with DMC which has a low viscosity and a lower melting temperature. [2] [15] The transport of ions can be express as the transport (t^+) and transference (T^+) numbers. In reality, transport number is not normally used as it only determines the net charge carried by the cation (Li^+) over the total charge carried by both cations and anions. Transference number takes into account the amount of drag on ion mobility. This is determined by the following equation:

$$T_{Li^+}^{+} = \frac{R_0}{\frac{\Delta V}{I_\infty} - R_{ct}} \quad \textbf{(1.3)}$$

Where R_0 is the bulk resistance, ΔV is the polarization voltage, I_∞ is steady state current after polarization, and R_{ct} is the charge-transfer resistance. [16]

In addition, temperature also affects ionic conductivity. Vogel-Tamman-Fulcher (VTF) type equation is used to determine conductivities of solvents at different temperature ranges [16]:

$$K = \frac{A}{\sqrt{T}} \exp\left(-\frac{E_a}{R}\frac{1}{T - T_0}\right) \quad \textbf{(1.4)}$$

Where K is conductivity, A is a constant, T is temperature, E_a is the activation energy, R is the gas constant, and T_0 is the glass transition temperature. The plot usually shows a convex shape with increasing temperature. Though higher temperatures increase conductivity, it is important to note that all materials in the electrochemical cell must be thermally stabile at those temperature ranges. [17]

1.4 *Positive Electrode*

Most commercial batteries typically contain intercalation materials ($LiCoO_2$, $LiNiO_2$, $LiMn_2O_4$) as a positive electrode of a secondary battery. On discharge, lithium is inserted into the host structure without changing its crystal structure. Even though their lattice may expand from insertion, their structure remains the same. While they provide excellent reversibility, they exhibit a limited capacity. At "true" theoretical capacity, the structure only allows one electron transfer per transition metal. In addition, the amount of accessible energy is only a fraction of its true capacity. On the other hand, conversion materials can have up to four times the typical capacity found in intercalation materials by utilizing all of the metal's redox potential and reducing it to its pure metal state. Unlike intercalation materials, lithium is reacts with the host material to for two new phases during discharge, a lithium salt and a reduced metal. Both types of cathodes are depicted in Figure 1.4. [18]

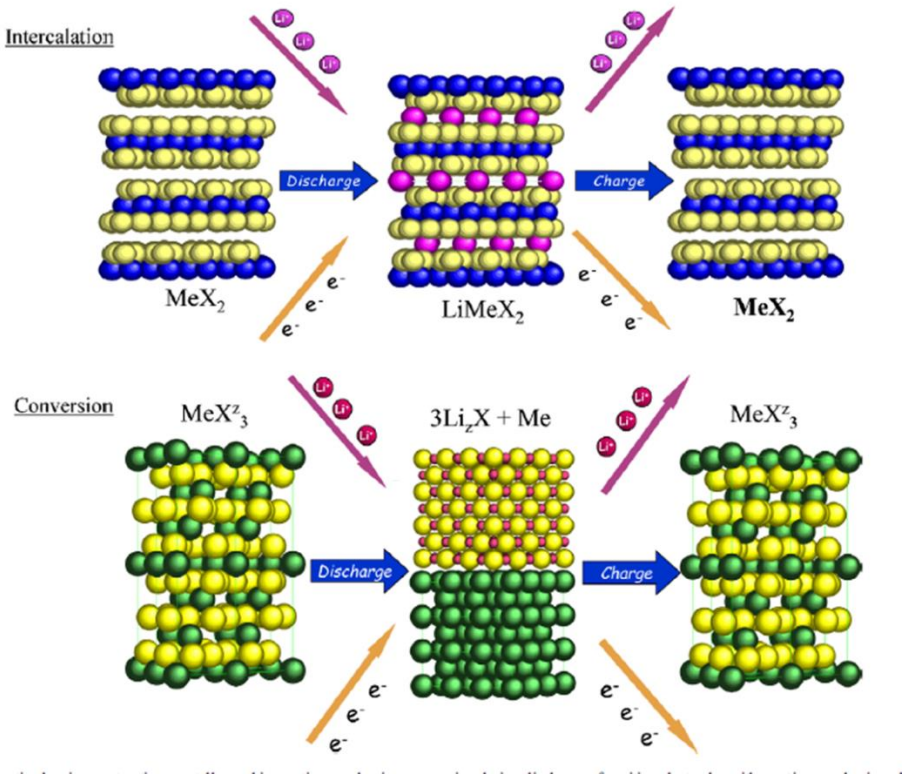

Figure 1.4. Illustration of the structural change during lithiation/delithiation in Intercalation and conversion compounds. Reprinted from Journal of Fluorine Chemistry, 128, G. G. Amatucci, N. Pereira, Fluoride based electrode materials for advanced energy storage devices, 243-262, Copyright (2007), with permission from Elsevier. [18]

1.5 *Intercalation material*

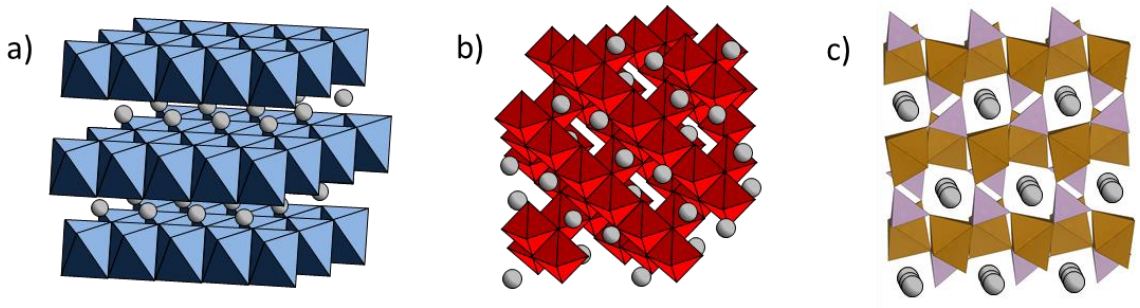

Figure 1.5. Structure of common positive intercalation electrodes materials. (a) layered, (b) spinel, (c) olivine. (a) and (b) were adapted with permission from Ref. [19]. Copyright (2011) American Chemical Society. (c) was made in VESTA software.

There are three main types of intercalation compounds utilized commercially: layered ($LiCoO_2$, $LiNiO_2$), spinel ($LiMn_2O_4$), and olivine ($LiFePO_4$). Crystal structures of all three can be seen in Figure 1.5. Layered structures have planes of alternating lithium-cation sheets and metal oxide-anion sheets. The structure proves a reversible insertion and removal of Li-ions easily from the planes. $LiCoO_2$ is an attractive material because of the strong covalently bonded CoO_2 layers that provide fast lithium-ion diffusion. In addition, the edges that the CoO_6 octahedrals share allow Co-Co interaction which provides good electronic mobility. This allows the material to achieve high current rate potentials. Co has a high oxidization level which allows $LiCoO_2$ to achieve a high chemical potential. However, only half of the theoretical capacity of $LiCoO_2$ could be utilized. Cobalt is expensive and toxic. This can become difficult when looking to scale-up for large battery applications such as electric vehicles. Furthermore, $LiCoO_2$ can decompose and generate oxygen at elevated temperatures. This can be a concern as it will react with organic electrolyte generating heat and combust. [20] [21]

In the interest on finding inexpensive and environmentally benign materials, $LiMn_2O_4$ spinel stood out as a possible candidate. Its operating voltage is higher than $LiCoO_2$ (4 V) and is more stable as little oxygen is produce during decomposition at elevated temperatures. [21] Its practical capacity is similar to $LiCoO_2$. The strong edge-shared octahedral Mn_2O_4 allows lithium to be inserted and extracted at the tetrahedral site without the collapse of the structure. It is possible to insert a second lithium atom into the structure effectively making a disorder tetragonal $Li_2Mn_2O_4$ that occurs at 3 V vs Li. Because of this phase change, this causes a 16% increase in the c/a ratio. [22] This large anisotropic change would make it difficult to maintain structural integrity. As a result, $LiMn_2O_4$ has a high capacity fade from repeated charge and discharge cycles past the 3 V region. [9] Thus cycling is limited to the 4 V region. Even so, $LiMn_2O_4$ is still susceptible to capacity loss. Some have suggested that the loss is from the dissolution of Mn^{2+} into the electrolyte after disproportionation of Mn^{3+} into Mn^{2+} and Mn^{4+}. [23] An analysis of the electrolyte after cycling at 50 °C concluded that 34% of the capacity fade was due to dissolution. [24] Another possible explanation is the formation of $Li_2Mn_2O_4$ on the surface of the electrode from non-equilibrium cycling. [25]

$LiFePO_4$ was reported as a new class of materials for lithium and lithium-ion batteries known as phospho-olivine. It has a theoretical capacity of 170 mAh/g and is low cost. It is also known to not produce any oxygen at elevated temperature which makes it very safe. [21] Though its operating voltage is lower than $LiCoO_2$ and $LiMn_2O_4$ (3.45 V), its voltage profile is very flat. This indicates a two-phase reaction occurring where $LiFePO_4$ (triphylite) transform into $FePO_4$ (heterosite). Initially, $LiFePO_4$ have been

reported to have poor rate capabilities and poor capacity. Even at low current rates, only 0.6 Li/mol was reversible. [26] This was because of the low electronic conductivities in both in the triphylite and heterosite. [1] It was later discovered that by reducing the particle size to the nanoscale and the addition of carbon, sufficient capacities and current rates could be reached. Reducing the particle size would also lower the diffusion length through the solid for both ions and electrons. Carbon is also known have excellent electronic properties. Comparing to other intercalation materials, $LiFePO_4$ is less dense than layered or spinel materials. Along with a low chemical potential, $LiFePO_4$ has a low energy density. [27]

1.6 *Conversion*

Though improvements in intercalation materials have been made over the years, they are limited to their redox activity. Thus, conversion materials have been investigated to improve energy densities. Table 1.2 is a comparison of electrochemical properties between intercalation and conversion materials.

Compound	Class	E°_{cell} / V	$mAhg^{-1}$	$Wh{\cdot}kg^{-1}$	$Ah{\cdot}L^{-1}$	$Wh{\cdot}L^{-1}$
VF_3	Conversion	1.87	745	1389	2505	4673
CrF_2	Conversion	2.28	596	1360	2287	5224
CrF_3	Conversion	2.29	738	1689	2789	6383
MnF_2	Conversion	1.92	577	1107	2296	4405
MnF_3	Conversion	2.65	718	1902	2543	6732
FeF_2	Conversion	2.66	571	1522	2336	6224
FeF_3	Conversion	2.74	713	1954	2758	7561
CoF_2	Conversion	2.85	553	1578	2466	7039
CoF_3	Conversion	3.62	694	2509	2691	9735
SnF_2	Conversion	2.98	342	1021	1563	4665
α-PbF_2	Conversion	2.83	219	619	1852	5243
o-BiF_3	Conversion	3.13	302	946	2391	7484
T-BiF_3	Conversion	3.13	302	946	2539	7960
$LiCoO_2$	Intercalation	3.95	135-165	530-640	690-840	2700-3250
$LiMn_2O_4$	Intercalation	~4.0	148	590	630	2520
$LiFePO_4$	Intercalation	3.45	170	586	608	2097

Table 1.2. List of conversion and intercalation materials and their theoretical reduction potential vs. Li, gravimetric capacity (mAh/g), gravimetric energy density (Wh/kg), volumetric capacity (Ah/L), and volumetric energy density (Wh/L). BiF_3 has two different phases: orthorhombic (o-BiF_3) and hexagonal tysonite phase (T-BiF_3). [28]

Fluorides, specifically iron-based, have been a main focus in the Energy Storage Research Group (ESRG) because of its low cost and relatively low toxicity. [29] [30] [31] Compare to other conversion materials, fluorides have a high ionic M-F bonds allow higher reduction potentials around or even above 2 V. This is a great contrast to oxides, sulfides, nitrides, and phosphides where their observed potentials are below 1.5 V. [32] Figure 1.6 shows typical voltage of three iron-based fluorides that are of interest: FeF_2, FeF_3, and FeOF. FeF_2 is looked at because it is a Fe^{2+} in a rutile structure, representative of most 3d transition metal difluorides, with a simple voltage profile, $FeF_2 + 2Li \leftrightarrow 2LiF + Fe^0$ with a theoretical capacity of 571mAh/g. On the other hand, FeF_3 is noticed because of its Fe^{3+} in a ReO_3 type structure allowing up to three electron transfers resulting in a theoretical capacity of 712 mAh/g. The voltage profile show lithium insertion at higher

voltage, $FeF_3 + Li \leftrightarrow LiFeF_3$ before full conversion at lower voltage , $LiFeF_3 + 2Li \leftrightarrow 3LiF + Fe^0$. As a hybrid between these two materials, FeOF is of interest since it is a Fe^{3+} in a rutile type structure and oxygen is introduced as an anion creating a degree of covalency of the Fe bond. If fully converted into $Fe^0 + LiF + Li_2O$, FeOF can provide a theoretical capacity of 885 mAh/g. Near theoretical capacities were first enabled though the use of carbon-metal fluoride nano-composites (CMFNCs). [30]

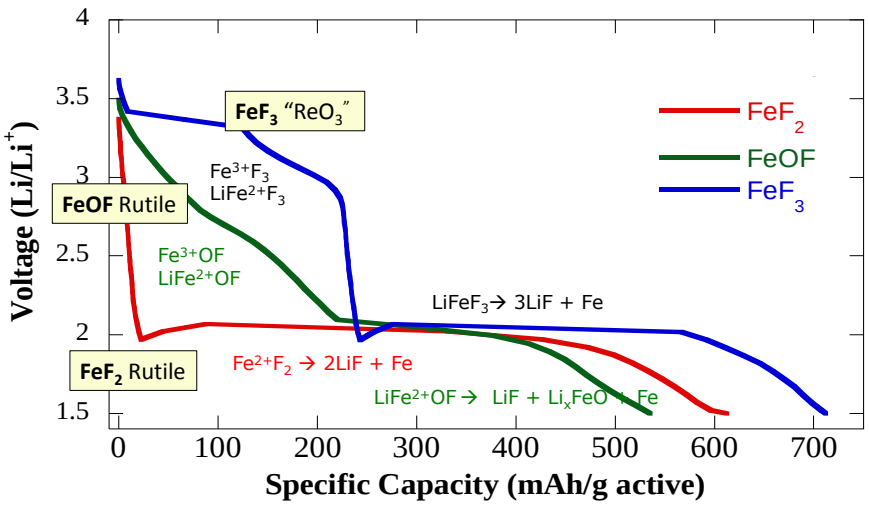

Figure 1.6. Typical voltage profiles of FeF_2, FeF_3, and FeOF.

The carbon matrix allowed electrons to move freely through the highly insulative cathode. The nano-size particles increased the amount of surface area in contact with both electrolyte and the carbon matrix. Despite forming these nanocomposites, it is believed these conversion materials are limited by the mobility of the Li^+ ions to move

to unreacted sites. Electrons may not be as limited because of the conductive network that is formed when the transition metal is reduced, although there is no experimental verification of this. This allows an electronic pathway for electrons to move to unreacted sites as illustrated in Figure 1.7 for FeF_2. [33] [34] In addition, the capacities of all iron compounds can only be achieved under low C-rates. One of the goals in this thesis is to determine conductivity and gain some insight into this percolated network.

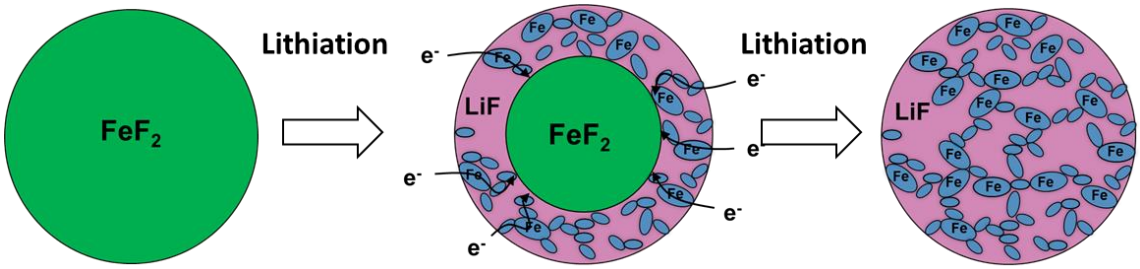

Figure 1.7. Illustration of conversion example of FeF_2. Because of the network of Fe formed during lithiation, electrons can travel to non-lithiated regions. Adapted with permission from Ref. [35]. Copyright (2014) American Chemical Society.

1.7 *Modes of mass transport*

In electrochemistry, there are three modes of mass transportation: migration, convection and diffusion. Migration is the movement of ions from an electrical gradient. In most electrochemical systems this is eliminated by adding supporting electrolyte. This reduces the potential gradient to zero and eliminate the electric field which causes migration. The supporting electrolyte can now carry the current with negligible migration. Convection is mass transport by gross physical movement such as stirring. This type of mass transport is helpful in increasing the flow of electroactive species to reaction sites. Some examples where convection is utilized in batteries in zinc/air

systems where the circulation of electrolyte helps prevent dendritic growth of zinc on the electrode which can cause a short-circuit and battery failure. [36] In flow batteries, pumps are utilized to circulate the anolyte and catholyte through the flow battery stack to allow more reactant to be consumed without having to build a larger battery stack (Figure 1.8). [37]

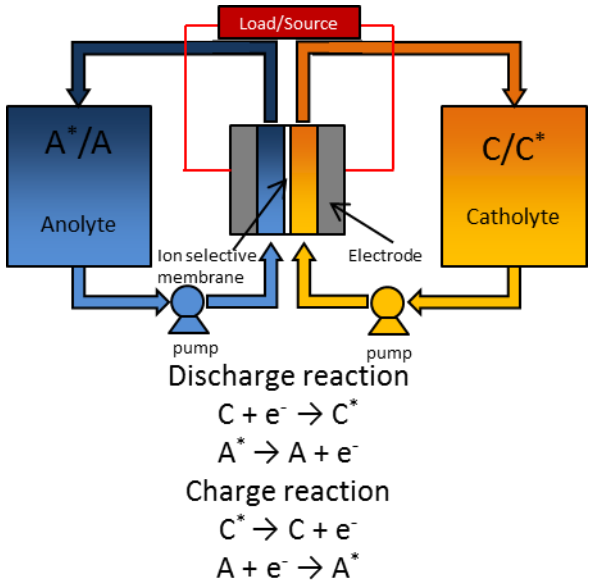

Figure 1.8. Example of flow battery. Electron transfer occur at the flow battery stack. Pumps are utilized to refresh the stack with fresh anolyte and catholyte from storage tanks. Adapted with permission from Ref. [37].

Lastly there is diffusion, the most studied means of mass transportation. Diffusion is the movement of a substance under the influence of a concentration gradient. Ficks's first law analyzes the diffusion flux as proportional to the concentration gradient under steady state.

$$J = -D\frac{dC}{dx} \quad \textbf{(1.5)}$$

Where J is flux, D is the diffusion coefficient, C is concentration and x is the position. Fick's second law takes into account the change in concentration with time (t) which is define by:

$$\frac{dC}{dt} = D\frac{d^2C}{dx^2} \quad \textbf{(1.6)}$$

In batteries, diffusion process is most significant in transporting species to and from the anode to cathode in order to maintain current flow. This can be approximated by rewriting Fick's first law, assuming that diffusion into the electrode is not limiting:

$$i = nF\frac{DA(C_B - C_s)}{\delta} \quad \textbf{(1.7)}$$

i is current and A is the contact area of the electrode. δ is the boundary-layer thickness between the bulk concentration of the electroactive species (C_B) and the concentration at the electrode surface (C_s). This is accomplish with the relationship that *i=nFJA* where J is the flux. The maximum current that a battery can put out is when C_s=0. Thus, the only means of increasing the battery rate performance is to increase the bulk concentration, electrode area, or diffusion coefficient.

Not only do ions have to diffuse through the electrolyte but into the electrode itself. If we assume one-dimensional transport, the chemical diffusion process can be described as Fick's second law, where x is the distance into the solid from the electrode/electrolyte interface. Ions diffuse into the solid because of the concentration difference from the electrode surface (C_s) and the local concentration in the solid (C_0).

Assuming that diffusion to the electrode surface is not limited, equation (1.7) can be used to determine the current where instead of the concentration difference is from the bulk electrolyte to the surface electrode ($C_B – C_s$), is the difference between the surface electrode and the local concentration in the solid ($C_s - C_0$). In electrochemistry, there are multiple methods in determining diffusion. [2]

1.8 *Cyclic Voltammetry (CV)*

Cyclic Voltammetry (CV) is a potentiodynamic electrochemical measurement. Similar to linear sweep voltammetry (LSV), the working electrode potential is ramped linearly with time and the current response is measured. In LSV, the measurement ends when the set potential is reached. However in CV, the working electrode potential is inverted and continues to linearly decrease in the opposite direction (Figure 1.9a). CV can be used to find the reaction mechanism during charge and discharge by plotting current response vs voltage as shown in Figure 1.9b. Each current peak in the graph is associated with an electrochemical reaction. Some sweeps may contain more than one current peak which indicates the occurrence of multiple reactions. Sometimes peaks can overlap each other and be convoluted. In order to separate one reaction peak from the other, identical cells are used. In the second cell, the same voltage sweep is applied as the first except that the potential is held constant after the first peak has formed and before the start of the second peak. This will allow on the first reaction to proceed without triggering the second. The second peak can be identified by the difference in current profiles for both cells. Diffusion coefficient can be determined by the current peak (i_p) using Randles-Sevcik equation:

$$i_p = 0.4463\left(\frac{F}{RT}\right)^{1/2} n^{3/2} A D^{1/2} C_{Li}^{1/2} v^{1/2} \quad \textbf{(1.8)}$$

F and R are Faraday's and gas constant as previously mention, n is the number of electrons transfer, A is the area of the electrode/electrolyte interface, C_{Li} is the initial concentration of lithium voltage sweep, and *v* is the voltage scan rate. It is assume that the diffusion of Li-ion behaves under Fick's laws and is treated as a one-dimensional semi-infinite diffusion. In semi-infinite diffusion, one side is treated to have a large amount species that any consumption is insignificant while the other side is changing over time. In this case, Li-ions in the electrolyte is considered having a constant concentration and the amount consumed is minute that the concentration does not change. The limitation is the amount of host material to accommodate the ions. Diffusion will continue to occur until the concentration in the host material is the same as the electrolyte. Since a Li-ion must be paired with an electron, diffusion rate can be determined from the current flow. In the scan profile, the peak intensity and peak separation changes with scan rate. With a faster scan rate the current peak intensity will increase, however peaks may become convoluted which may become difficult to distinguish multiple reaction mechanisms. [38] In porous electrode materials, A is usually the surface area of particulates. This can be estimated by the average size of the particles or by using Brunauer, Emmett and Teller (BET). [39] Though eq. (1.8) could be used on slow scan rates, it is not recommended because current peaks would not be well define and attractive interactions between the host and electroactive species may lower the apparent diffusion. The assumptions used to determine diffusion with CV are as follows:

1) One-dimensional semi-infinite particles: CV assumes that particles have simple geometries that are large enough such that finite size effects can be neglected.
2) Fickian dynamics: CV assumes that the transport is described by Fick's equation, with no gradient energy term
3) Constant D during perturbation: CV assumes that during the voltage sweep the diffusion coefficient does not change as the concentration changes.
4) Scan rate: CV assumes that the scan rate is fast enough that the above approximations hold, but be able to separate multiple reactions.
5) Extra-particle dynamics: CV assumes no impact on the current response from the dynamics outside the particles.

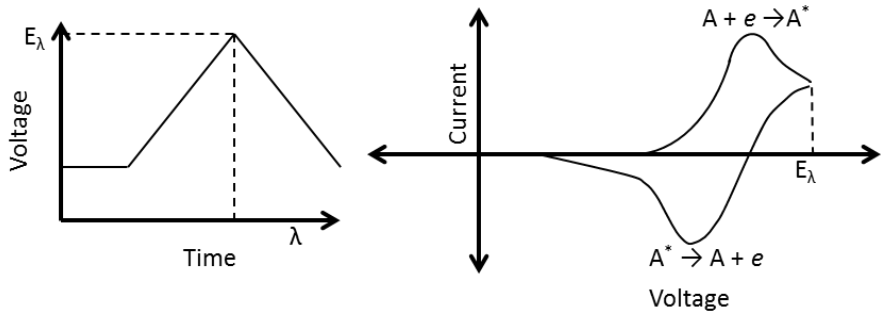

Figure 1.9. (a) 1 complete cyclic potential sweep. (b) Example of a cyclic voltammogram with one reaction mechanism. Adapted with permission from Ref. [39].

1.9 *Galvanostatic Intermittent Titration Technique (GITT)*

In galvanostatic intermittent titration technique (GITT), current is applied in pulses followed by a period of relaxation time, in which no current passes through the

electrochemical cell. Positive current is applied during change and negative during discharge. The same amount of current is applied during each current pulse. During a positive current pulse (Figure 1.10), the potential will suddenly increase from internal resistance (IR drop) of the cell. Afterwards, it would continue to increase slowly from the applied current. After a time interval τ, current is interrupted (relaxation) and the cell is allow time to relax to an open circuit potential (OCP). Because of the influx of mobile species at the surface of the electrode, there still remains a concentration difference between the surface and bulk. During this period the composition in the electrode will tend to become homogeneous by diffusing the remaining mobile species into the bulk. Initially during this equilibrium process, the potential will drop suddenly from IR drop and then continue to decay until reaching an equilibrium potential. Then the cycle repeats with a current pulse followed by relaxation until the cut-off potential is reached. The opposite holds true during a negative current pulse. As a negative current applied, there is an IR drop followed by a slow decrease in potential. During relaxation, the potential will suddenly increase from IR drop and then continue to slowly increase till it reaches equilibrium. The process continues again till a cut-off potential is reached. The cell voltage difference (Figure 1.10), not including IR drop during the period of applied current, is the total transient voltage change (ΔE_t). ΔE_s is the change of the steady-state voltage of the cell for a single step. [40] [41] [42] [43]

At the time when current pulse was initiated (t_0) the composition at the electrode is A_yB where A is the mobile species and B is the host material. After the

current pulse the composition becomes $A_{y+x}B$ where x amount of A ions have diffuse into the electrode. It can be define by the following equation:

$$\Delta x = \frac{I_0 \tau M_B}{n m_B F} \quad \textbf{(1.9)}$$

Where Δx is the stoichiometric change in the composition, I_0 is the applied current at the start of the current pulse (t_0), M_B is the atomic weight of B, and m_B is the mass of B. F and n are Faraday's constant and number of electrons transfered.

The diffusion coefficient can be calculated at each step using the following equation:

$$D = \frac{4}{\pi}\left(\frac{V_M}{AFn}\right)^2 \left[\frac{\mathrm{I}_0\left(\frac{dE}{dx}\right)}{\left(\frac{dE}{d\sqrt{t}}\right)}\right]^2 \quad \textbf{(1.10)}$$

V_M is the molar volume of the sample and A is the area of the electrode/electrolyte interface. $\frac{dE}{dx}$ is the change in potential from the stoichiometric change from the mobile species during the applied current. If a small amount of current is used, this can be approximated to $\frac{\Delta E_s}{\Delta x}$. $\frac{dE}{d\sqrt{t}}$ is the change in potential from the change in the square root of time during the current pulse. This can once again be simplified to $\frac{\Delta E_t}{\Delta \tau}$. By substituting these into eq. (1.9), diffusion can be found by:

$$D = \frac{4}{\pi\tau}\left(\frac{m_B V_M}{M_B A}\right)^2 \left(\frac{\Delta \mathrm{E_s}}{\Delta E_t}\right)^2 \quad \textbf{(1.11)}$$

It is important to know that eq. (1.11) is valid when $\tau << L^2/D$ where L is the thickness of the electrode. This is from the relationship:

$$L \approx \sqrt{Dt} \quad \textbf{(1.12)}$$

You can estimate the distance the mobile specie has traveled from its diffusion coefficient and the amount of time that has elapsed. In this case, if $\tau > \frac{L^2}{D}$, then enough time has passed for the mobile species to diffuse to the end of the electrode. This will change the concentration difference which will cause a change in diffusion rate. The calculated diffusion coefficient would appear to be lower then expected. The assumptions for GITT are as follows [44]:

1) One-dimensional semi-infinite particles: GITT assumes that particles have simple geometries that are large enough such that finite size effects can be neglected.
2) Fickian dynamics: GITT assumes that the transport is described by Fick's equation, with no gradient energy term
3) Constant D during perturbation: GITT assumes that during the current pulse the diffusion coefficient does not change as the concentration changes.
4) Constant $\frac{dE}{d\sqrt{t}}, \frac{dE}{dx}$: GITT assumes that these derivatives are constant to make it possible to write the diffusion coefficient (eqs. (1.10) and (1.11)) in terms of experimentally accessible quantities
5) Small current pulse: GITT assumes that the current pulse is small and short enough that the above approximations hold.
6) Extra-particle dynamics: GITT assumes no impact on the current response from the dynamics outside the particles.

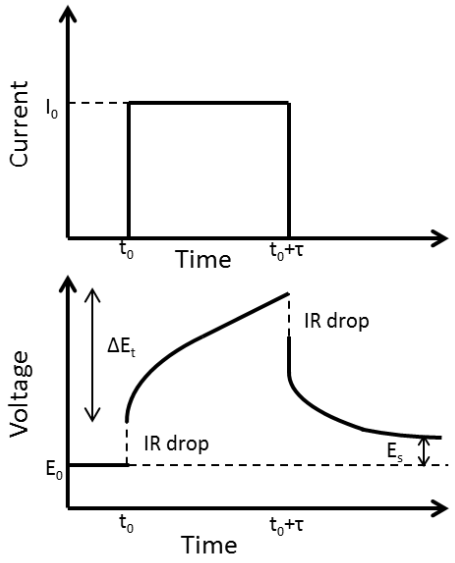

Figure 1.10. Current and voltage response of a single GITT step. Reproduced by permission of The Electrochemical Society. [41]

1.10 *Potentiostatic Intermittent Titration Technique (PITT)*

Potentiostatic intermittent titration technique (PITT) is similar to GITT except that a constant potential is held while the current is monitored. PITT is beneficial because the potential can be controlled such that reactions would not progress forward unless it is both kinetically and thermodynamically favorable. Thus, the reaction mechanism could be determined from the voltage profile. The experiment starts at OCP and a small potential difference is applied to the cell (Figure 1.11). On charge, the potential difference is positive with a positive current response. On discharge, the potential difference is negative with a negative current response. During a positive potential difference, there is an initial increase current response followed by decay in current and eventually reaching zero. However, typically this is stopped after reaching a cut-off current or time in order to complete the measurement in a practical amount of

time. After the potential is raised the same amount and current is measured until cut-off. This step repeats till reaching a final cut-off potential. On discharge, there is a small negative potential difference applied to the cell, the current initially becomes negative and slowly increase exponentially to cut-off current or time. This step repeats itself till a cut-off potential is reached. The current follows a Cottrellian behavior where [42]:

$$I(t) = nFA(C_s - C_0)\left(\frac{D}{\pi t}\right)^{\frac{1}{2}} \qquad \text{if } t << L^2/D \qquad \textbf{(1.13)}$$

The diffusion coefficient can be determined from the slope of the linear plot of I vs. $1/\sqrt{t}$ if the concentration difference is known. Under long step times, $t >> L^2/D$ current decays exponentially:

$$I(t) = \frac{2z_a FS(C_s - C_o)D}{L}\exp - \frac{\pi^2 \widetilde{D} t}{4L^2} \qquad \textbf{(1.14)}$$

This can be simplify by taking the natural log and taking the first derivative which yields:

$$\frac{d(\ln(t))}{dt} = -\frac{\pi^2 D}{4L^2} \qquad \textbf{(1.15)}$$

By rearranging the equation, D can then be calculated by taking the linear region in the graph of ln(I) versus t.

$$D = -\frac{d(\ln(I))}{dt}\frac{4L^2}{\pi^2} \qquad \textbf{(1.16)}$$

The advantage is that the concentration difference does not need to be known.

At long step times, the mobile species move towards equilibrium where the electrode becomes homogenous. The change in stoichiometry is directly related to the concentration difference under the relationship:

$$\Delta x = V_M(C_s - C_0) = \frac{Q}{nFn_B} \quad \textbf{(1.17)}$$

Where Q is the charge transfer, n_B is the number of moles of the host material. Q can be determined by the amount of current passing through during the potential step:

$$Q = \int_0^\infty I(t)dt \quad \textbf{(1.18)}$$

Knowing that the $L=(V_M n_B)/S$, eq.(1.13) and (1.14) can be rewritten in terms of Q:

$$I(t) = \frac{QD^{\frac{1}{2}}}{L\pi^{\frac{1}{2}}}\frac{1}{\sqrt{t}} \qquad \text{if } t \ll L^2/D \quad \textbf{(1.19)}$$

$$I(t) = \frac{2QD}{L^2}\exp\left(-\frac{\pi^2 Dt}{4L^2}\right) \qquad \text{if } t \gg L^2/D \quad \textbf{(1.20)}$$

In PITT the assumptions are as follows [44]:

1) One-dimensional semi-infinite particles: PITT assumes that particles have simple geometries that are large enough such that finite size effects can be neglected.
2) Fickian dynamics: PITT assumes that the transport is described by Fick's equation, with no gradient energy term.
3) Constant D during perturbation: PITT assumes that during the potential step the diffusion coefficient does not change as the concentration changes.

4) Cutoff current: PITT assumes in the case of eq. (1.19) and (1.20), that Q is found by infinite time integration which must be shortened after some practical interval.
5) Small potential step: PITT assumes that the potential step is small enough that the above approximations hold.
6) Extra-particle dynamics: GITT assumes no impact on the current response from the dynamics outside the particles.

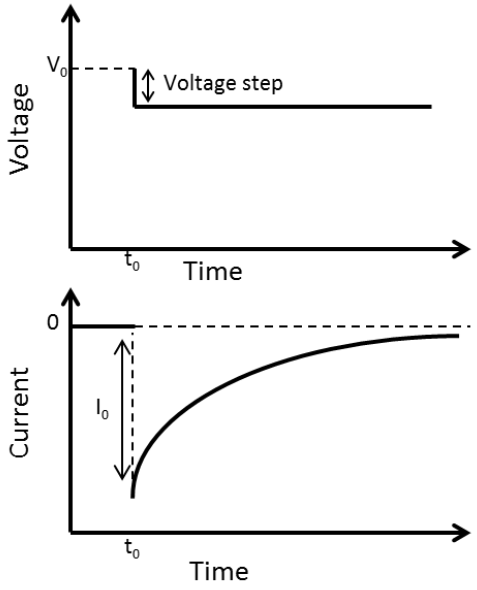

Figure 1.11. Current response of a single PITT step.

1.11 *Electrochemical Impedance Spectroscopy (EIS)*

In electrochemical impedance spectroscopy (EIS) or alternating current (AC) impedance, potential is swept from positive to negative in a sine wave and the current is

measured. Ohm's law defines voltage potential (V) in terms of current (I) and resistance (R):

$$V = IR \tag{1.21}$$

The current response would be in phase with the sweeping voltage for an ideal resistor. However in many materials, it is not the case and complex equivalent circuits are used to describe their behavior.

As potential is applied in a sinusoidal wave, the current response would also be sinusoidal at the same frequency but shifted in phase (Figure 1.12). In a linear system, both the potential and current response, as a function of time, can be described as the following [45]:

$$V = IR \tag{1.22}$$

$$I(t) = I_0 \sin(\omega t + \phi) \tag{1.23}$$

E_0 and I_0 is the potential and current amplitude of the signal, t is time, ω is the angular frequency which is related to frequency (f) by:

$$\omega = 2\pi f \tag{1.24}$$

From Eq. (1.21), we can calculate the impedance (Z) of the system as:

$$Z = \frac{E(t)}{I(t)} = \frac{E_0 \sin(\omega t)}{I_0 \sin(\omega t + \phi)} = Z_0 \frac{\sin(\omega t)}{\sin(\omega t + \phi)} \tag{1.25}$$

Z_0 is the magnitude of the impedance. When the sinusoidal potential and current is plotted on a graph, the result is an oval known as a "Lissajous Figure" (Figure 1.13). This is typically observed with an oscilloscope and was the acceptable method for measuring impedance prior to modern EIS instrumentation.

Using Euler's formula, it is possible to express impedance in a complex function:

$$\exp(j\phi) = \cos(\phi) + jsin(\phi) \quad \textbf{(1.26)}$$

$$E(t) = E_0 \exp(j\omega t) \quad \textbf{(1.27)}$$

$$I(t) = I_0 \exp(j\omega t - \phi) \quad \textbf{(1.28)}$$

j is the imaginary unit and the impedance can be represented as:

$$Z(\omega) = Z_0 \exp(j\phi) = Z_0[\cos(\phi) + jsin(\phi)] \quad \textbf{(1.29)}$$

Since Z(ω) is composed of both real and imaginary parts, it can be plotted with the real in the x-axis and imaginary on the y-axis we have a Nyquist plot as shown in Figure 1.14 for an electrochemical cell. In order to describe the data, equivalent circuits composed of ideal resistors (R), capacitor (C), and inductors (L). The relationship with impedance is shown in

Table 1.3.

Component	Definition	Impedance
Resistor	$E = IR$	$Z_R = R$
Capacitor	$I = C\frac{dE}{dt}$	$Z_C = \frac{1}{j\omega C}$
Inductor	$E = L\frac{dI}{dt}$	$Z_L = j\omega L$

Table 1.3. Circuit elements used to model EIS spectra.

Because real systems do not behave ideally, two additional components are used, constant phase element (CPE) and Warburg impedance (Z_W). Randle's equivalent circuit is typically used to interpret the impedance in an electrochemical cell, R_0 is the uncompensated ohmic resistance of the electrolyte and electrode; R_{ct} is the charge-transfer resistance, C_{dl} is the double layer capacitance, Z_w^* is the Warburg impedance. Narquisian impedance spectra show a semi-circle at high frequency which is the combination of R_o and R_{ct}. At very low frequencies a vertical line in which R reaches its limit which is the sum of (R_0 +R_{ct}) and R_L where R_L is the limiting low frequency resistance. [46]

The diffusion coefficient can be calculated by the Warburg impedance expressed as:

$$Z_W = \sigma(1 - j)\omega^{-\frac{1}{2}} \quad \textbf{(1.30)}$$

σ is the Warburg coefficient, j is an imaginary unit and ω is the angular frequency. σ can be found by taking the slope of Re(Z) vs ω^(-1/2). This can then be used in the equation:

$$\sigma = \frac{V_m}{\sqrt{2}zFAD_{app}^{1/2}}\frac{dE}{dx} \quad \textbf{(1.31)}$$

V_m is the molar volume of the cathode, z is the charge transfer between the anode and the cathode, F is Faraday's constant, A is the active surface area of the electrode and dE/dx slope of voltage.

The equation is rearranged to find D:

$$D_{app} = \frac{V_m^2}{2z^2F^2A^2\sigma^2}\left(\frac{dE}{dx}\right)^2 \quad \textbf{(1.32)}$$

We followed Ho's assumptions for Fick's diffusion equation which states that the lithium diffusion into the cathode is a semi-infinite and that during the time period of the measurement is taken for, lithium has not penetrated to the end of the cathode. [46] Furthermore, the driving force for diffusion is a gradient in relation to composition and that the electrical field in the electrode can be negated. Lastly, the diffusion coefficient is linearly and independently related to the concentration over the range of the alternating voltage that is applied.

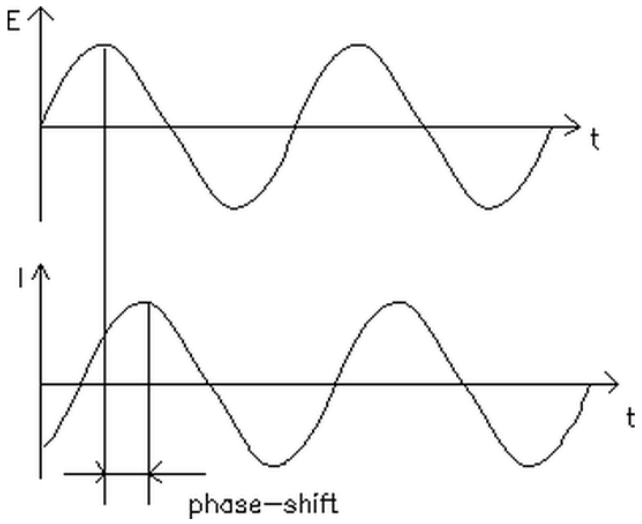

Figure 1.12. The current response to a voltage sweep is shifted by ϕ. Reprinted with permission from Ref. [45].

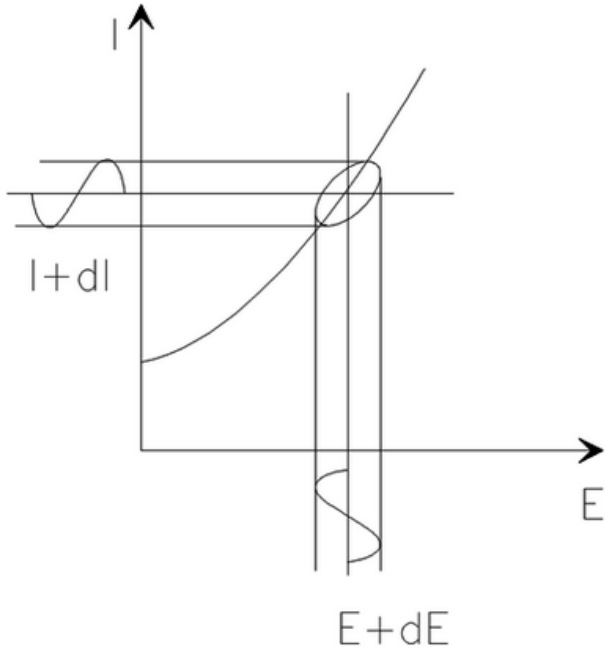

Figure 1.13. Lissajous Figure is formed from both current and voltage components. Reprinted with permission from Ref. [45].

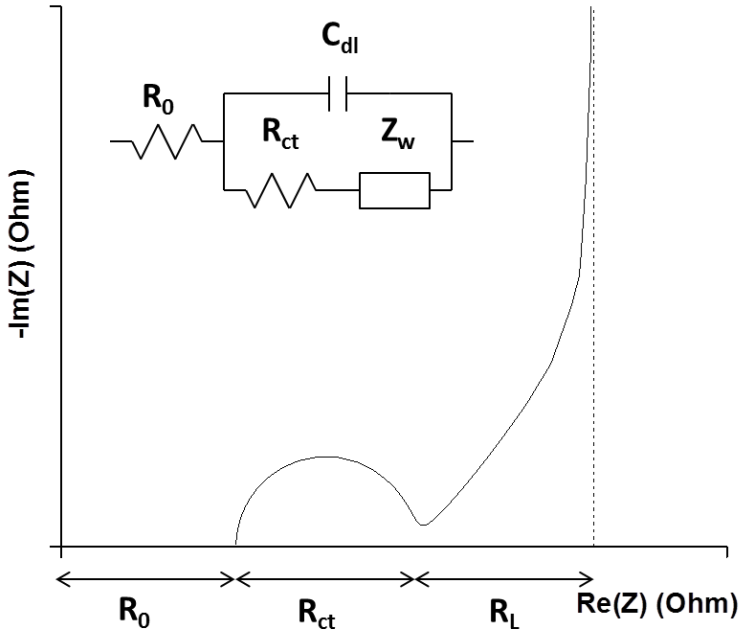

Figure 1.14 An illustration of Randles circuit. Adapted with permission from Ref. [35]. Copyright (2014) American Chemical Society.

1.12 *Overpotential polarization*

Ideally it would be desirable that all the chemical energy be converted to usable electrical energy. However, polarization can cause a drop in voltage and loss in energy. Activation, concentration, and ohmic polarizations consume useful energy and release it as waste heat. Figure 1.15 shows how these polarizations can affect a cell's operating voltage.

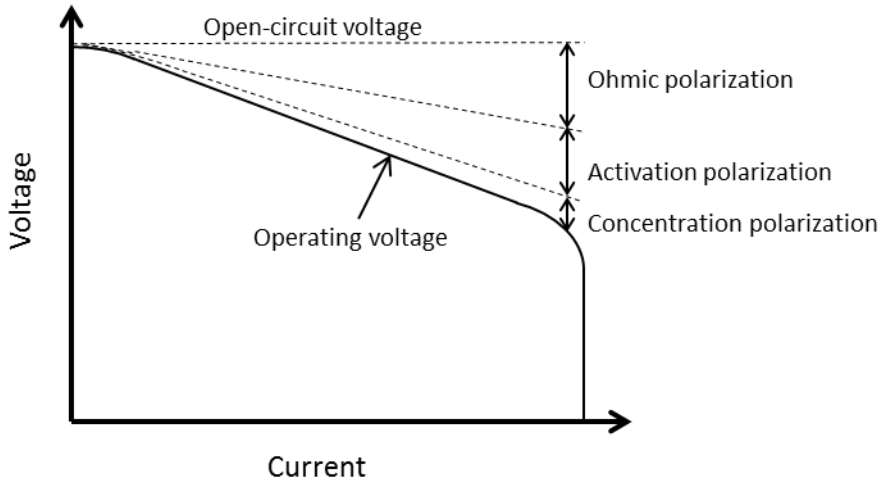

Figure 1.15. Cell potential profile as a function of current. There is a greater potential loss with increasing current. Reproduced with permission from Ref. [2].

Energy loss is minimal when operating current is small and can be detrimental when large. Even though the capacity of a battery is determine by the electrochemical reactions, polarization can greatly affect their performance. In order to minimize these effects, it is essential to understand the components that cause polarization.

The reaction rate is determined by the slowest reaction step of the process. The energy barrier in this rate-determining step must be overcome in order for the reaction to proceed further. As a result, the electrode potential changes in order to overcome the barrier. Activation polarization is the overpotential caused by the energy barrier of the rate-determining step of the electrochemical reaction. In 1905, Tafel observed that this overpotential is linearly proportional with the log of the current.

$$\eta = a \pm b \log i \tag{1.33}$$

Where η is the overpotential, i is current, and both a and b are constants. This is more noticeable under high overpotentials. Tafel's equation has been used in studies of activation overpotential for hydrogen formation where the slowest step is the formation of gas. As hydrogen ions collect at the cathode gaseous hydrogen is formed. It collects together to form a bubble which will stick to the cathode surface. This affects the kinetic process as it lowers the amount of usable surface. Eventually, enough gaseous hydrogen will collect together releasing it from the surface of the cathode. [2] [47]

According to the Nernst equation, we can determine the potential for the concentration at the electrode and bulk:

$$E = E^0 - \frac{RT}{nF}\ln(C) \quad \textbf{(1.34)}$$

Where R is the gas constant, T is the temperature, C is the concentration of the bulk or electrode surface. Because there is a difference in concentration, there is also a potential difference which yields a concentration overpotential (η_C) where $\eta_C = E_E - E_b$. The concentration polarization could be reduced by either convection or by increasing the operating temperature to increase the movement of the electroactive species. [48]

Lastly, there is ohmic polarization or IR drop. All electrochemical cells have some internal impedance. The total internal impedance is compose of the ionic resistance of the electrolyte, electronic resistance of the electrode and current collectors, as well as the contact resistance between them. This can be seen with EIS as mention previously. Internal resistance greatly affects the performance and rate capability of a cell. The

voltage drop is proportional to the amount of current flowing through the cell as it follows Ohm's law.

The total voltage drop from polarization can be expressed as:

$$E = E_0 - [(\eta_{ct})_a + (\eta_c)_a] - [(\eta_{ct})_c + (\eta_c)_c] - iR_i \quad \textbf{(1.35)}$$

E_0 is the open circuit voltage of the cell, $(\eta_{ct})_a$ and $(\eta_{ct})_c$ is the charge-transfer overpotential or activation polarization at the anode and cathode, $(\eta_c)_a$ and $(\eta_c)_c$ is the concentration polarization at the anode and cathode, i is the operating current, and R_i is the internal resistance of the cell. At high current rates, voltage drops due to polarization effects are more apparent on both charge and discharge. The voltage gap that is formed from this is called hysteresis.

1.13 *Intrinsic Hysteresis*

Not to be confused with hysteresis induced from polarization, intrinsic hysteresis is the voltage difference from charge and discharge not caused by high cycling rates and is inherent to a material. Polarization hysteresis can be reduced by reducing the current rate, minimizing particle size, or electrode thickness. This effectively reduces the current density or decrease the impedance from charge transfer. While this is more noticeable in conversion materials, some intercalation materials contain a small amount of intrinsic hysteresis. [26] [49]

In intercalation materials, intrinsic hysteresis is a result from the many-particle model. To understand this model, we first look at the properties for a single particle.

Assuming a single nano-size particle of $LiFePO_4$, neglecting possible mechanical phenomena, the chemical potential of Li as a function of composition is shown in Figure 1.16. The black dotted line is the equilibrium potential in which the two phases ($FePO_4$ and $LiFePO_4$) can coexist. During galvanostatic charge (red), the potential passes the equilibrium line as an overpotential reaching a local maximum (point A to B). This area at point B is the spinodal region where two phases are formed inside the particle, one having a higher lithium concentration than the other. During this phase formation, the potential decreases back to equilibrium (point B to C) will continue on the line during charge (point C to D).

In the case where there are multiple particles involve, it assume that these particles are close enough to allow Li-ions to exchange with each other. Similar to a single particle case on delithiation, the potential passes the equilibrium potential and into the spinodal region. At one point, a single particle will decompose into two phase and the potential will decrease to the equilibrium point, however it is not stable since it is in contact with other particles with varying amount of Li concentration. The single particle will quickly become homogeneous by redistributing its remaining Li-ions to other particles. As lithium continues to be removed from the system the potential is once again raised until another particle decomposes that the potential drops this is show in Figure 1.17a. Though this may be noticeable in a small numbers of particles, electrodes are composed of thousands of particles that these potential drops are never seen resulting a higher than normal equilibrium potential (Figure 1.17b). [50]

One of the drawbacks of conversion materials is the large hysteresis found in its cycling profile. [51] In conversion materials, intrinsic hysteresis is not mainly caused by particle transformation but rather different reaction pathways. As shown using first principles, there are many intermediate phases present on lithiation and delithiation. [52] [53] [54] For example with FeF_3, Doe et al. initiated that during lithiation the calculated equilibrium pathway is to form $Li_{1/4}FeF_3$ then $Li_{1/2}FeF_3$ before Fe and LiF precipitate out. However, kinetics can cause FeF_3 to deviate from this pathway and follow nonequilibrium ones as the equilibrium potential does not match with that found experimentally as there are several potential drops in the voltage profile. One possibility is that there is a stable phase between $Li_{1/2}FeF_3$ and 3 LiF + Fe that allows it to drop further down, such as $LiFeF_3$ and $Li_{3/2}Fe_{3/4}F_3$. The other is that the slow moving Fe in the fluoride phase is so slow that it does not precipitate out until Li concentration reaches $LiFeF_3$. This kinetic limitation would also explain the different pathway during delithiation.

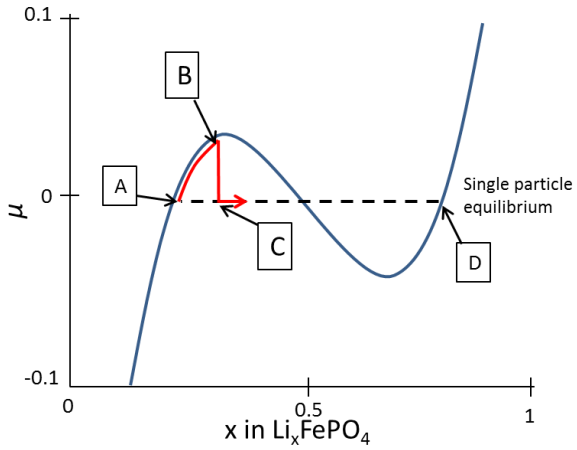

Figure 1.16. Chemical potential profile of $LiFePO_4$ in a single particle case. Blue curve assume no phase transition. Red curve is the expected pathway for a single particle with a phase transformation. Adapted by permission from Macmillan Publishers Ltd: Nature Ref. [50], Copyright (2010).

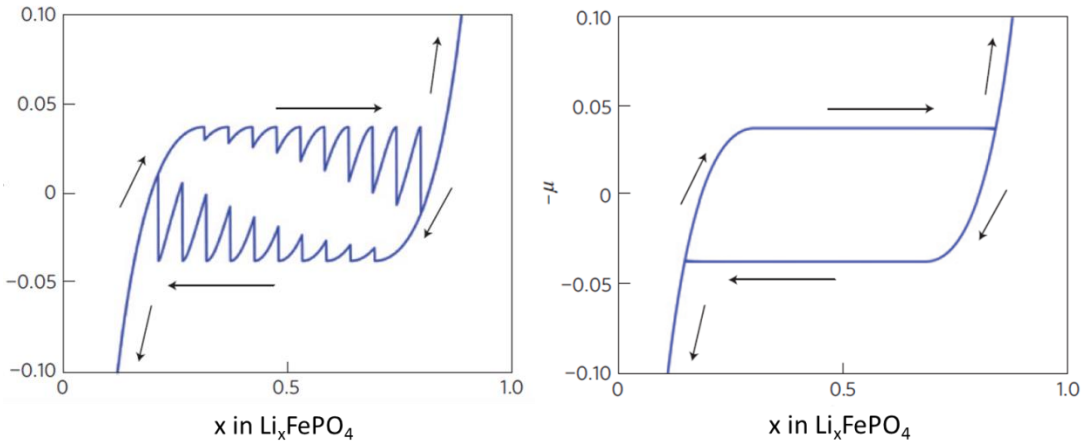

Figure 1.17. Chemical potential profile in a many particle case. (a) assumes only 10 particles involved. (b) assumes only 1,000 particles involved. Reprinted by permission from Macmillan Publishers Ltd: Nature Ref. [50], Copyright (2010).

1.14 *Percolation Theory*

In conversion materials, metal precipitates out during lithiation and potentially forms a conductive metal network in an insulating lithium salt matrix. [32] [33] [18]

Because of the metal network through the insulating salt, it may support electronic transport to the reaction front during discharge. This matrix of metal–insulator can be described through percolation theory. Percolation is a standard model for disordered systems. It can be used to describe transport in amorphous and porous materials. This can also be used in the real world such as the distribution of oil in a porous rock or water through coffee grinds. To better describe this, if we assume a 2-D square lattice where each site is randomly chosen to be either occupied with probability *p* or empty with a probability 1-*p* (Figure 1.18). We also assume that occupied sites are completely conductive and empty site completely insulative and that electrons can only travel through conductive sites near each other. Under low concentration, *p*, conductive sites are either isolated or had formed small clusters. In either case, current cannot travel from one edge to the other. As concentration increases, more sites become filled until a critical point, p_c, where sites have become interconnected to support electron transport. Further increase will increase more interconnectivity between conductive particles which in turn will increase conduction. Below p_c is an insulator and above p_c is a conductor. [55] [56]

There are several different models that are used to describe different types of percolation networks, a few noteworthy are mention herein. Site percolation was described previously where sites are considered part of a cluster when they are next to each other. An example is a mixture of paramagnets and ferromagnets, where at p_c, the mixture changes from paramagnetic behavior to ferromagnetic.

Another different model is bond percolation, where all sites are occupied but a physical bond between nearest neighbors is required to be part of a cluster (Figure 1.19). The probability for one site to bond to another is *q* and at a critical concentration of bonds, q_c, the system changes for a phase with finite clusters to a phase of infinite clusters where they are interconnected. An example is the gelation process in boiling an egg, at room temperature it is a liquid and upon heating, it transforms into a solid-like gel. Site-bond percolation is used in the gelation behavior in diluted liquids. In this case, clusters are formed when sites are both occupied with a probability *p* and bonded with a probability *q*.

Lastly there is continuum percolation where the positions in a mixture are not restricted to discrete sites of a lattice, but in the overall material. Unlike site and bond percolation, continuum percolation does not depend on the coordination number of the lattice. A simple example is a sheet of conductive material where circular holes are punched out randomly. The amount of conductive material is now a fraction, *p*. In 3-dimensions, the empty spaces can be treated as spherical voids in the material. Continuum percolation is also known as the Swiss cheese model because of the resemblance. This model has been used to describe sandstone or other porous materials.

Percolation theory can be used to describe electronic transport in material composites. Conductivity (σ) is proportional to the molar concentration (x) by the following equation [55] [56]:

$$\sigma \sim (x - x_c)^{\mu} \quad \textbf{(1.36)}$$

Where x_c is the critical volume fraction where electronic transport can be supported, μ is a critical exponent which is 1.30 for two-dimensional percolation and 2.00 for three-dimensional percolation. The expected x_c is different depending on the type of model used. x_c can be found by measuring conductivity at different compositions as shown in Figure 1.20. The sharp increase in conductivity is determined to be x_c where the metal particles become interconnected to allow electronic transport. Conductivity at x_c can vary from several orders of magnitude since it becomes conductive from a completely insulating state. When $x>x_c$ conductivity continues to increase a few orders of magnitude until σ_M when x=1 is composed of only pure metal. The critical exponent, μ, can be determined by ploting ln(σ) with respect to $\ln(x-x_C)$ and finding the slope of the linear region.

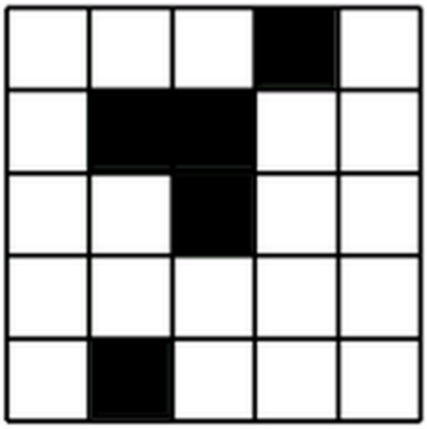

Figure 1.18. Example of site percolation in a square lattice. Black squares are considered filled positions Adapted with permission granted by Wolfram Companies, www.wolfram.com, Ref. [57]

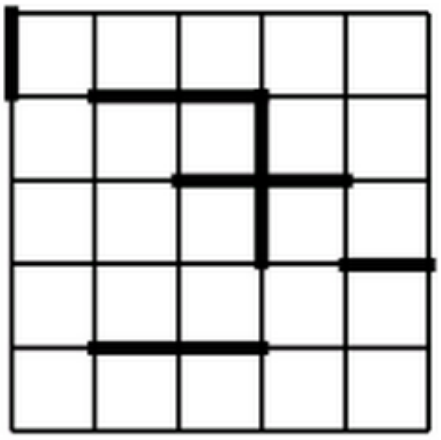

Figure 1.19. Example of bond percolation. Adapted with permission granted by Wolfram Companies, www.wolfram.com, Ref. [57]

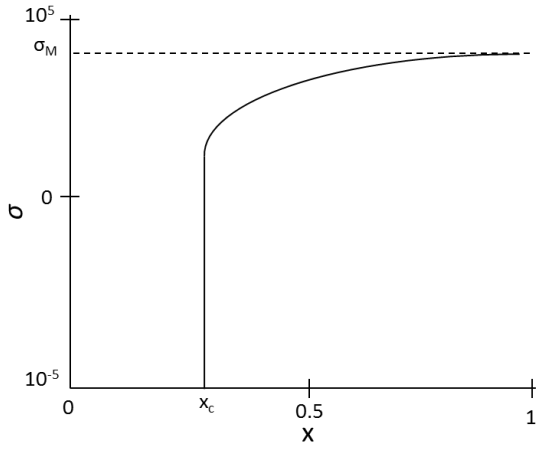

Figure 1.20. Schematic diagram of the conductivity (σ) at different volume compositions (x). x_c is the critical volume fraction in which metal particles for a conductive network. σ_M is the conductivity of pure metal.

1.15 *Summary and Organization of Thesis*

Although intercalation positive electrode materials provide decent capacity with reasonable cyclability, the demand for energy storage with higher energy densities has led into conversion type materials. Iron-based metal fluorides can provide three times

the capacity of traditional intercalation materials at a fraction of the cost. By making CMFNCs, the full capacity could be utilized reducing the fluoride into a percolated network of metal in a LiF matrix. Despite these beneficial factors, there are still many questions that are left unclear such as the properties percolated structure that forms on lithiation and the causes for its low cycling rate. This thesis will focus on identifying the reaction mechanism involved during lithiation and delithiation. Quantify both electronic and ionic transport and relate to their poor electrochemical performances. Establish in what way does mobility of ions affect the reaction pathway taken during lithiation and delithiation, and how do these changes the hysteresis seen in the voltage profiles.

Chapter 2 provides background information on the instruments used for electrochemical and physical characterization throughout this thesis.

Chapter 3 presents detail work on ionic transport and reaction mechanism in these iron-base fluorides using high resolution PITT. In this chapter, a new method is presented in determining intrinsic hysteresis eliminating nucleation induced overpotentials. The reaction mechanism for these fluorides during reconversion was of interest especially FeF_2.

Chapter 4 focuses on the electronic transport aspect of these fluorides. The main focus was to determine if the percolated structure that forms during lithiation is electronically supporting. Thin films of FeF_2 were deposited onto interdigitated electrodes (IDE) and chemically lithiated. Results were compared with pure Fe film as well as a contrasting fluoride, BiF_3.

Chapter 5 incorporates the results from chapter 4. An alternative method was used to quantify ionic transport in these fluorides by utilizing the conductive properties of the percolated structure.

2 Experimental Techniques

2.1 *X-ray Diffraction (XRD)*

XRD is a useful tool in identifying different phases in materials. It can be used to determine size, shape, internal stresses, and preferential orientation. It is most powerful when applied to crystalline materials. Crystalline materials contain atoms that are arranged in a long order repeating pattern in solid form. Amorphous materials are solids having only order short distances. As X-rays penetrate the surface of the material, the atomic planes of the crystal will cause X-rays to interfere with each other as they exit. However, at certain angles, x-ray beams are reflected at the same angle as the incident beam. Bragg correlated the diffracted X-ray beam to the d-spacing between crystallographic planes:

$$n\lambda = 2d \sin\theta \quad \textbf{(2.1)}$$

Where n is the order of the reflection (usually n=1), λ is the wavelength of the x-ray beam, *d* is the d-spacing of successive atomic planes, and θ is the angle between the atomic plane and both the incident and reflected beam (Figure 2.1). Crystals can have more than one plane with different d-spacings and each reflect at different angles. Each plane is associated with a certain hkl associated with the crystal. At other angles, X-rays are instead diffracted. There are seven major crystal systems: triclinic, monoclinic, orthorhombic, tetragonal, trigonal, hexagonal, and cubic. Some compounds may have the same crystal structure but have different d-spacings for the same hkl. This is from the different elements that make up the compound. Since atoms have different sizes

depending on the element, this can cause planes to have different d-spacing. Because of these differences, each crystalline material has a unique XRD pattern which can be used for identification.

A typical XRD consists of three major components: X-ray source, sample mount, and detector (Figure 2.2). During operation, two of the components move while the third is fixed to form different incident beam angles. In the X-ray source, a W cathode filament is heated to the point that electrons are ejected out of the material. Under high voltage (40 kV) and low current (40 mA), electrons are pulled to a metal anode (typically Cu) where they bombard it at high velocities. This causes the electrons in the metal atoms to become excited, moving to higher orbitals and on relaxation they emit a distinct wavelength x-ray. Since the two most common types of x-rays generated are K_α and K_β, a filter is used to absorb the K_β X-rays (typically Ni). Usually the ideal choice for a X-ray filter is a metal whose atomic number is one less than the anode metal. [58]

Bruker D8 Advance diffractometer was used for XRD. The X-ray source and detector, in our case is a position sensitive detector (PSD), are mounted to a goniometer. At the center is the sample mount that is fixed in place. The sample mount is custom made to hold a glass slide so that thin films or small amounts of powder could be used. There are two different scanning protocols that the XRD can utilize: continuous and step scan. Continuous, as it states, the source and detector move across various angles without stopping so that all diffracted X-rays are collected. Step scan is similar to

continuous except that it is held at an angle for a certain period of time before proceeding to the next angle. The protocol use here is a continuous scan from 15-60 ° with 0.02 increments at 1.9 scan speed which is equivalent to a scan rate of 0.631°/min.

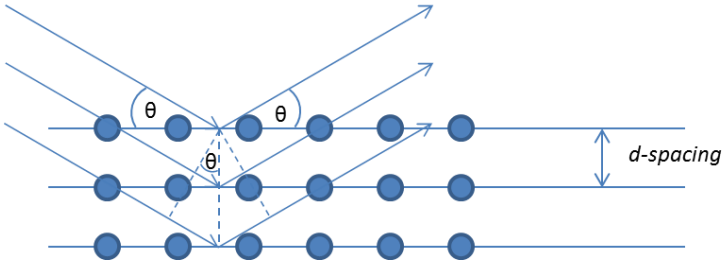

Figure 2.1. Illustration of X-ray Incoming beam being reflected at angle θ.

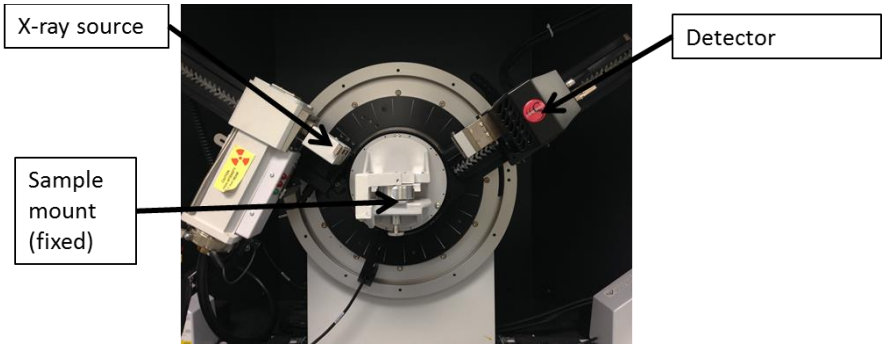

Figure 2.2. Components of X-ray Diffractometer.

2.2 *Profilometer*

Profilometry has been useful in the assessment of the surfaces using two-dimensional surface profiles. The two main types of profilometry are contact and non-contact. Contact systems involve a mechanical stylus that scan along the surface of the

material. Non-contact systems involve different technique (optical focus detection, optical interferometry, light scattering, capacitance, etc.) to determine the surface profile that does not require physical contact. This is useful on materials which their surface is sensitive to physical contact. The advantage of using contact type profilometers over non-contact is that they can be used in dirty environments where non-contact methods may measure the surface contaminants instead of the surface of the material itself.

In a contact profilometer (Figure 2.3), has a stylus with a small tip that is sensitive to the surface of the material. The sample sits on a stage that can move in the x and y direction while the stylus measure the z. As the stylus moves across the surface (x-direction), the change in vertical movement (z-direction) measured by a linear variable differential transformer (LVDT) or an optical transducer which is physically connected to the tip. They convert this signal from analog to digital form. The digital signal is amplify and process by several other electrical components. A two-dimensional profile is collected from a single scan. Thus to get a three-dimensional profile, several scans are made where each scan is a shift from the last scan (y-direction).

Thickness measurements were taken using a Dektak 150 (Vecco) with a 2.5 µm radius tip stylus. The sample profile was scanned for 500 µm in 10 secs, a 0.167 µm resolution. The stylus had only 3 mg of force on the sample so it would not damage it.

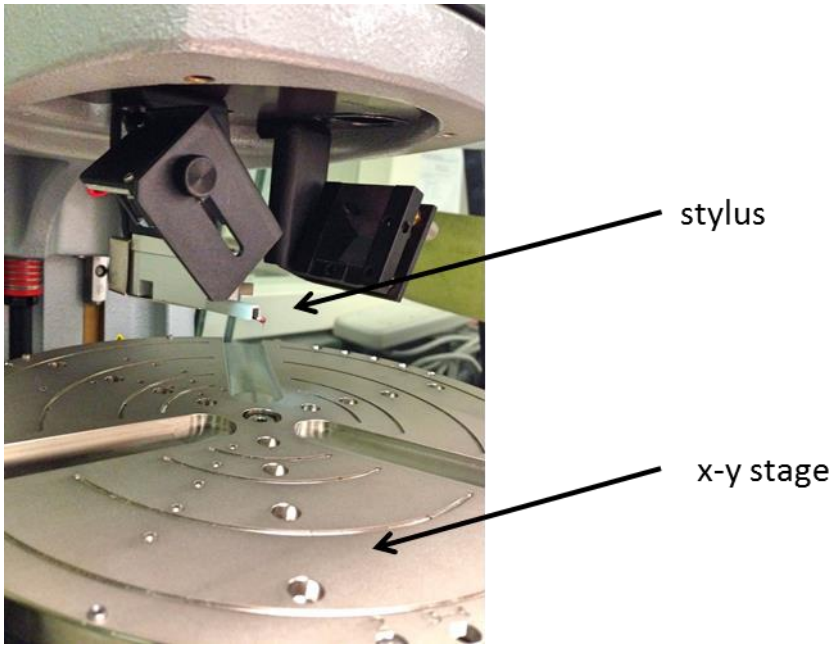

Figure 2.3. Components of profilometer.

2.3 *Electrochemical Characterization*

Several different electrochemical instruments were used to identify certain properties of an electrochemical cell. Galvanostats and potentiostats, such as the Macpile (Biologic) and Arbin BT2043, can provide performance information as well as intrinsic properties of the materials. Galvanostats are galvanostatic instruments that control the current though the cell and record voltage change. Alternatively, potentiostats are potentiostatic instruments that control the voltage through the cell and record the current change. In both cases, experiments can be made based from a cell's voltage, current, capacity, or time elapsed. GITT and life cycling are some typical testing methods used with galvanostats.

Other than mA and mA/g, current can be described as C-rates. In describing cell, C-rates are used to compare to other cells with different capacities. It is determined based off of its maximum capacity. For example in discharge, a 1C rate means that the cell will completely discharge in 1 hour. C/2 rate is half of the current rate and thus will take 2 hours to completely discharge. In order to determine the current rate in ampere, the capacity is substituted for C.

Figure 2.4. Macpile unit contain 16 channels used for testing cells. Ch. 1-8 is for galvanostatic tests and Ch. 9-16 is for potentiostatic tests.

PITT and CV are used with a potentiostat where controlling the potential is important. Voltage potential can be determine by the working electrode and counter electrode. Sometimes reference electrodes are used for determining the potential for a specific electrode. The reference electrode contains a material that has little or no effect on the cell during testing. A small amount of current passes through the reference electrode in order to determine the potential. In our experiments, half cells are made

such that lithium metal is both the counter and reference electrode while fluoride is the working electrode. Figure 2.4 is of the Macpile which contain dedicated channels for both galvanostatic and potentiostatic tests. Each Macpile contain 16 channels which usually have half for galvanostatic and the other for potentiostatic. In some cases, all 16 could be made to run only galvanostatic tests. The Arbin (Figure 2.5) on the other hand, contains 48 channels and along with an expansion deck, can reach up to 64 channels. Unlike the Macpile, all 64 channels can run both galvanostatic and potentiostatic tests. This is ideal when switching between different testing protocols.

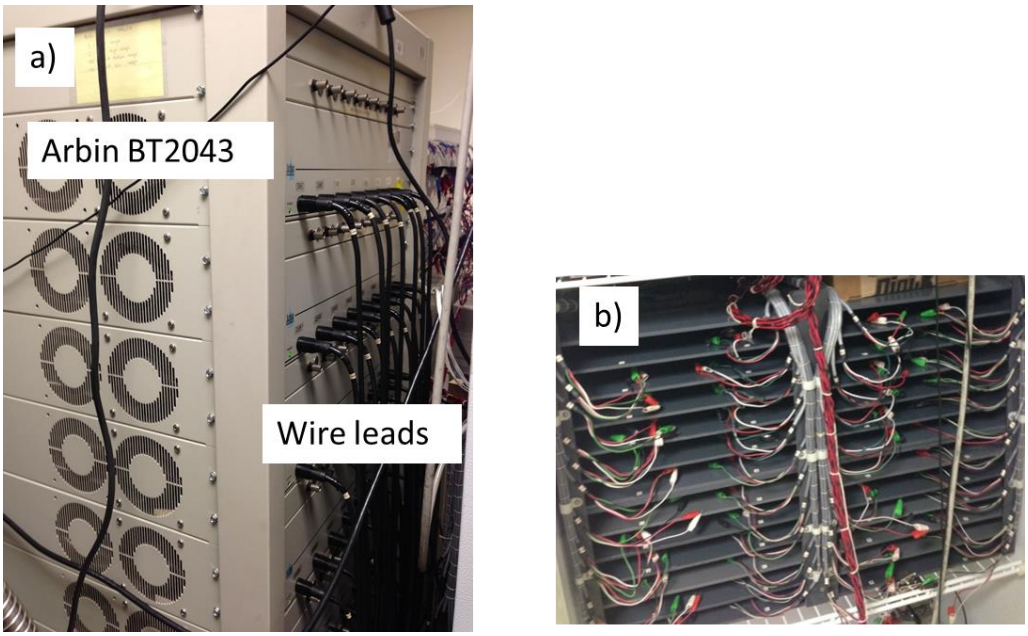

Figure 2.5. Arbin BT2043 can contain up to 64 channels. Wires from the Arbin unit (a) lead to a temperature control refrigerator in (b) where channels are separated from each other with shelves.

The Solartron contains an electrochemical interface (SI 1287) that can run both galvanostatic and potentiostatic tests (Figure 2.6). It also paired with an

Impedance/gain-phase analyzer (SI 1260) that can used to apply sine wave to galvano or potentiostatic tests. This is used with EIS to understand the ion interactions within the cell.

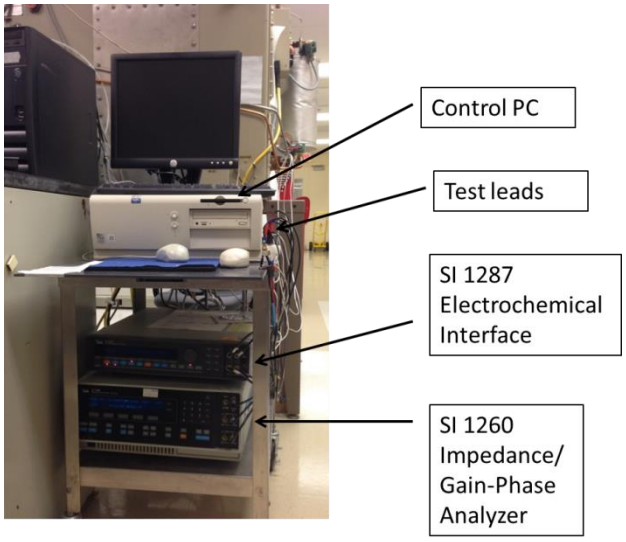

Figure 2.6. Solartron SI 1287 and SI 1260 used for EIS and DC polarization.

Another testing method, direct current (DC) polarization, was also used with the solartron. In DC polarization, potential is held at a certain value and current is monitored. In electrochemical cells, current will eventually drop to zero. In materials that allow ionic and electronic mobility, current will decay but never reach zero as shown in Figure 2.7. DC polarization is useful in separating ionic conductivity from electronic because as a potential is held constant, ions will move and stick to one of the electrode. In the end, only electrons will be able to move freely through the circuit. VMP (Biologic) is similar to the Solartron except that it can run up to 16 channels

simultaneously, shown in Figure 2.8. Each channel has a dedicated board that can be switched out depending on the test.

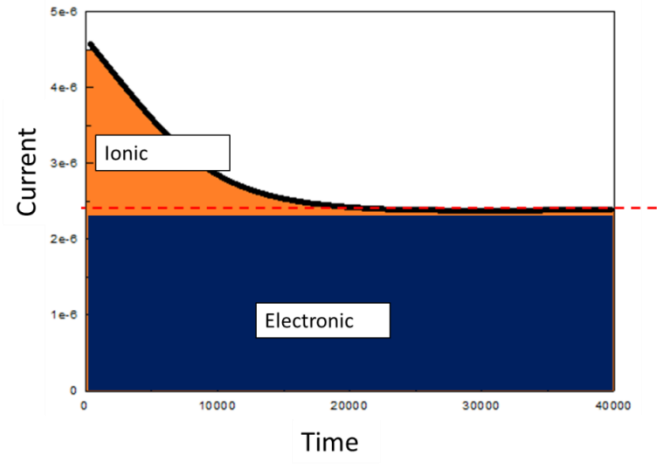

Figure 2.7. Typical current profile of DC polarization. The ionic component will be blocked at the electrodes leaving only the electronic component.

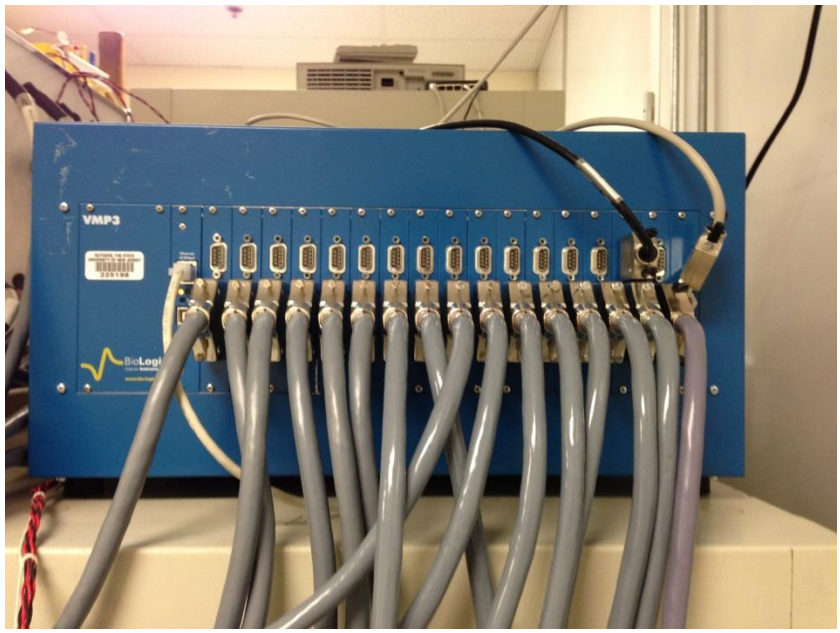

Figure 2.8. VMP instrument containing 16 interchangeable boards.

3 Transport, Phase Reactions, and Hysteresis of Iron Fluoride and Oxyfluoride Conversion Electrode Materials for Lithium Batteries

3.1 *Introduction*

Portable electronics have given rise to improved rechargeable batteries to address demands of power and energy. Current commercial batteries typically contain intercalation cathode materials (e.g. $LiCoO_2$, $LiFePO_4$). While they provide very good reversibility, they exhibit a limited capacity. At the "true" theoretical capacity, the layered structure only allows one electron transfer per transition metal. In addition, the amount of accessible energy is only a fraction of its true capacity. Conversion materials can have up to four times the typical capacity found in intercalation materials by utilizing all of the metal's redox potential and reducing it to its pure metal state. One of the challenges for conversion materials is the limited mobility of the Li^+ ions to move to the unreacted sites. Electrons are not as limited because a conductive network is formed when the transition metal is reduced allowing an electronic pathway to unreacted sites. [33] [34] Fluorides, specifically iron-based, have been a main focus of our group because of their low cost and relatively low toxicity. The high ionic M—F bonds allow higher reduction potentials around 2 V. Herein we will present data on three transition metal fluorides: FeF_2, FeF_3, and $FeO_{0.67}F_{1.33}$.

When cells are cycled galvanostatically, i.e. under constant current, the voltage profile is a composite of theoretical reaction potential, polarization and intrinsic hysteresis. Polarization can be reduced dramatically since it is not inherent to a material,

in contrast, hysteresis cannot. Intrinsic hysteresis is a common property that is found in all conversion materials and was clearly shown by the Tarascon group for metal oxides and sulfides. [59] Metal fluorides exhibit similar challenges. [30] [60] [61] Doe et al., proposed a model for the large intrinsic voltage hysteresis found in FeF_3. [54] Since Fe mobility is slower than Li^+ ions, Li^+ follows a different reaction pathway than what is thermodynamically favorable during the conversion process. As a result, many metastable pathways could be identified through calculations, especially on delithiation with little potential difference. [54] Dissimilarities in reaction mechanism between charge and discharge could account for the presence of intrinsic hysteresis in conversion materials. This is distinct from intrinsic hysteresis postulated for all insertion material systems as discussed by Dreyer and Moskon in their many particle models. [50] [62]

Accurate characterization of overpotential and hysteresis is critical to the understanding and optimization of the electrode kinetics, and reaction pathways of conversion materials. In galvanostatic intermittent titration technique (GITT), current is applied in pulses while voltage is monitored. Upon current relaxation, voltage decays to an equilibrium voltage. [41] While this voltage corresponds to a specific lithium concentration in the cathode for intercalation materials; this cannot be used for conversion materials since the equilibrium state is split between converted material and unconverted material. More importantly, the relaxation voltage would also be considered the equilibrium potential for both converted and unconverted material to coexist, not for the reaction to proceed. This chapter will show that for conversion materials, galvanostatic measurements, although useful for evaluating kinetic

polarization, are not as helpful for establishing intrinsic properties and that potentiostat measurements offer a more robust approach.

Potentiostatic intermittent titration technique (PITT) is a related method for studying diffusion and thermodynamics in lithium batteries. [42] Interfacial resistance is negated since the technique involves small increment voltage steps while monitoring the current associated with the reaction to move to equilibrium before moving to the next step. With PITT, one is able to calculate the diffusion coefficient of Li ions, or more specifically, the mobility of the reaction front during the three-phase reaction step. The beginning of every voltage step in PITT establishes a new concentration at the electrode-electrolyte interface. The current response is a result of maintaining the new concentration at the surface while ions diffuse into the electrode until the whole electrode is at equilibrium with the new concentration. We further support this with diffusion coefficients extracted from electrochemical impedance spectroscopy (EIS) measurements. Both diffusion coefficients were measured using the methods found in Huggin's papers. [42] [46] Identification of the intrinsic hysteresis potential in conversion materials is not a simple endeavor. Intrinsic hysteresis obtained through PITT can be complicated by the presence of a nucleation overpotential to initiate conversion. To overcome these challenges a reverse step potentiostatic intermittent titration technique method was utilized in the identification of the reaction potential hysteresis.

3.2 *Experimental*

3.2.1 Sample Preparation

FeF_2 and FeF_3 were used as received (Advance Research Chemicals) and $FeO_{0.67}F_{1.33}$ was synthesized from a solution of iron metal and fluorosilicic acid and then dried under air as described previously. [31] Carbon nanocomposites of these metal fluorides were prepared by high-energy milling (SPEX 8000). An 85:15 weight ratio between the metal fluoride and activated carbon (Norit A-supra) was placed inside a hardened steel milling cell under He and milled for 30 min. After milling, the composite samples were stored in vials packed under He atmosphere to avoid atmospheric contamination. Electrodes were prepared using the Bellcore method by adding poly(vinylidene fluoride-co-hexafluoropropylene) (Kynar 2801, Elf Atochem), carbon black (Super P, MMM), and propylene carbonate (Aldrich) to the powder in acetone (Aldrich). [63] The slurry was tape cast in a dry room (<1% relative humidity), allowed to dry for 10 min, and rinsed three times in 99.8% anhydrous diethyl ether (Aldrich) to extract the propylene carbonate plasticizer. The electrodes were further dried, under vacuum at 120 °C for 1 hour, to remove any residual moisture. Phase purity of materials was confirmed through the use of X-ray diffraction.

3.2.2 Electrochemical Characterization

Coin cells (2032, Hohsen) were assembled in a He-filled glovebox using Whatman GF/D glass fiber separators saturated with either 1M $LiPF_6$ in ethylene carbonate : dimethyl carbonate (EC:DMC) or 1M $LiBF_4$ in ethyl methyl sulfone (EMS). The metal

fluoride nanocomposite electrode was used as the positive electrode while pure lithium metal (FMC) was used as the negative electrode. Batteries were cycled using MacPile (Biologic), VMP 3 (Biologic), and Arbin cyclers for both potentiostat and galvanostat.

Coin cells were cycled in GITT from 4.25 V to 1.5 V with 7.5 mA/g (based on weight of active material) pulses for 1 hour followed by a 5 hour relaxation between pulses. Typical hysteresis is taken from voltage points after relaxation in which polarization is eliminated.

All materials characterized by PITT were cycled from 4.25 V to 1.5 V using 10 mV step size with a current cut-off of 0.4 mA/g (<C/1000) of active material. The diffusion coefficient, D was calculated by measuring the linear slope of the ln (I) vs time (t) at each voltage step as described in section 1.10. At each voltage step the surface current decays exponentially [42]

$$I(t) = \frac{2z_a FS(C_s - C_o)\widetilde{D}}{L} \exp - \frac{\pi^2 \widetilde{D}}{4L^2} \qquad \textbf{(3.1)}$$

D can then be calculated by taking the linear region in the graph of ln (I) versus t.

$$\widetilde{D} = -\frac{d(\ln(I))}{dt}\frac{4L^2}{\pi^2} \qquad \textbf{(3.2)}$$

Where *I* is the current of the potential step, *t* is time within the potential step and *L* is the diffusion length. In our case we assume our samples are 50 nm spherical particles based on characterization by transmission microscopy.

EIS was measured in the range of potentials between 3.5 V and 1 V using a VMP (Biologic). Cells were discharged for 4 hours at 20 mA/g. Before each measurement the cell was allowed to rest for 10 minutes. The cells were characterized at an amplitude of 10 mV within a frequency range of 200 kHz to 200 µHz. Each spectrum was fitted with a Randle's equivalent circuit (Figure 3.1).As described previously in section 2.3, R_0 is the uncompensated ohmic resistance of the electrolyte and electrode; R_{ct} is the charge-transfer resistance, C_{dl} is the double layer capacitance, Z_w^* is the Warburg impedance. Narquisian impedance spectra show a semi-circle at high frequency which is the combination of R_o and R_{ct}. At very low frequencies a vertical line in which R reaches its limit which is the sum of (R_0 +R_{ct}) and R_L where R_L is the limiting low frequency resistance. [41]

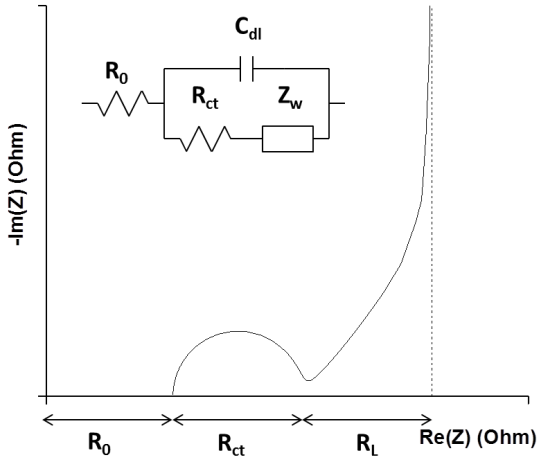

Figure 3.1. An Illustration of Randles circuit.

As mention in section 1.11, the diffusion coefficient can be found from the Warburg impedance:

$$D_{app} = \frac{V_m^2}{2z^2F^2A^2\sigma^2}\left(\frac{dE}{dx}\right)^2 \quad \textbf{(3.3)}$$

To address the degree of correction required to account for charge transfer considerations, we applied the correction factor approach suggested by Montella utilizing both the EIS and PITT data we have collected. [64]

Diffusion coefficients that were determine through the Cottrellian region can be an underestimation because of kinetic limitations from surface processes and ohmic drop. This can be corrected with the following equation: [64]

$$\frac{D_{ap}}{D} = 4\frac{b^2}{\pi^2} \quad \textbf{(3.4)}$$

D_{ap} is the apparent diffusion coefficient, D is the corrected diffusion coefficient, and is the 1st positive root of the following equation:

$$b\tan(b) - \Lambda = 0 \quad \textbf{(3.5)}$$

Λ is the dimensionless parameter. When Λ has a high value ($\log(\Lambda)>1$), $b=\pi/2$ in which the cottrellian response is diffusion control and that interfacial charge transfer and/or ohmic drop is consider negligible, thus $D_{app}=D$. The dimensionless parameter is defined as: [65]

$$\Lambda = \frac{I(0)\cdot\tau_d}{\Delta Q} \quad \textbf{(3.6)}$$

Where *I* (0) is the initial current of the step. ΔQ is the total charge transfer during the step and τ_d is:

$$\tau_d = \frac{L^2}{D} \quad \textbf{(3.7)}$$

3.2.3 Pair Distribution Function (PDF) Analysis

X-ray total scattering data, suitable for PDF analysis, were collected at the beamline 11-ID-B at the Advanced Photon Source, Argonne National Laboratory for electrodes recovered from selected states of lithiation and delithiation. Electrode samples were prepared as described above, cycled galvanostatically at 60 °C at 50 mA/g (with respect to the nanocomposite) for FeF_2 and $Fe_{0.67}F_{1.33}$ and at 7.5 mA/g for FeF_3, removed from the coin cell, transferred to an inert X-ray sample environment and mounted on the instrument perpendicular the beam. High-energy X-rays (λ = 0.2114 Å) were combined with a large area detector (Perkin-Elmer amorphous-silicon) to collect data to high values of momentum transfer with exposure times of 5 min. [66] [67] The scattering images were reduced to one-dimensional data within fit2d. [68] [69] The data were corrected for background scattering, Compton scattering and detector effects within PDFgetX2 and Fourier transformed to Q_{max} = 19 $Å^{-1}$ to obtain the PDF, *G(r)*. [70] Structural models were refined against the PDF data within PDFgui. [71]

Comprehensive structural phase analyses have been performed for a series of samples recovered following the 1st, 2nd, 10th, and 20th lithiation and delithiation processes. The detailed results of these analyses will be reported elsewhere. Here, we focus on the structural models refined for the rock salt LiF component(s).

3.3 *Results*

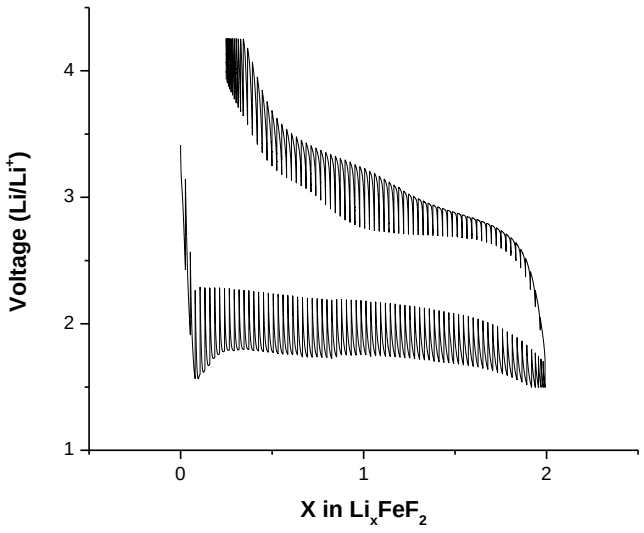

Figure 3.2. GITT of FeF_2—C nanocomposites, 7.5 mAh/g with 1h cutoff follow by 5 h open circuit relaxation at 25 °C.

3.3.1 GITT

FeF2—C nanocomposites were pulsed in GITT mode during lithiation and delithiation for 1 hour at 7.5 mA/g with a 5 hour relaxation between pulses at 25 °C shown in Figure 3.2. The overpotential before the ~1.8 V plateau corresponds to nucleation and growth of the 2LiF + Fe product of the conversion reaction. [72] The average OCV (Open Circuit Voltage) upon lithiation is ~2.2 V from x = 0.25-1.5. On delithiation, the average OCV was 2.7 V from x = 1.75-1. Traditionally, post pulse OCV such as these have been presented as an indication of the true hysteresis of the reversible conversion reactions. Upon closer inspection, however one can see (FeF2 x = 0.25 in Figure 3.3) that the voltage during relaxation has not truly relaxed to an

equilibrium value. Compared to the theoretical value (V_{th} = 2.66 V), the relaxation voltage after 5 hours is about 2.28 V. The true relaxation voltage can be approached by allowing a longer relaxation time or by increasing the temperature which in turn will increase the kinetics and thus drive the reaction closer to equilibrium potential. EMS was used for electrochemistry at temperatures 60 °C and greater because of the solvent stability up to 220 °C. [73] The effect of temperature on the voltage polarization and hysteresis is also seen in Figure 3.3. The polarization induced voltage during the lithiation pulse is systematically decreased (from 2.28 to 2.53 V) with an increase in temperature (from 25 to 100 °C). More importantly, from the context of this chapter, the kinetics of the relaxation was much improved revealing that the room temperature relaxation values established through GITT at 25 °C are far from equilibrium. Even though the response at 100 °C is much faster, no equilibrium value have been reached.

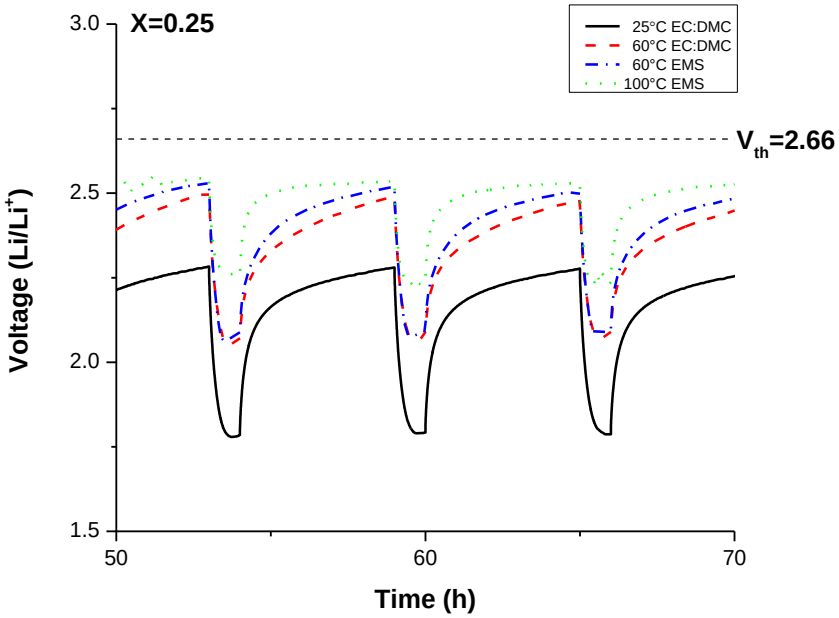

Figure 3.3. GITT of FeF_2—C nanocomposites during lithiation at various temperatures, 7.5 mAh/g with 1h cutoff follow by 5h open circuit. Shown at x=0.25 in Li_xFeF_2. 1M $LiPF_6$ in EC:DMC was used at 25 °C and 60 °C while 1M $LiBF_4$ in EMS was used at 60 °C and 100 °C.

In order to gain a greater insight into the true equilibrium value, the lithiation and delithiation profiles of the relaxation were fitted for each temperature. Results show that the relaxation curves from lithiation and delithiation require extraordinarily long times to access a near equilibrium value. Extension of the fits for approximately 10 days shown in Figure 3.4 reveals that, within error of the extensive fit, relaxation potentials approach an equilibrium value near 2. 6 V and no intrinsic hysteresis can be determined using the relaxation technique. This should be expected, as the relaxed value of a true conversion reaction during GITT should not be indicative of any hysteresis when comparing the delithiation and lithiation reaction. However, the “on”

pulse in GITT gives excellent insight into overpotential + hysteresis characteristics. Indeed, the conversion reaction may require a minimum potential to activate a reaction pathway even at near equilibrium rates. As such, well controlled PITT may represent a better path of understanding as the potential is controlled and the limiting potential required to induce the onset of the reaction can be identified.

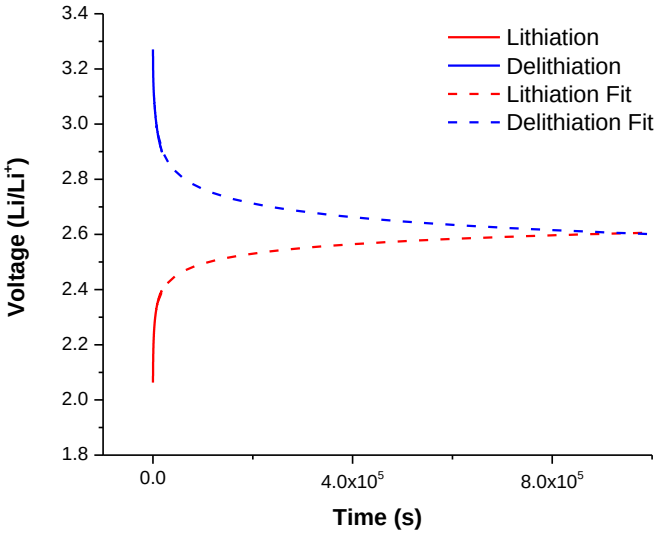

Figure 3.4. Fit of the relaxation curve of FeF_2—C nanocomposites GITT at 60 °C at x=1 in Li_xFeF_2. Electrolyte was $LiBF_4$ in EMS.

3.3.2 PITT

Figure 3.5 shows the voltage profile of FeF_2—C nanocomposite electrode characterized utilizing a very slow rate PITT discharge where a typical lithiation reaction requires 2 months. The voltage steps down in small 10 mV steps and does not continue to the next step until the current decays to <0.4 mA/g (approximately C/1000). Commencing with an initial OCV of 3.39 V, the discharge proceeds without any

significant increase in the current until 1.84 V. At this potential the entire $FeF_2 \rightarrow 2LiF + Fe$ reaction proceeds to near completion in a single 10 mV step. [33] [30] In sharp contrast to this lithiation behavior, even at the very low C/1000 rate, the delithiation proceeds in a more solid solution like manner over many steps. This data is strong evidence that the delithiation reaction proceeds in a mechanism which is unlike the lithiation reaction. Before making such a conclusion, the second lithiation was investigated due to the considerable polarization observed in the first lithiation for most conversion materials. The second lithiation reveals a small 3 V reaction shown in Figure 3.6. This is attributed to a small degree of Fe^{3+} formation as a result of Fe^{2+} loss through dissolution. [33] Again, the conversion step is seen to proceed in a single step reaction that occurs entirely within a 10 mV step. However, the onset potential of this step at 2.09 V is significantly higher than the first lithiation. This shift in conversion potential can be attributed to the significantly finer nanostructure of the reformed FeF_2 particles undergoing conversion, typically 10 nm vs 20 nm. As such, a smaller nucleation overpotential may be required.

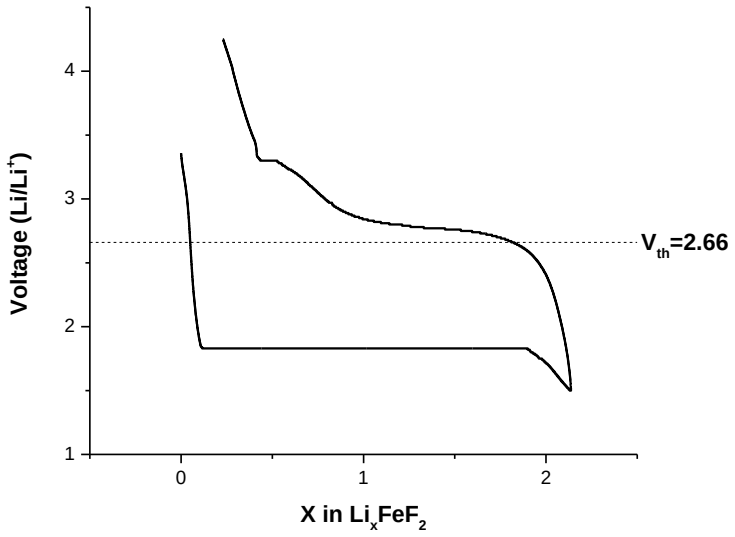

Figure 3.5. First PITT cycle of FeF_2—C nanocomposites, 10 mV step 0.4 mA/g current cutoff at 25 °C.

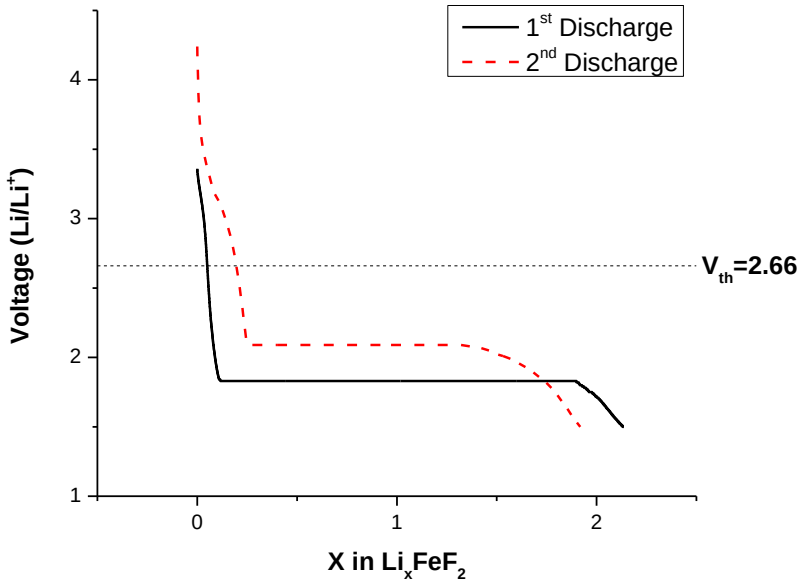

Figure 3.6. First and second PITT discharge of FeF_2—C nancomposites, 10 mV step 0.4 mA/g current cutoff at 25 °C.

Iron (III) fluoride (FeF_3) was investigated as a contrasting case of conversion. Figure 3.7 is the voltage profile of FeF_3—C nanocomposite electrode under similar 10 mV step PITT conditions. The PITT lithiation commenced at an OCV of 3.63 V. A lithium insertion reaction commences at 3.36 V. There the lithium inserts in a two-phase reaction as evidenced by the quasi plateau of potential steps. This proceeds to approximately x = 0.242 in Li_xFeF_3. This is consistent with the two phase reaction leading to a defective rutile like structure of an approximate composition of $Li_{0.5}FeF_3$. [30] [54] [72] Further lithiation forms a metastable solid solution of $LiFeF_3$. At 1.89 V, the conversion process of $LiFeF_3 \rightarrow 3LiF + Fe$ proceeds in a single 10 mV step, although a bit short of full completion. This is remarkably similar to the 1.84 V onset potential of conversion observed for the FeF_2 material. This is also consistent with previously reported data which the plateau represents the reduction of Fe^{2+} to Fe^0. [30] [74] As with FeF_2, the delithiation occurs over a large multitude of small 10 mV steps, far from the behavior one would expect in a "reconversion" reaction. As an aggregate of small steps, this delithiation proceeds with two general plateau-like areas in contrast to FeF_2. This suggests origins in the $Fe^o \rightarrow Fe^{2+}$ and Fe^{2+} to Fe^{3+} redox reactions. On the second lithiation, there is no indication of a $Li_{0.5}FeF_3$ phase formation via plateau formation at the higher voltage regions (Figure 3.8). This is consistent with the reported spectroscopy which indicates that the reconverted FeF_3 is more rutile like in nature thus not requiring the structural transformation observed in the first lithiation of the ReO_3-like FeF_3 original phase. FeF_3 experiences a higher onset potential for conversion during the

second cycle associated with the smaller crystallite size formed following reconversion.

[30] [72]

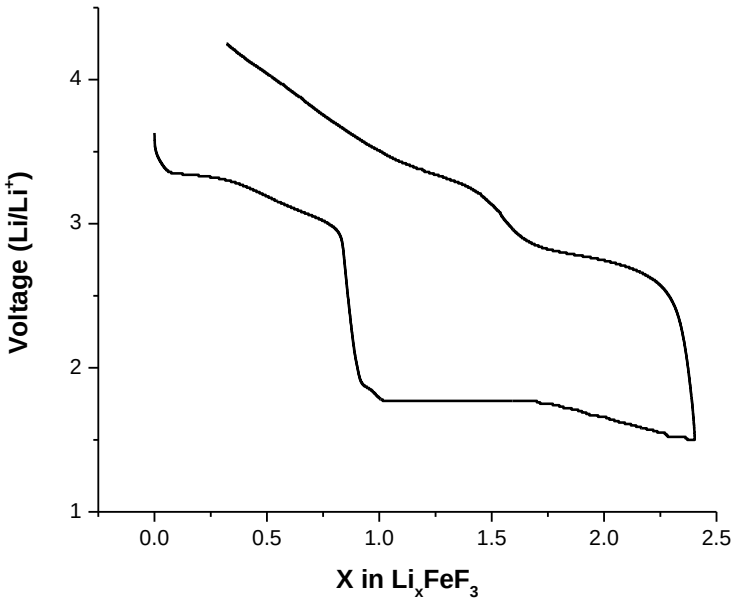

Figure 3.7. First PITT cycle of FeF_3—C nancomposites, 10 mV step 0.4 mA/g current cutoff at 25 °C.

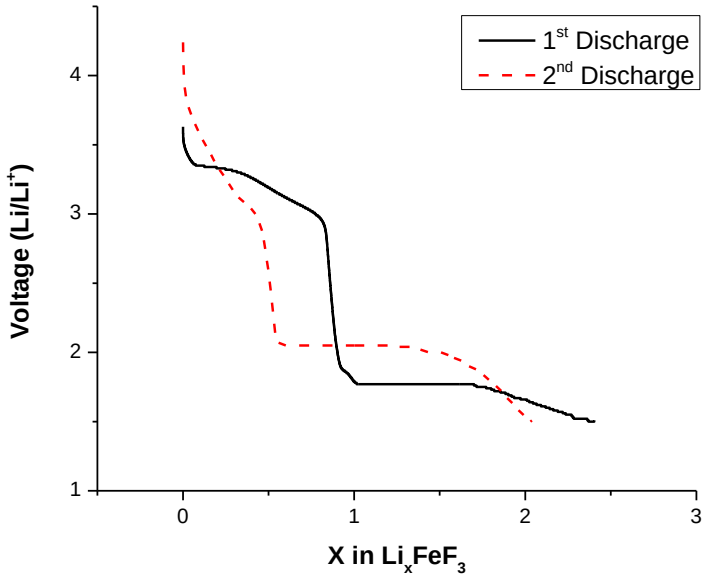

Figure 3.8. First and second PITT discharge of FeF_3—C nanocomposites, 10 mV step 0.4 mA/g current cutoff at 25 °C.

$FeO_{0.67}F_{1.33}$ was investigated as a hybrid between FeF_2 and FeF_3 in which the Fe^{3+} exists in a FeF_2 rutile structure instead of the ReO_3 structured FeF_3. $FeO_{0.67}F_{1.33}$ has a starting OCV of 3.54 V. Upon lithiation under PITT protocol, $FeO_{0.67}F_{1.33}$ proceeds with solid solution like behavior as lithium is inserted into the structure forming a lithiated rocksalt type phase ($Li_{0.7}FeO_{0.7}F_{1.3}$). This seems contrary to expected behavior but will be discussed in more detail in the discussion. The reaction potential is consistent with lithium insertion to reduce $Fe^{3+} \rightarrow Fe^{2+}$. [31] This proceeds until x = 0.516 in $Li_xFeO_{0.67}F_{1.33}$ where the onset of the "conversion" reaction occurs at 2.1 V, significantly higher than the onset potential of either FeF_2 or FeF_3 during the first lithiation. As opposed to the conversion reaction proceeding to completion in one single 10 mV step for the conversion reaction of FeF_2 or FeF_3 in the first or second lithiation, numerous potentials

are required (Figure 3.9) for the conversion reaction of $FeO_{0.67}F_{1.33}$ to fully proceed. As such, the $FeO_{0.67}F_{1.33}$ material displays a distinctly unique conversion behavior during lithiation. The higher onset potential of the conversion can be explained by spectroscopic evidence suggesting that the rocksalt phase and possibly the Fe metal is already present in the latter part of the lithium insertion reaction which occurs at higher potentials than the conversion reaction. [75] [52] As such, these phases are already nucleated before the conversion step. The conversion reaction, consisting of many small plateaus, can be attributed to compositional changes with new phases forming from conversion or from the gradient of oxygen in the composition. [76] This will be discussed in further detail below within the discussion.

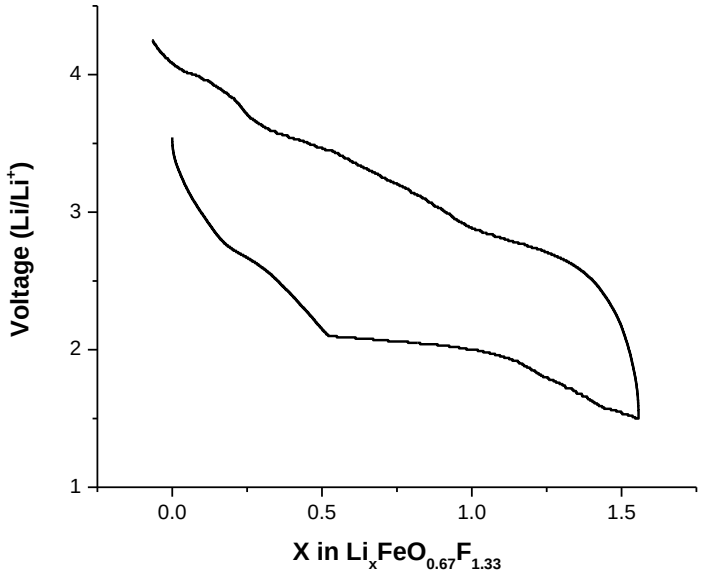

Figure 3.9. First PITT cycle of $FeO_{0.67}F_{1.33}$—C nanocomposites, 10 mV step 0.4 mA/g current cutoff at 25 °C.

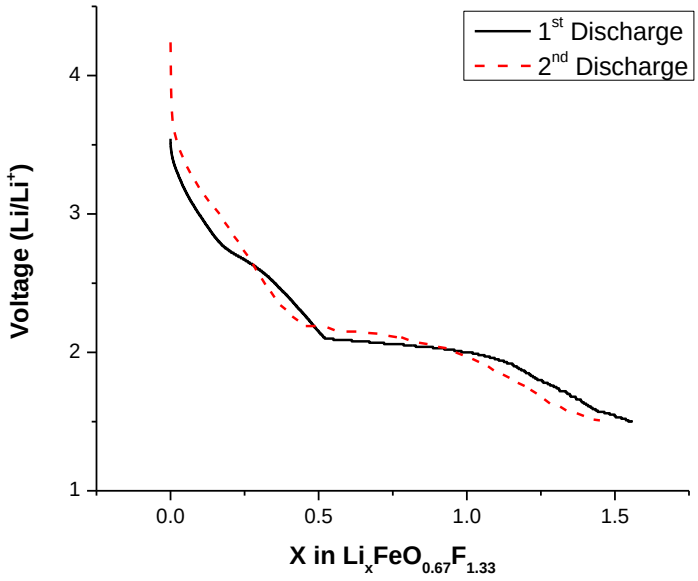

Figure 3.10. First and second PITT discharge of $FeO_{0.67}F_{1.33}$—C nanocomposites, 10 mV step 0.4 mA/g current cutoff at 25 °C.

The delithiation reaction of $FeO_{0.67}F_{1.33}$ is very similar to that of FeF_3 and FeF_2 in that it is composed of hundreds of small 10 mV regions clearly showing the potential is changing systematically with compositional change. It is similar to the delithiation of FeF_3 in that it has two regions that can be attributed to the oxidation of the Fe. Indeed, the approximate location of these segments are consistent with $Fe^0 \rightarrow Fe^{2+}$ and $Fe^{2+} \rightarrow Fe^{3+}$ oxidation regions as shown by in-situ Mossbauer. [77] The second lithiation shows a higher voltage region of quite different potential dependence than the first lithiation. This may be in part attributed to small amounts of rocksalt phase known to be present during the delithiation and the nanostructure is near amorphous therefore leading to insertion with minimal reconstruction. [75] In sharp contrast to the FeF_2 and FeF_3, $FeO_{0.67}F_{1.33}$ shows very little change in the onset potential of the second cycle

conversion relative to the first lithiation. This gives support to the fact that the preconversion structure is highly favorable for the conversion reaction to proceed in the case of $FeO_{0.67}F_{1.33}$. As from Figure 3.10, $FeO_{0.67}F_{1.33}$ maintains the same voltage profile during the second lithiation as with the first with the exception of a higher conversion voltage at 2.19 V from the reduced particle size.

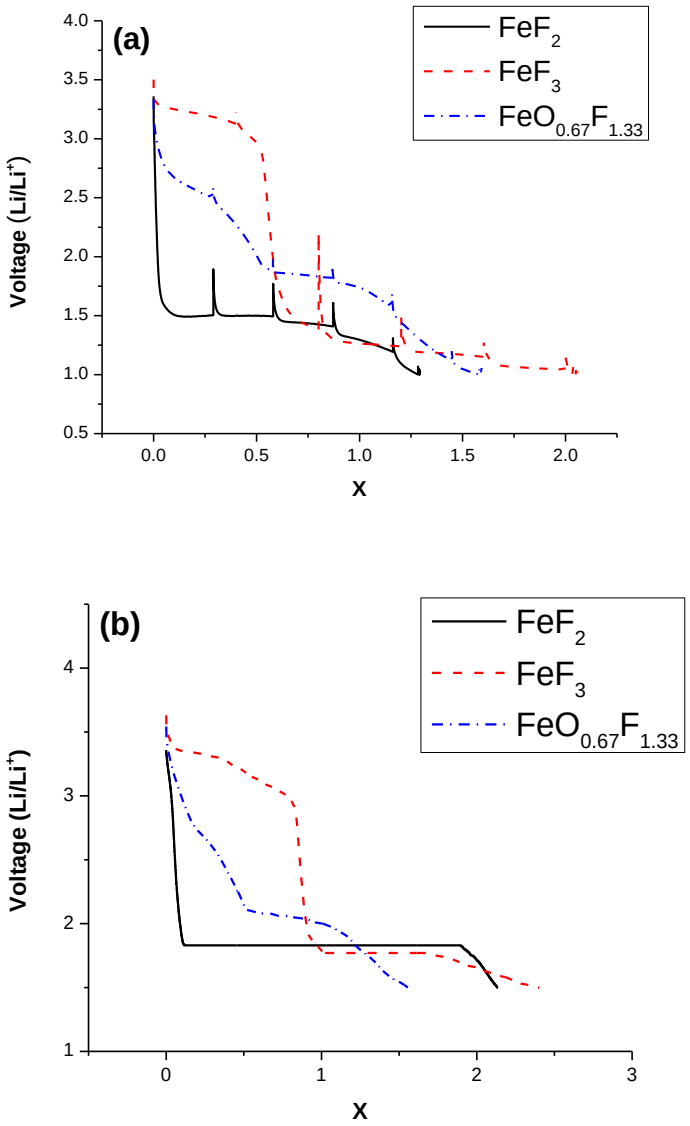

Figure 3.11. Voltage profile of x in Li_xFeF_3, Li_xFeF_2, and $Li_xFeO_{0.67}F_{1.33}$ taken from: (a) EIS and (b) PITT analysis.

3.3.3 Diffusion Coefficients

Diffusion coefficients were extracted from the PITT data. As a benchmark, EIS was also used to calculate the diffusion coefficients. It is certainly well known that PITT derived diffusion coefficient in multiphase reactions is not a direct representation of D_{Li}

but rather an effective diffusion coefficient or pseudo diffusivity coefficient which reflects the interface movement and the diffusion of other species. PITT has been demonstrated as an acceptable approach for the study of interface mobility in a number of multiphase electrode reactions [78] [79] [80] [81] [82] [83] [84] [85] and also against it if not corrected for charge transfer effects [64] [65] [86], as discussed below. Some theorize the small region of Cottrellian behavior observed within the PITT response of multiphase reactions is due to a localized range of solid solutions reactions occurring at a very small length scale where the interface moves forward, thus fundamentally dependent on diffusion processes. Regardless of the true nature of the correlation, the diffusion coefficient derived by PITT in multiphase behavior has been seen to be remarkably close to true time scales of the reactions and similar (within to order of magnitude) to corrected methodologies in many published accounts. We only utilize the Cottrellian – like linear behavior region within the non-Cottrellian current evolution, which is typical of multiphase reactions. Indeed, the results from PITT contain a collection of transport phenomena including the bulk diffusion of lithium and other species which contribute to the boundary diffusion as described above and also charge transfer. The latter is the latest focus of correction as it impacts the interpretation of the voltage step intrinsic to the PITT technique. In certain transport scenarios, interface resistance could lead to a source of serious underestimation of the bulk diffusion coefficient. [64] The basis for this rests in an uncorrected charge transfer and solution resistance, which affects both the short-term and long-term current decay response and thus the calculation of the diffusion coefficient. This can be corrected by the use of the

dimensionless parameter (Λ), where if there is little charge transfer resistance relative to diffusion, large Λ, no correction is needed, where the opposite is enacted for contrasting situations. This theory was also used as a correction factor by Dell'Era et al. and others. [81] Alternative methodologies have been developed by Vorotyntsev et al., [65] Li et al. [86] utilizing a Biot number correction and others. Following the approach by Montella detailed in the experimental section, our calculations revealed large Λ for all three model materials. For example, the dimensionless parameter was found to be 84 for FeF_2, which indicate a bulk diffusion controlled process and no correction required.

Figure 3.11 is a comparison of the voltage profiles observed during the intermittent EIS and PITT. Both have similar voltage profiles. The only difference arises from the x value which is a direct result of the faster discharge rate on the cells used for EIS. The calculated diffusion coefficients from both PITT and EIS are shown in Table 3.1. The values are mostly similar, being within at most 1 order of magnitude to each other.

It is possible that this discrepancy is due to the fact that the EIS measurements were taken when the samples were not in full equilibrium as impedance was taken after a constant current discharge.

Comparing the PITT observed results for FeF_2 and FeF_3; FeF_2 had a diffusion rate of 4.04 x 10^{-18} cm^2/s, FeF_3 had a rate of 1.71 x 10^{-18}. It is understandable that FeF_2 is faster as it can demonstrate higher C-rates as a result of less LiF molarity to diffuse through in the converted compound. $FeO_{0.67}F_{1.33}$ diffusion rate is 3.19 x 10^{-18} cm^2/s which is close to

that of FeF_2 although $FeO_{0.67}F_{1.33}$ can demonstrate faster C-rate which seems to suggest that the limitation is not due to lithium diffusion and that the large series of multiphasic reactions seen from PITT is benefiting overall reaction kinetics. In general, all coefficients are quite low thus supporting the requirement for nanomaterials and nanocomposites to enable practical rate reactions to proceed.

Region	PITT Diffusion Coefficient (cm^2/s)	EIS Diffusion Coefficient (cm^2/s)
FeF_2—C		
Conversion	4.04E-18	1.01E-19
FeF_3—C		
Insertion	2.32E-17	3.21E-18
Conversion	1.71E-18	1.66E-18
$FeO_{0.67}F_{1.33}$—C		
Insertion	9.35E-17	1.99E-17
Conversion	3.19E-18	8.89E-19

Table 3.1. Diffusion coefficient of FeF_2, FeF_3, $FeO_{0.67}F_{1.33}$ extracted from PITT and EIS characterization.

3.3.4 Reverse Step PITT

In PITT, voltage is controlled while the current is monitored to eliminate the polarization effect seen in galvanostatic mode. The goal is to identify the absolute minimum potential it takes for the reaction to proceed forward in order to accurately define “hysteresis” vs. kinetically induced polarization. However, as shown above, in some of the conversion materials, there is a significant amount of overpotential that must be addressed in order to initiate the conversion process. In PITT, after the

initiation of reaction the reaction then proceeds at a voltage which may be in considerable excess of the subsequent true potential needed to carry out the reaction. As such, it would be fruitless to utilize this potential to calculate intrinsic hysteresis between the lithiation and delitiation reactions.

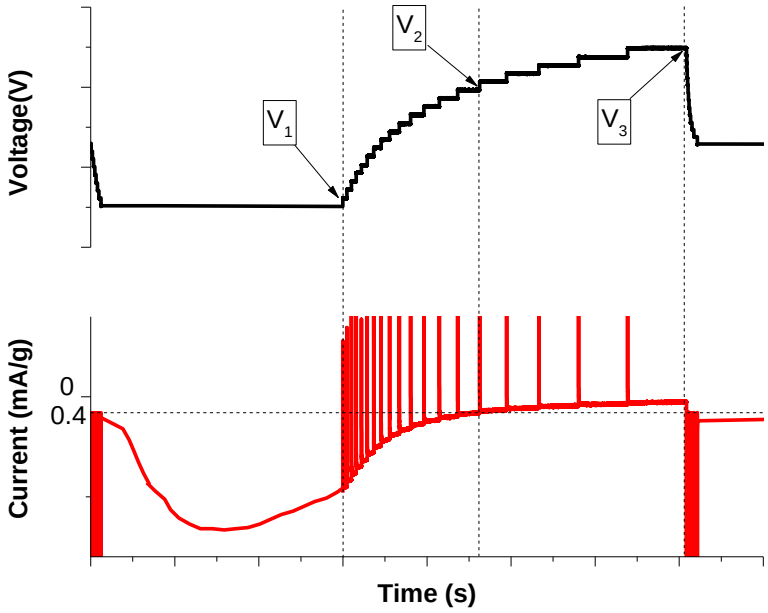

Figure 3.12. Typical Reverse step PITT voltage profile during lithiation. V_1, V_2, and V_3 are voltages at: initiation of reverse step PITT, the current decay to 0.4 mA/g, and the point where the cell is unable to discharge 3 mAh/g within 18 hours in a single step.

It has been noted that FeF_2 and FeF_3 have an overpotential which is associated with nucleation and growth. [72] In order to separate the hysteresis from this initial "nucleation – like" activation overpotential we employed reverse step PITT. In reverse step PITT we commence with the same conditions as normal PITT, i.e. lowering the

voltage in (10 mV / 0.4 mA/g current cutoff) steps until a certain predefined capacity is reached. At that point (V_1), we reverse the 10 mV voltage step direction and continue until the cell is unable to discharge 3 mAh/g within 18 hours in a single step. Generally the current at this point is ~C/3000 and is labeled as "V_3" in Figure 3.12. V_2 is noted as the point in which the current has dropped to 0.4 mA/g (C/1000). Afterwards, PITT in the original direction is resumed. By reversing the step direction, we eliminate lithiation driven by overpotential required by the initial nucleation. Indeed, lithiation still occurs but at a much slower rate for every 10 mV step in the reverse direction. Eventually, conversion lithiation reaction cannot proceed as the potential is too high. The voltage found at "V_3" is determined to be the true reaction activating potential. Hysteresis is found by taking the difference of "V_3" found in the lithiation and delithiation direction at similar lithium contents (Li_x). In our study, cells were lithiated 10 mV steps with a 0.4 mA/g (<C/1000) current cut-off until the following capacities are reached: 100, 198, 200, 290, 450, and 480 mAh/g of active material. The true reaction hysteresis was determined by finding the true activating voltage in lithiation and delithiation at the same lithium concentration.

	Capacity (mAh/g)	X	V_1 (V)	V_2 (V)	V_3 (V)	V_3-V_1 (V)
FeF_2						
Lithiation						
	25	0.09	1.86	2.02	2.07	0.21
	25	0.09	1.86	2.04	2.06	0.20
	100	0.35	1.89	2.00	2.07	0.18
	100	0.35	1.89	2.00	2.06	0.17
	200	0.70	1.85	2.00	2.05	0.2
	200	0.70	1.93	2.03	2.11	0.18
	450	1.58	1.82	1.94	1.99	0.16
2^{nd} Lithiation	100	0.35	2.18	2.27	2.33	0.15
EC:DMC 60 °C	200	0.70	2.28	2.43	2.46	0.18
EC:DMC 60 °C	200	0.70	2.07	2.23	2.29	0.22
EMS 60 °C	200	0.70	2.13	2.26	2.29	0.16
EMS 100 °C	200	0.70	2.28	2.42	2.46	0.18
Delithiation						
	450	1.58	2.73	2.72	2.71	0.02
	450	1.58	2.73	2.72	2.70	0.03
	200	0.70	3.38	3.37	3.33	0.05
	100	0.35	3.86	3.85	3.82	0.04
FeF_3						
Lithiation						
	100	0.42	3.22	3.23	3.26	0.04
	100	0.42	3.22	3.22	3.26	0.04
	290	1.22	1.73	1.87	2.03	0.30
	480	2.02	1.73	1.76	1.91	0.18
Delithiation						
	290	1.22	3.36	3.35	3.29	0.07
$FeO_{0.67}F_{1.33}$						
Lithiation						
	100	0.34	2.79	2.80	2.80	0.01
	198	0.68	2.23	2.25	2.25	0.02
	198	0.68	2.09	2.10	2.12	0.03
	290	0.99	2.03	2.06	2.08	0.05
Delithiation						
	290	0.99	2.78	2.77	2.76	0.02
	290	0.99	2.79	2.79	2.76	0.03
	290	0.99	2.68	2.67	2.64	0.04
	198	0.68	3.09	3.08	3.06	0.03
	198	0.68	3.15	3.14	3.12	0.03
	198	0.68	3.01	3.00	2.98	0.03

Table 3.2. Reverse step PITT of FeF_2, FeF_3, $FeO_{0.67}F_{1.33}$ at various capacities. *Note*: Duplicate cells are reported to show reproducibility

Capacity (mAh/g)	Lithiation V_3 (V)	Delithiation V_3 (V)	(ΔV) Reaction Hysteresis (V)
FeF_2			
100	2.07	3.82	1.75
200	2.05	3.33	1.28
450	1.99	2.71	0.72
FeF_3			
290	2.02	3.29	1.27
$FeO_{0.67}F_{1.33}$			
198	2.12	2.98	0.86
290	2.08	2.64	0.56

Table 3.3. Table of calculated reaction hysteresis.

The voltage points collected from reverse step PITT for FeF_2, FeF_3 and $FeO_{0.67}F_{1.33}$ are shown in Table 3.2. The reaction hysteresis was extracted by finding the difference in voltages at V_3 found in both lithiation and delithiation for each specific capacity. This is shown for each material in Table 3.3. Reverse step PITT was performed at three points in the two-phase lithiation reaction for FeF_2 cycle (100, 200, 450). Voltage profiles can be seen in Figure 3.13. Results indicate that the FeF_2 conversion reaction was initiated at ~1.85 V and continued until it reach the targeted capacities. Voltage steps were reversed at the targeted capacity and the reaction persisted until the potential was raise to ~2.05 V, at which the cell is no longer able to maintain conversion. This large 200 mV difference is consistent with the “nucleation – like” overpotential shown in Figure 3.2. In

addition, all cells exhibit a higher potential for the reaction to move forward when resuming normal direction PITT reaction as continued reaction proceeds from the prenucleated conversion front. In sharp contrast, the points taken on delithiation revealed that FeF_2 was able to maintain reconversion for only a very short period after reversing the step potential downward. The potential difference (V_3 - V_1) in delithiation is very much lower than on lithiation (50 mV as opposed to 200 mV). This is mainly from the lack of a "nucleation – like" overpotential as seen in lithiation. Since the reaction pathway is different on delithiation, the voltage "V_3" will differ significantly depending on x in Li_xFeF_2.

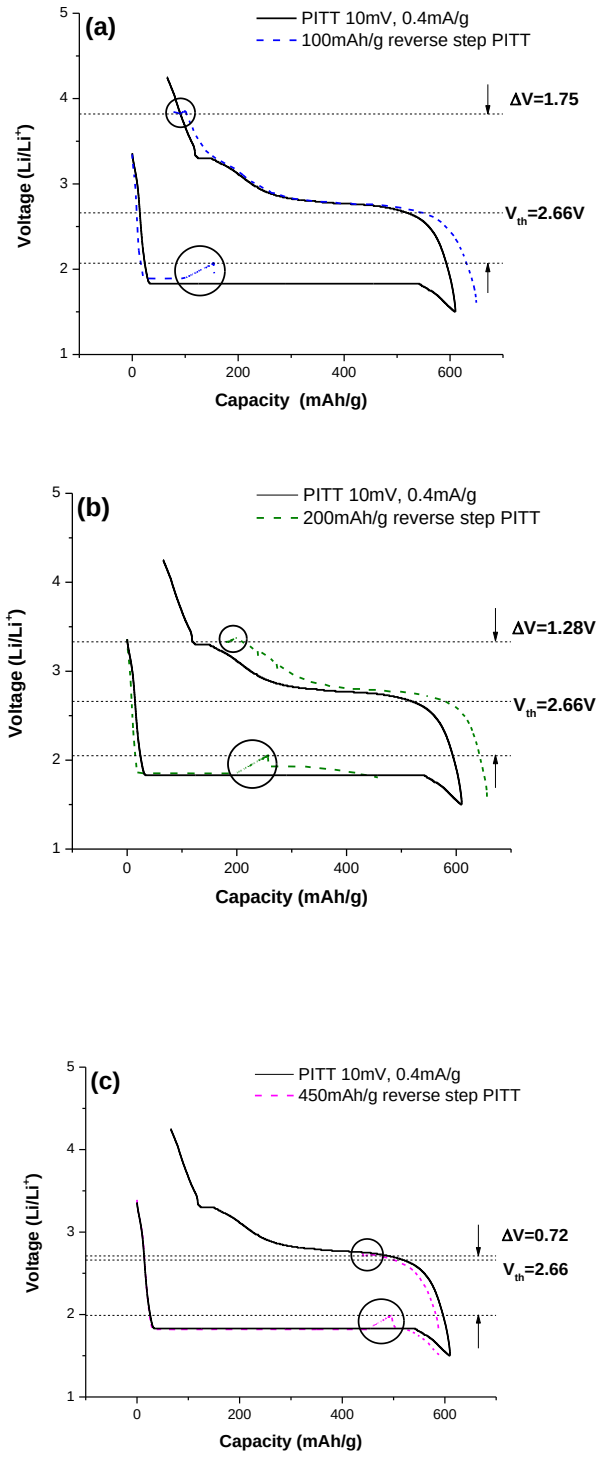

Figure 3.13. Reverse step PITT of FeF_2 with its normal PITT overlay for capacities, the reverse step PITT portion are indicated with circle: (a) 100 mAh/g (x=0.35), (b) 200 mAh/g (x=0.70), (c) 450 mAh/g (x=1.58).

The reaction hysteresis taken at 200 mAh/g (0.7 mol Li) is 1.28 V, whereas the hysteresis found at 100 mAh/g (0.35 mol Li) is 1.75 V as shown in Table 3.3. Compared to the thermodynamically derived theoretical FeF_2 conversion potential of 2.66 V for FeF_2, the V_3 value on delithiation is much closer (50 mV) to the theoretical potential than on lithiation (830 mV) at the 450 mAh/g data point. In contrast, the values for 100 mAh/g show that the difference for delithiation is larger than for lithiation (1.16 V vs. 0.59 V).

Referring to Table 3.2, FeF_3 was able to maintain lithiation by conversion reaction when the voltage was reversed and increased by 300 mV in its conversion region (290 mAh/g). In contrast, the voltage only stepped up 40 mV before the lithiation reaction stopped when reverse step PITT was performed during the initial lithium insertion, non-conversion, region at 100 mAh/g. Similar to FeF_2, the "nucleation – like" overpotential is what contributes to the large potential difference seen in the conversion region. [74] Also FeF_3 exhibits a higher potential (1.83 V) at 380 mAh/g when resuming downward PITT for lithiation than the potential observed at the start of reverse step PITT (1.73 V) as shown in Figure 3.14. Reverse step PITT did not have much effect on delithiation, at 290 mAh/g FeF_3 was only able to maintain reconversion for a 70 mV decrease in voltage. From Table 3.3 the reaction hysteresis at 290 mAh/g is 1.27 V.

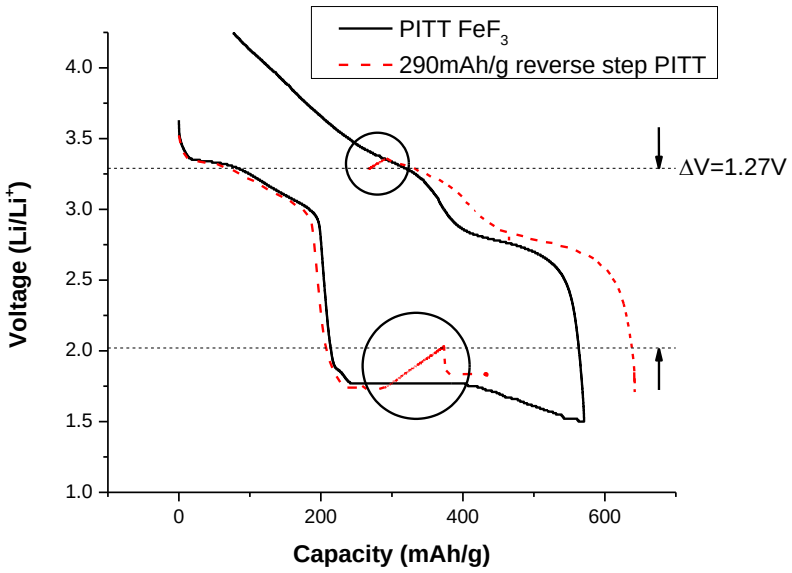

Figure 3.14. Reverse step PITT of FeF_3 with its normal PITT overlay for 290 mAh/g (x = 1.22) in the conversion region, the reverse step PITT portion is indicated with circle.

In $FeO_{0.67}F_{1.33}$, reverse step PITT was performed at 198 mAh/g in the insertion region and 290 mAh/g in the conversion region. Voltage profiles of both are shown in Figure 3.15. In the insertion region, the $FeO_{0.67}F_{1.33}$ reaction quickly ceases after the potential was increased by only 20 mV. For the conversion region, unlike FeF_2 or FeF_3, the voltage increased only 50 mV before the reaction ceased, in sharp contrast to the large values of FeF_2 and FeF_3. This is also in agreement with its voltage profile as $FeO_{0.67}F_{1.33}$ has no overpotential as seen in FeF_2 and FeF_3. [31] On delithiation, both measurements taken at 198 and 290 mAh/g reveal that $FeO_{0.67}F_{1.33}$ was only able to maintain reconversion with a small difference in potential (<50 mV difference). From

Table 3.3, the conversion reaction hysteresis found at 290 mAh/g (x = 0.797) is 0.56 V much lower than the hysteresis values observed for FeF_2 and FeF_3 conversion.

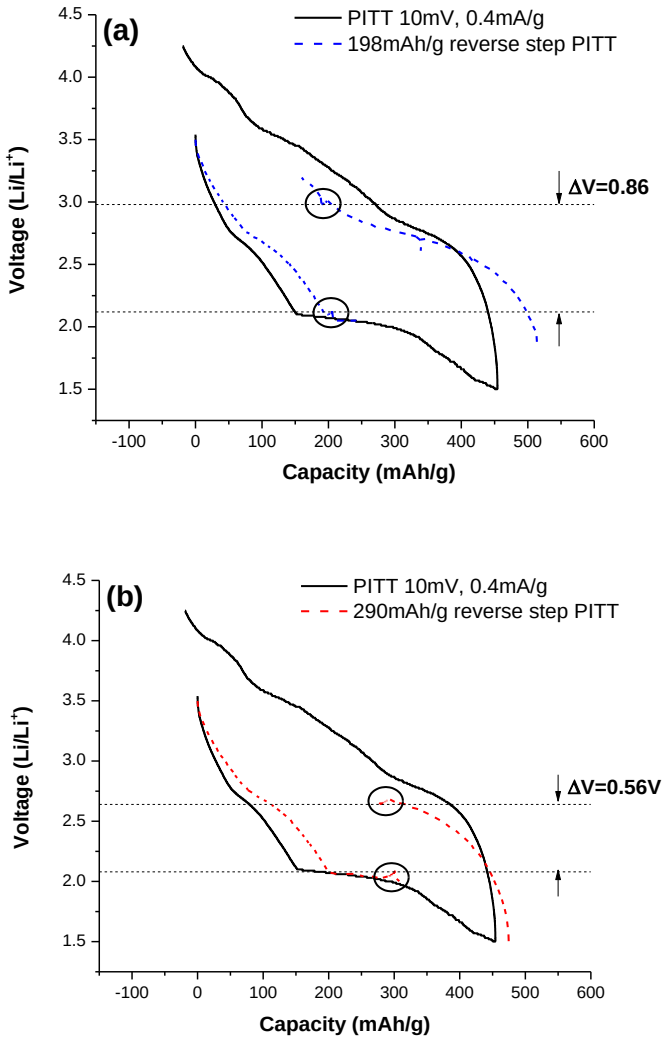

Figure 3.15. Reverse step PITT of $FeO_{0.67}F_{1.33}$ with its normal PITT overlay for capacities, the reverse step PITT portion are indicated with circle: (a) 198 mAh/g (x = 0.68) in the insertion region, (b) 290 mAh/g (x = 0.99) in the conversion region.

3.4 *Discussion*

3.4.1 PITT and Reaction Mechanisms

Insight regarding the progression of phases and their respective electrochemical potential can be extracted by thermodynamics and Gibb's phase rule as presented in early work by Huggins and others. [87] [88] [89] The phase rule, F = C – P + 2 where F is defined as the degrees of freedom, C number of components, P number of phases can be reduced to F = C - P under conditions of constant temperature and pressure. In the case of single phase topotactic insertion such as Li_xTiS_2, C = 2 (Li^+ guest and TiS_2 host), P = 1and thus F = 1. The electrochemical potential and phase composition will change as a function of lithiation. If two phases form such as in the $Li_4Ti_5O_{12}/Li_7Ti_5O_{12}$ reaction, F = 0, the potential and phase composition, will remain the same as a function of lithiation. Conversion reactions are interesting as they seemingly represent a case of C = 2 (Li and FeF_2) and P = 3 (FeF_2/Fe/LiF) resulting in F = -1. However, in this case it is apparent that there are two moving species, the Li^+ and either Fe^{2+} or F^- to allow the conversion reaction to proceed. This represents a case of C = 3 (Li, Fe, F) and P = 3 resulting in F = 0 and a constant potential as a function of lithiation. Such a situation is undoubtedly consistent with the experimental results of this chapter with the near complete conversion of FeF_2 and $LiFeF_3$ within a span of 10 – 20 mV, even when corrected for overpotential.

The reaction mechanism becomes increasingly complex as we move to the delithiation reaction of these conversion fluorides. Examination of the high resolution

PITT with C/1000 current cutoff clearly shows that for FeF_2 and FeF_3, the delithiation reaction requires a systematic increase in the potential with small degrees of constant potential, most within a $\Delta x << 0.2$, representing multiphase equilibrium reactions. This is much more apparent in the case of FeF_3 where the Δx is $<< 0.1$ for the entire delithiation reaction. Although small, the constant potential vs composition plateaus are not insignificant. This suggests small compositional windows of phase equilibrium. For FeF_2, one could imagine a delithiation reaction scenario following (2) vs. the overall reaction of (1). As a function of delithiation, a multiphase reaction results in an increasing, but not complete degree of delithiation. This phase could be envisioned as Fe^{2+} inserted into the rocksalt LiF, after which a rutile phase is formed upon reaching a Fe saturation threshold. Although the transformation back to rutile FeF_2 has been experimentally confirmed in numerous studies, [33] [34] [30] we explored whether there was evidence of a rocksalt solid solution precursor to such a transformation.

$$2LiF + Fe \rightarrow FeF_2 + 2Li^+ \quad (1)$$

$$2LiF + Fe \rightarrow (1-x)Fe + Fe_xLi_{2-2x}F_2 + 2xLi^+ \quad (2)$$

PDF was utilized to explore the delithiation reaction in detail. At the end of FeF_2 lithiation processes, the expected rocksalt-type LiF phase is evident in the PDF data, with a refined lattice parameter of *ca.* 4.035 Å as shown in Figure 3.16 in close correspondence with the literature values (a = 4.03 Å). Although rocksalt-type LiF is expected to be completely consumed by the delithiation reaction resulting in the reformation of rutile FeF_2, delithiation was found to be incomplete as evidenced by a

small amount of residual metallic Fe and rocksalt phase. The rocksalt phase observed upon delithiation has a significantly (~1.4%) larger lattice parameter (a = 4.09 Å) than for lithiation (or pristine LiF). Preliminary in-situ data which will be reported elsewhere indicates Fe insertion into LiF precedes the formation of rutile FeF_2. The LiF lattice parameter grows progressively in the initial stages of delithiation suggesting a Fe-LiF with progressively increasing Fe content. Fe-LiF can be observed without the presence of rutile but not rutile without Fe-LiF. The increase in the LiF rocksalt lattice dimension can be attributed only to a change in its composition, that is insertion/substitution of Li cations by larger Fe cations (likely Fe^{2+}), i.e., $Fe_xLi_{2-x}F_2$. Both the electrode composition and the lattice parameter of the rocksalt phase positively exclude the possibility that this is an unrelated rocksalt (e.g., $LiFeO_2$, $a \approx 4.3$ Å).

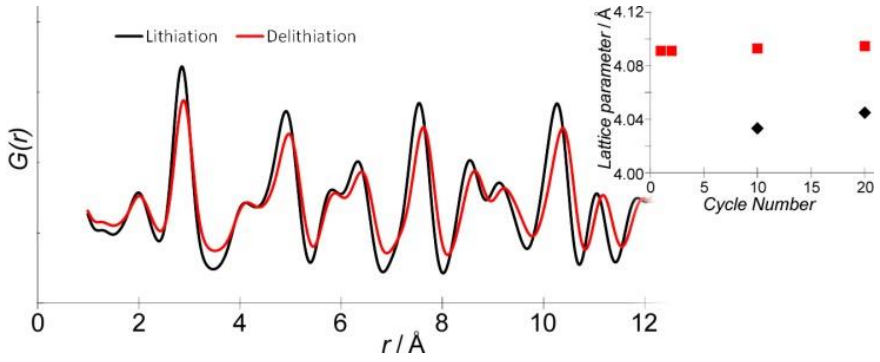

Figure 3.16. PDFs modeled for the LiF rocksalt components for the lithiated and delithiated electrodes showing the larger lattice parameter for this phase during delithiation. The refined lattice parameters for these phases are inset.

Two approaches were used to estimate the level of Fe substitution/insertion within the LiF: based on refinement of the structural model against the PDF; and based

on the lattice expansion. In the PDF modeling, constraining the atomic displacement parameters for Li and F to the values refined for the lithiated state (and Fe to a reasonable value), *x* refined to 0.5 for $Fe_xLi_{2-x}F_2$. Although Vegard's law does not directly apply (as no rocksalt FeF_2 phase exists), assuming a linear relationship between the lattice volumes for pure rocksalt LiF and rutile-type FeF_2, the lattice dimensions refined for $Fe_xLi_{2-x}F_2$ correspond to $x \sim 0.4$. Although each approach has limitations, the similarity in the suggested levels of Fe substitution supports the existence of the Fe-substituted LiF rock salt phase $Fe_xLi_{2-x}F_2$.

Similar "normal" and expanded rocksalt-type LiF phases were observed upon lithiation and delithiation of FeF_3 suggesting that the Fe substituted $Fe_xLi_{2-x}F_2$ phase is also involved in the FeF_3 delithiation reaction as a precursor to the formation of its defective rutile formation described below. That the same lattice parameter is observed for $Fe_xLi_{2-x}F_2$ in both delithiated FeF_3 and delithiated FeF_2 suggests that this may represent the maximum substitution of Fe into LiF.

For the case of FeF_3 delithiation leads to the formation of a defective rutile structure. Based on our PITT results, composition changes are extremely small for each multiphasic reactions. Such phase evolution is supported by the multiple pathway defect rutile delithiation evolution proposed through first principles and also supported in part by characterization. [54] [72] [29] [90] In particular, Yamakawa et al. showed evidence of a sequential delithiation and formation of a rutile phase with lithium incorporation and iron oxidation state increasing with the state of charge. [72]

FeOF presents interesting behavior upon lithiation. As opposed to the known conversion reaction of FeF_2 and FeF_3, we have a known reaction of (3) representing P=4. [31] [75] [76] Similar to the delithiation reactions observed in the FeF_2 case, the lithiation reaction during the conversion reaction occurs in steps of minimal but not insignificant constant potential range. This may be related to nanometer oxygen gradients in the $FeO_{0.67}F_{1.33}$ phase utilized in this research or conversion phases of limited composition represented by (3). In order to have a constant potential of the four phase reaction in (3), i.e. F = 0, the number of components will have to be 4. Li, Fe, and F are required as independent components due to their mobility to form the LiF and Fe phases. Treating the rutile LiFeOF phase and the oxygen as the final fourth component would be acceptable as the diffusion of the oxygen is unlikely. This scenario leads to F=0 and an invariant potential as a function of composition.

In contrast to scenario (3), scenario (4) consists of P = 3. In this structural evolution, one can treat the LiFeOF as more of a displacement vs. conversion material. Indeed, advanced characterization has yet to observe the conclusive presence of the LiF phase as a result of the conversion process and the phase has only been present under low potentials as a result from the decomposition of the rocksalt phase.[26,28] In this scenario, the rocksalt phase develops as a natural progression from the host rutile phase as lithium inserts into the rutile phase and displaces 0.5 Fe for every Li insertion. In this case, we can count the active components as 3; Li, Fe and the host compound transporting to the rocksalt phase. This scenario also leads to F = 0, a constant potential reaction.

In both scenarios the zero degree of freedom scenario suggest that the entire reaction should proceed as an invariant reaction. In contrast, the potential is observed to change with small degrees of constant potential with $\Delta x << 0.1$. This could be explained in the same manner as the delithiation reactions where in this case the rock salt phase has limited degrees of stable phase composition before the transformation to the next step.

$$Li^+ + LiFeOF \rightarrow LiF + 0.5Fe + LiFe_{0.5}O \quad (3)$$

$$Li^+ + LiFeOF \rightarrow 0.5Fe + Li_2Fe_{0.5}OF \quad (4)$$

If the above specified metal fluoride electrode reactions evolve a series of limited solubility multiphase reactions in near equilibrium multi month measurements, it is highly likely that most of these phases are not evolved during practical cycling rates. At such rates, the voltage induced by kinetic polarization will be such that near final phase compositions will be approached directly. This presents scenarios where reaction rates may dictate phase and morphology evolution which then may influence ultimate electrochemical performance.

3.4.2 Hysteresis

The discussion above presents strong electrochemical evidence that a contrast in conversion reaction mechanism exists between the lithiation and delithiation reaction for the pure fluorides. This contrast in pathways manifests itself as an asymmetric intrinsic hysteresis. The contrast in mechanism between lithiation and delithiation also

presents itself as a significant difference in the delta of the reaction potential between the lithiation and delithiation reaction relative to the thermodynamic potential of the reaction as defined by the Gibb's free energy of formation. FeF_2 is the only material which we have appropriate thermodynamic free energy of formation, a potential of 2.66 V vs Li/Li^+. For the lithiation reaction of (1), the hysteresis relative to the thermodynamic reaction potential is much greater than the multistep reaction of delithiation.

Ideally, the reaction path of an electrode material would be completely symmetric to induce minimal intrinsic hysteresis. Quantitative evidence for this can be found in the comparison of the 1.3 V hysteresis of the conversion regions of FeF_2 and FeF_3 vs. 0.7 V for $FeO_{0.67}F_{1.33}$ established under C/1000 reverse step PITT. The significant difference in observed hysteresis is consistent with the conversion reaction mechanisms discussed above. All the materials undergo multiple phase reactions with many changes in composition during delithiation. The pure fluorides present a single multiphase conversion reaction which goes to near completion during lithiation. Only the lithiation of $FeO_{0.67}F_{1.33}$ presents electrochemical evidence of a similar reaction mechanism during lithiation as delithiation consistent with significant decrease in hysteresis.

3.4.3 Transport

The diffusion coefficients for all the conversion reactions were found to be in the range of $1 - 5 \times 10^{-18}$ cm^2/s. Although small, these diffusion values extracted over small composition perturbation techniques such as PITT and EIS are in excellent agreement with the times of diffusion typically observed during the macro length discharge of the

fluorides. Specifically, it has been shown by Badway and later by Liao that reaction (particle) length scales must be < 20 nm to achieve effective utilization of iron fluorides through the conversion reaction. [30] [90] Applying the Einstein equation to the calculated diffusion coefficient of 4.0×10^{-18} cm^2/s derived by PITT for FeF_2 realizes a diffusion distance of 7.6 nm at a C/20 rate very consistent with a particle of 20nm size with at least 2 sided diffusion access.

Most importantly, transport must be discussed in context to the conversion reaction. As opposed to a straight forward topotactic lithium insertion/deinsertion involving the mobility of Li^+ exclusively, the conversion reaction is dependent on the mobility of other species, namely Fe^{2+} or F^- as discussed in detail in the subject matter above. The mobility of these species is expected to be very slow, but effective over small spatial dimensions. As such, they will exist as the limiting factor in phase front mobility and the effective diffusion coefficient which should obviously be not attributed solely to the Li^+ ion.

3.5 *Conclusions*

High resolution PITT of 10 mV steps to C/1000 current was found effective to isolate the true hysteresis of FeF_2, FeF_3, and $FeO_{0.67}F_{1.33}$ compounds relative to simple kinetically induced polarization. Reverse step PITT studies were used to remove effects induced by nucleation overpotential. Clear electrochemical evidence was seen for a significant asymmetry in lithiation/delithiation conversion reaction mechanisms for FeF_2 and FeF_3 while more symmetry was revealed for $FeO_{0.67}F_{1.33}$. This translated to similar

hysteresis for FeF_2 and FeF_3 while $FeO_{0.67}F_{1.33}$ realized a significant reduction in hysteresis. This result strengthened the argument of reaction pathway asymmetry as the origin of kinetically unresolved hysteresis in conversion materials. Diffusion studies for the three materials realized similar low diffusion coefficients on the order of 1×10^{-18} cm^2/sec, a value consistent with the required 20 nm to support a practical electrode reaction. High resolution PITT leads to new insights regarding the conversion reaction mechanisms. In one example, the reconversion process during delithiation reveal electrochemical and structural evidence of a $Fe_xLi_{2-2x}F_2$ rocksalt precursor forming prior to the reformation of FeF_2 rutile. The reaction was consistent with a multistep delithiation process observed within the PITT data.

4 Electronic Transport in Lithiated Iron and Bismuth Fluoride

4.1 *Introduction*

Lithium-ion batteries are the ubiquitous energy storage device for portable electronics. Historically, there has been a continuous quest for higher energy density chemistries in order to reduce the weight or volume in new innovative devices. Lithium conversion compounds are one of the promising alternatives for battery positive electrodes. [91] The advantage is their ability to accommodate more than one lithium/electron per transition metal to achieve higher capacities than traditional intercalation compounds. Transition metal fluoride conversion materials have been a research focus because their highly ionic bonds allow reduction potentials approximately 1 V higher than the chalcogenides. [29] [30] [32] [92] As such, high capacity, low cost metal fluorides such as FeF_2, FeF_3 and CuF_2 are of interest. FeF_2 has been extensively investigated as a potential electrode material due to its potential low cost and rutile structure which is common among the first row metal fluorides. [34] [35] [93] The latter aspect makes it an excellent model material for fundamental studies. FeF_2 exhibits a single three phase reaction, $FeF_2 + 2Li^+ + 2e^- \rightarrow Fe + 2\ LiF$, exhibiting a theoretical capacity of 571 mAh/g. During lithiation, most conversion materials of fluoride and dichacodenide chemistries form a bi-continuous network of nano metal and lithium salt (i.e. LiF, Li_2O, etc.). This has been shown in a number of high resolution transmission electron microscopy studies and supported in part by molecular dynamic modeling. [35] [94] Although such networks visually appear to be electronic percolating (Figure 4.1) and may be the pathway for electron transport to the reaction front, there

has been no data to suggest what order of magnitude the conductivity of this percolated network is. The goal of the effort presented herein is to establish quantitatively the electronic conductivity of the percolated network. Two conversion materials were investigated in this chapter, FeF_2 and a contrasting conversion electrode, BiF_3. [61] Even though BiF_3 can have up to 3 electron transfer per mole, the heavy weight of Bi yields a theoretical capacity of 302 mAh/g. However, its dense structure allows a high volumetric energy density of 7170 Wh/l. Its conversion reaction takes place around 3 V and has shown to have high rate capabilities. [61] The establishment of an electronic percolating pathway is of importance to establish effective electron transfer from the cell to the reaction front. In the case of FeF_2, the formation of 2M LiF and 1M Fe results in a nanocomposite of 73.48 volume % of insulating LiF and 26.52 volume % of Fe. The relatively small volume % of Fe presents a challenging composite environment for the establishment of an electronic conducting pathway. Despite this, it is in the realm of volume % required to create a percolating pathway as long as the morphological development is continuous.

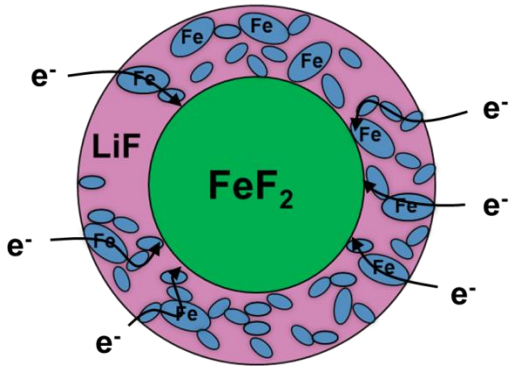

Figure 4.1 Schematic of the LiF – Fe^0 bi-continuous network that is formed during lithiation.

Conductivity of an effective mixed conducting electrode is comprised of both ionic (σ_i) and electronic (σ_e) contributions. Thus, total conductivity is $\sigma_T = \sigma_i + \sigma_e$. In order to measure conductivity, thin film fluoride materials were deposited onto interdigitated electrodes (IDE) and were chemically lithiated with n-butyllithium. Films were also electrochemically lithiated although this approach was not used as the primary investigative tool as lithiation would occur preferentially at the IDE interface and overall would yield an inhomogeneous evolution of converted material. Chemical lithiation can provide a uniform lithiation without any preferential sites. Electrochemical impedance spectroscopy (EIS) was used to obtain total conductivity while direct current (DC) polarization was used to separate any ionic from electronic conductance.

4.2 *Experimental*

4.2.1 Film and sensing electrode fabrication

Two and four electrode titanium IDE arrays were utilized to characterize the electronic conductivity of the initial and converted films. Figure 4.2a is a schematic of a four point probe IDE utilized for FeF_2 thin film to correct for contact resistance. Similar to standard four point probe measurements, current was applied on the outside fingers of the IDE, voltage was measured on the inner fingers. Generally, the FeF_2 films were 400 nm thick deposited on while between IDE electrodes thickness was 250 nm. The conductivity measurements were compared to its two point probe counterpart (Figure 4.2b). In this case, current was measured on the same IDE fingers where the voltage was applied. In contrast to 4-point probe design, 2-point probe consist of a 250 nm IDE with a 100 or 200 nm active film deposited in such that they sit in between the fingers of the IDE.

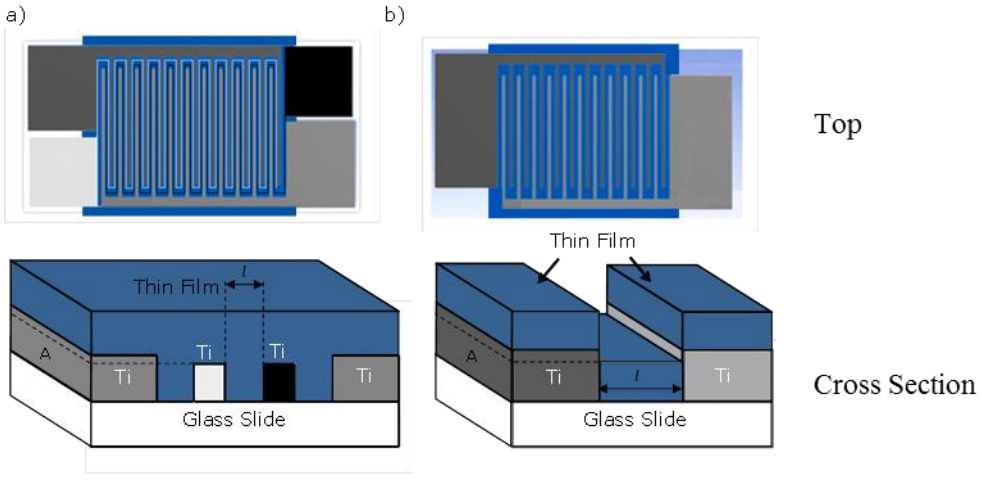

Figure 4.2. Schematic of IDE designs consisting of titanium deposited onto a glass slide with a conductive thin film on top: a) 4-point probe IDE b) 2-point probe IDE.

Ti IDEs were deposited onto glass slides using e-beam vacuum deposition. The glass slides were cleaned with acetone followed by methanol. The slides were then secured to a substrate holder with Kapton tape. The source material, titanium (99.99% Ti granules Alfa Aesar), was packed in a graphite crucible. Both the glass slides and the source material were placed in the deposition chamber and the chamber was brought down to 10^{-6} torr. Ti IDEs were deposited onto the glass slides using a mask and the chamber was then vented with nitrogen gas followed by dry air. The glass slides was removed from the chamber and stored in a glovebox under an inert gas before depositing the active film.

FeF_2 was also deposited using the e-beam deposition. Beforehand, FeF_2 (Advance Research Chemicals) was dried for 4 h at 288 °C in an argon filled tube furnace to remove any moisture. IDEs were attached to a substrate holder using Kapton tape along with a single blank slide, the latter was used for determination of deposited film thickness by profilometry. Strips of aluminum were used to mask the tabs of the IDE to keep them free from iron fluoride during deposition. The substrate holder and dried FeF_2 were placed in the deposition chamber. FeF_2 was deposited onto the slides after reaching ideal pressure. Afterwards, the slides were taken out and stored in the glovebox.

BiF_3 was deposited using thermal evaporation. BiF_3 (Advance Research Chemicals) was dried also in a tube furnace under argon at 260 °C for 2 h. Blank IDE slides along with BiF_3 were transferred to a high vacuum thermal evaporator coater in a

glovebox under argon. IDE slides along with a blank slide were placed in the evaporator chamber and held in place with a substrate cover to protect the tabs of the IDEs. The chamber was place under vacuum and the source material was deposited onto the IDEs. Slides were then removed and transferred back in the glovebox without any exposure to ambient air.

A basic 2-electrode (Figure 4.3) was also fabricated to compare with IDE measurement. In this case, the fluoride or base metal material was deposited first onto the glass slide using thermal evaporation. Afterwards, Au tabs were deposited by thermal evaporation through shadow mask deposition.

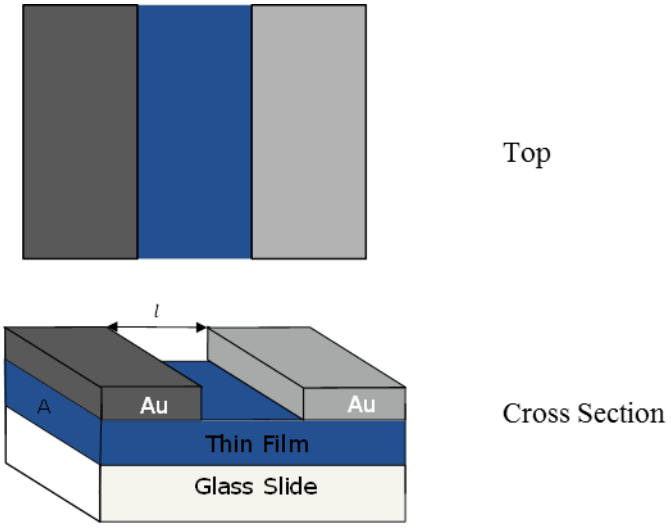

Figure 4.3. Illustration of a basic 2-electrode design also utilized for conductivity measurements.

Films were chemically lithiated with a 2.5M solution of n-butyllithium in hexane (Sigma-Aldrich). (Caution: N-butyllithium will react violently when exposed to water and air). Chemical lithiation was safely performed in a glovebox under argon. N-butyllithium

has a reducing power of 1 V vs. Li/Li^+ which is sufficient enough to reduce both FeF_2 and BiF_3 to their base metals. The films were soaked in the solution from 2 weeks up to 3 months to allow sufficient time for the n-butyllithium to fully convert the film. Films were then removed and excess reducing solution was rinsed off using hexanes (anhydrous, 95% Sigma-Aldrich) and placed under vacuum for 15 mins to evaporate any remaining hexane from the film. Afterwards, they were removed and rinse again with dimethyl carbonate (DMC, Novolyte) and placed back under vacuum for an additional 15 mins. In addition to the chemical lithiation, one of the IDE was electrochemically lithiated using an in-situ cell. The cell was assembled with the IDE as the positive electrode and lithium metal as the negative electrode with two glass fiber separators soaked with 1M $LiPF_6$ ethylene carbonate: dimethyl carbonate (EC:DMC) between them. The cell was then discharged at a constant potential of 1.3 V with a 0.04 mA/g current cut-off to reduce the film. The IDE was then removed from the cell, rinsed off with DMC and placed under vacuum for 15 mins. EIS and DC polarization for both chemically and electrochemically lithiated samples were performed using a Solartron impedance/gain-phase analyzer (SI 1260) equipped with electrochemical interphase (SI 1287). Au probe leads that connected the samples to the Solartron outside the glovebox so that measurements can be conducted while samples remained in an inert atmosphere.

4.2.2 Physical characterization

The thickness of the deposited films was measured using a Vecco Dektak 150 stylus profilometer. The glass slide has a smooth surface which provides a near zero reference point for measurements. The thickness of the titanium IDE digits were also

measured before the deposition of the active materials. The thickness of the film was determined by measuring the film deposited on the blank glass slide. Four points were measured and an average thickness was calculated.

Cross sections of the 2-point probe IDE samples were prepared by ion cross polishing using a JEOL Cross Section Polisher. Samples were then evaluated under a field emission scanning electron microscope (FESEM) by Zeiss (Model 8100) to confirm the IDE profile and film thicknesses. Bruker D8 Advance was used for X-ray diffraction (XRD) using CuKα radiation as the source. Samples were protected from the environment by using a mild barrier of Kapton which was sealed to the substrate before removal from the glovebox. Films were scanned before chemical lithiation to confirm the structure of the material deposited and provide a baseline of the material amount. Lithiated samples were scanned again and phases were identified using Eva software. Both Eva and Topas Rietveld analysis software were used to quantify the composition of the lithiated samples.

DC polarization was performed at 2 different sets of voltage potentials, (2, 20 mV) and (20, 200 mV). Films were polarized for 10 h with a 3 h rest at open circuit. After polarizing the films for 10 h, the decayed current was deemed to be purely electronic. The measured current was used to find the resistance which was utilized in the conductivity calculations. Impedance was also measured before and after each polarization from 2 MHz to 0.1 Hz with a 20 and 200 mV amplitude. Both EIS and DC

polarization were first performed at lower potentials and then samples were allowed at least a 12 h rest period before subjecting them to higher potentials.

During DC polarization, ions are blocked at the electrode while electrons are free to flow freely, resulting in decay in the current. Conductivity was calculated using the following equation:

$$\rho = (RA)/l \quad \textbf{(4.1)}$$

R is the resistance, A is contact surface area, l is length between the contact area and ρ is the resistivity. Conductivity (σ) can be found by taking the inverse of ρ. In the 2-electrode case, the contact surface area is the product of the thickness of the film and the length of the tab, and *l* is the distance between the two contact tabs (Figure 4.3). Initially for the IDEs, the surface area was determined as the thickness of the film by the contact length of the digits of the IDE times the number of digits. The length was the distance between the digits (Figure 4.2). However, results indicated that the films were so highly conductive that electrons would ignore the IDE circuit and effectively act as a basic 2-electrode setup. For this assumption, the IDE film was subdivided into parts and an equivalent circuit was fabricated, as shown in Figure 3.4 for 2-point probe IDE. R_a and R_e are the resistance of the IDE tabs where there is no film on top. R_b, R_c and R_d are the resistances where the thin film has been deposited on top of the IDE. R_b and R_d are subdivided into parts, $R_{b,2}$ and $R_{d,2}$ are areas where part of the IDE tabs contain a thin film coating on top, $R_{b,1}$, $R_{b,3}$, $R_{d,1}$, and $R_{d,3}$ are parts that is only the thin film. R_c is also

subdivided into several parts, $R_{c,1}$ and $R_{c,7}$ are parts which contain only the thin film outside the IDE area. $R_{c,2}$ and $R_{c,6}$ are the rails of the IDE. $R_{c,3}$ and $R_{c,5}$ are the portion between the rail of one side of the IDE to the edge of the digits for the other. $R_{c,4}$ contain the digits from both sides of the IDE and the space in between. Because of symmetry, the equivalent circuit can be reduced such that the total measured resistance, $R_T = 2\,R_a + 2\,R_b + R_c$ and $\frac{1}{R_c} = \frac{2}{R_{c,1}} + \frac{2}{R_{c,2}} + \frac{2}{R_{c,3}} + \frac{1}{R_{c,4}}$. In areas where the film is on top of the IDE, it can be treated as 2 resistors in a parallel circuit and total resistance is determined by their thickness and conductivities. The conductivity of Ti was found using 4-point probe while the thickness of IDE and thin film was determined from profilometry. Thus, the conductivity of the film can be determined by the measured resistance. In addition, assuming that during chemical lithiation conversion progresses down into the bulk uniformly, the thickness can be corrected by the percentage of the lithiated phase based on XRD analysis.

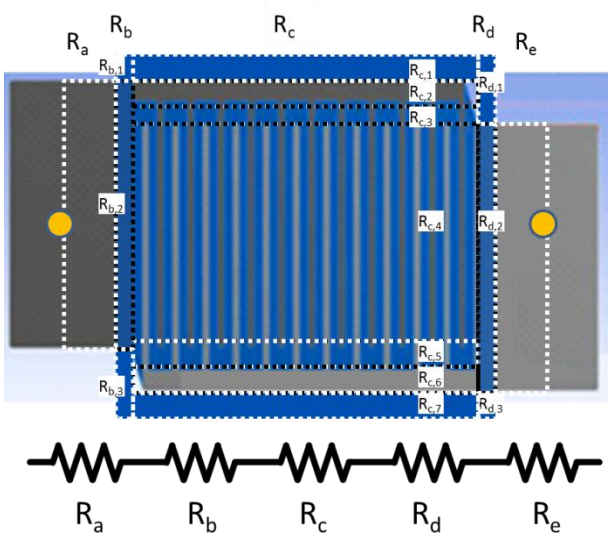

Figure 4.4. Equivalent circuit used for conductivity calculations for 2-point probe IDE. R_b, R_c, and R_d contain smaller sections of the IDE that are in parallel with each other. Placement of the Au probes is shown as circles.

4.3 *Results*

Conductivity measurements of deposited thin film Fe and Bi metals were used as a benchmark to compare to the conductivities of the metal – LiF matrices that are formed from chemically lithiated metal fluorides. As listed in Table 4.1, while Fe^0 and Bi^0 have a theoretical conductivity value of 1.04×10^5 and 7.75×10^3 S/cm respectively, our deposited thin film metals generally exhibit 5 or 10 times less than theoretical. This would be consistent with the polycrystalline nature of the films. [95] [96] [97] Both DC polarization and EIS show similar results to that obtained with 2-electrode probes. The conductivity values also agree with measurements from 4-point probe being within the same order of magnitude.

Sample material	Theoretical metal conductivity (S/cm)	4-point probe (S/cm)	2-electrode (Polarization, EIS) (S/cm)
Fe^0	1.04×10^5	1.45×10^4	(3.58×10^4, 3.58×10^4)
Bi^0	7.75×10^3	1.73×10^3	(1.39×10^3, 1.39×10^3)

Table 4.1. Theoretical and measured conductivity of Fe and Bi thin film metals. Conductivity measurements shown were taken using 4 point probe at 2 mA, 2-electrode polarization at 20 mV and through EIS.

4.3.1 FeF_2

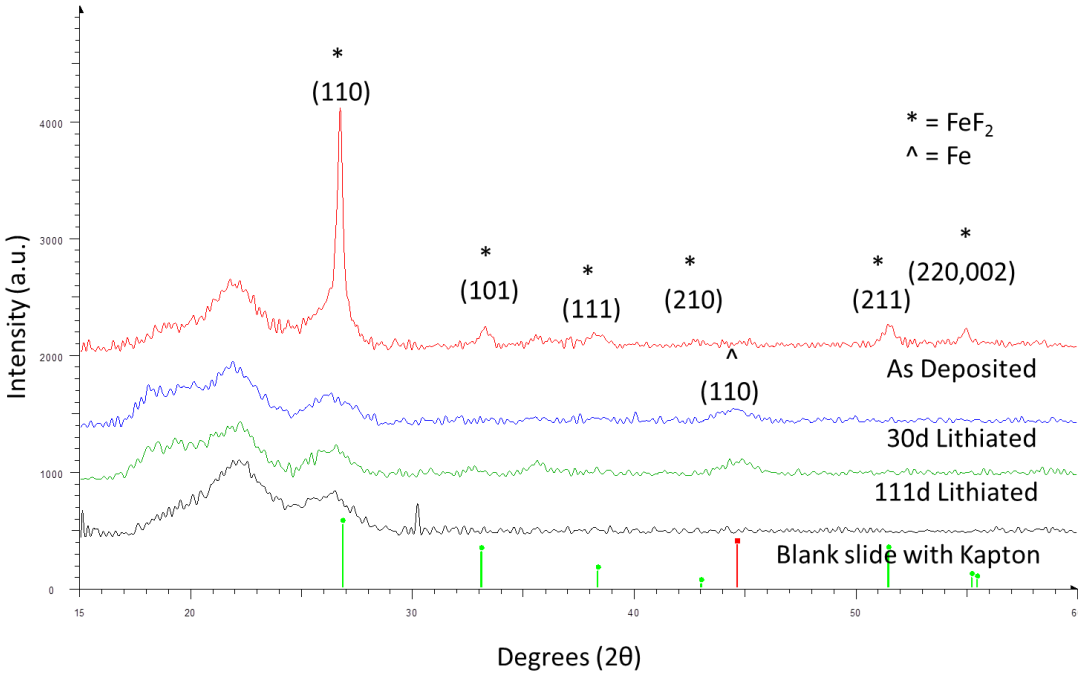

Figure 4.5. XRD scan of FeF_2 IDE after chemical lithiation.

Figure 4.5 shows the XRD pattern of the films after they have been lithiated and compared to the initial film and blank slide. After 30 days, the majority of the FeF_2 film

had reduced to Fe^0. The broad peaks at 22° and 27° relate to the Kapton barrier and are not FeF_2 peaks. The broad Fe^0 Bragg reflections relate to a crystallite size of 9.9 nm base from Scherrer formula. There is little evidence of crystalline LiF. Relative to the Fe scattering factor, LiF is expected to be considerably smaller, of low peak intensity and high peak breadth consistent with a crystallite size <10 nm, so crystalline evidence by XRD is not expected for the thin film. However, LiF is present in a conventionally cast thicker, increased x-ray scattering intensity, electrode of FeF_2 which has been chemically lithiated. It indicates that there is little propensity for the selective dissolution of LiF in the n-butyllithium and hexanes.

Initially, all conductivity measurements were performed with IDEs as we believed the conductivity would be much lower than what we measured. As such, the increased surface area offered by the IDE arrangement would have been highly beneficial. Surprisingly, the results indicated that the Fe – 2 LiF matrix has a very high conductance on the order of the IDE electrode itself. As such, the electrons would divert from the IDE pattern and travel through the converted film to the opposite electrode. Thus, corrections to the IDE calculations to account for the conductivity of the electrodes themselves were applied as described previously. The conductivity results were comparable with subsequent films of a simple two Au electrode configuration which were also fabricated (Table 4.2). Table 4.2 shows very good consistency in conductivity results regardless of the configuration (IDE vs. 2-electrode), sensing electrode (Au vs. Ti), lithiation days (11 - 111), DC polarization voltage (2, 20, or 200 mV), or characterization technique (EIS vs. DC polarization). There was an increase in conductivity for the 111 day

lithiated sample. Most likely the extended time allowed n-butyllithium to penetrate further into the film increasing the conductance of the film. Using the aforementioned geometric corrections, 4 point probe IDE conductivity measurements resulted in a conductivity of 1.23 S/cm for the fully lithiated film, a conductivity value consistent with the three other approaches. In short, all results span within a relatively high $1 – 8 \times 10^{0}$ S/cm range of conductivity. Films were also lithiated electrochemically vs. lithium and presented in Table 4.2 as a contrasting benchmark. In this case, FeF_2 shows a decrease in conductivity by approximately one order of magnitude relative to all the chemically lithiated samples. We believe this is due to considerable resistance caused by the catalytic cathodic decomposition of the cyclic carbonates to form an extensive solid electrolyte interphase. [98]

Thickness (nm)	Polarization Voltage (mV)	# Days Lithiated	Conductivity (Polarization, EIS) (S/cm)
E-beam deposition FeF_2/Ti IDE			
209	2	30	(2.24, 1.73)
209	20	30	(1.56, 1.64)
209	20	111	(5.46, 8.81)
209	200	111	(5.22, 5.46)
209	20	Electrochemical	(4.26×10^{-1}, 3.53×10^{-1})
209	200	Electrochemical	(3.42×10^{-1}, 3.43×10^{-1})
Thermal evaporation FeF_2/Au 2 electrode			
98	20	11	(2.11, 1.49)
98	200	11	(1.57, 1.57)
264	20	11	(1.06, 1.15)
264	200	11	(8.55×10^{-1}, 1.14)

Table 4.2. Electronic conductivity measurements for lithiated FeF_2. Films were chemically lithiated using n-butyllithium. A 209 nm film was electrochemically lithiated to 1.3 V vs. Li/Li^+.

4.3.2 BiF_3

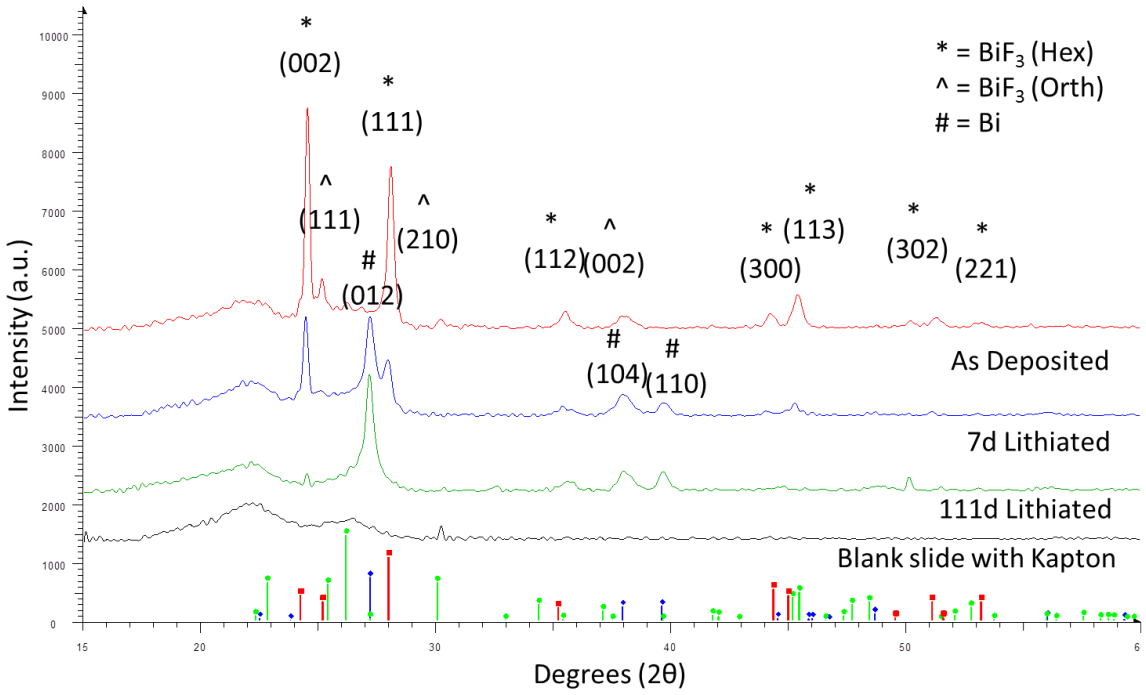

Figure 4.6. XRD scan of BiF_3 IDE after chemical lithiation.

XRD results revealed two polymorphs of BiF_3 phases are formed from deposition: hexagonal tysonite ($P\bar{3}c1$) and orthorhombic phase (Pnma) (Figure 4.6). After 7 days of chemical lithiation the orthorhombic BiF_3 disappears and reduce to Bi metal. Even though majority of the tysonite phase has converted, a small quantity remains. After 111 days, the majority of the film has been reduced. As with FeF_2, there is no evidence of LiF peaks in the XRD pattern as it may be nano-size so that it is lost in the background noise. In fact, LiF has been noted as being absent by XRD of macro electrode converted materials, yet present by TEM analysis. [99] Similar to FeF_2, chemical lithiation of thicker cast electrode resulted in LiF and Bi^0. However it should be noted that Li_3Bi was also found to be present in the thicker electrodes well. Even though the reduction of Bi^0 to

Li_3Bi occurs at a low potential (0.82 V), the direct reduction from BiF_3 to Li_3Bi occurs at 1.01 V which is just above the reduction potential of n-butyllithium, as shown in Table 4.3. The chemical reaction is as follows:

$$6\ LiC_4H_9 + BiF_3 \rightarrow Li_3Bi + 3\ LiF + 3\ C_8H_{18} \qquad \textbf{(4.2)}$$

This reduction pathway would be active if the conversion rate to Bi^0 is slow. In this case, the direct conversion of BiF_3 to the Li – Bi alloy would take place. It seems this is not the case for the thin films as there is no XRD evidence of the Li – Bi alloy was shown to develop. This may be due to the increased kinetics of the reaction afforded by the thin film structure allowing a sequential conversion of the BiF_3 to Bi followed by the alloy formation.

Chemical Reaction	Δε (V)	ΔG (@ 25 °C) (kJ/mol)
$3\ Li + Bi \longrightarrow Li_3Bi$ [100] [101]	0.8216	-237.839
$Li + F \longrightarrow LiF$ [102]	6.09	-587.7
$BiF_3 + Li \longrightarrow Bi + 3\ LiF$ [53]	3.21	-929.15
$Bi + 3\ F \longrightarrow BiF_3$	2.881	-833.949
$8\ C + 9\ H_2 \longrightarrow\ C_8H_{18}$	0.206	-357.274
$Li + \frac{1}{2}\ C_8H_{18} \longrightarrow LiC_4H_9$ [53] [103]	1	-96.485
$3\ LiC_4H_9 + BiF_3 \longrightarrow LiF + Bi + \frac{3}{2}\ C_8H_{18}$	2.21	-638.252
$6\ LiC_4H_9 + BiF_3 \longrightarrow 3\ LiF + Li_3Bi + 3\ C_8H_{18}$	1.015	-587.98

Table 4.3. List of chemical reaction formulas and Gibb's free energy of formation.

The Bi^0 that is formed from chemical conversion of the BiF_3 is highly conductive, as such, corrections needed to be made for conductivity measurements based on the

IDE designs. As the correction used for FeF_2 is in agreement with other techniques, the same correction methodology was utilized for BiF_3. The results (Table 4.4) were relatively consistent with a conductivity of 5 – 9 x 10^{-1} S/cm which is approximately 3 orders of magnitude below that of the base metal. The sample that was lithiated for only 7 days revealed a conductivity that was one order of magnitude higher in polarization than in EIS. XRD revealed this sample had an incomplete chemical conversion of 60% (Figure 4.6).

Thickness (nm)	Polarization Voltage (mV)	# Days Lithiated	Conductivity (Polarization, EIS) (S/cm)
Thermal evaporation BiF_3/ Ti IDE			
128	2	7	(9.72, 9.17 x 10^{-1})
128	20	7	(6.24, 7.93 x 10^{-1})
224	20	111	(8.37 x 10^{-1}, 8.97 x 10^{-1})
224	200	111	(5.35 x 10^{-1}, 5.44 x 10^{-1})

Table 4.4. Conductivity measurement for lithiated BiF_3. Films were chemically lithiated with n-butyllithium.

4.4 *Discussion*

The electronic conductivity measurements for both the FeF_2 and BiF_3 converted nanocomposites reveal that the percolated metal network maintains a very high electronic conductivity on the order of 1 - 10 S/cm. For both cases, the values are approximately three orders of magnitude less than the deposited pure metal control films suggesting the formation of a similar percolated network for both elements. From a percolation perspective, conductivity increases by a power law:

$$\sigma = (x - x_c)^{\mu} \quad \textbf{(4.3)}$$

μ is a critical exponent which is 1.30 for two-dimensional percolation and 2.00 for three-dimensional percolation. x_c is the critical volume fraction such that when the volume fraction (x) is below x_c the material is insulating. [56] Above x_c, metal clusters are interconnected to allow electron transport. The value for μ is also highly dependent on the morphology of the percolating composite components and details of the interconnections. Abeles et al. studied percolation in W – Al_2O_3 metal films where W is the conductive particulates in an insulating Al_2O_3 matrix. [104] Unannealed films contained grains less than 2 nm and vary in size after annealing. The critical volume fraction was found to be 0.47 and conductivity varies from completely insulating to 10^5 S/cm. However near x_c, conductivity could be between 10^2 – 10^{-3}, a 5 order magnitude difference. Although somewhat similar in metal size of W – Al_2O_3 composites FeF_2 and BiF_3 forms an unique electrochemically derived 3-D percolated network of 1 - 2 nm metal – LiF during lithiation with strong evidence of a textured relationship among all the metal nanocrystallites within a single composite domain. Therefore, its critical volume fraction would likely be lower than W – Al_2O_3.

Material	% volume metal	% volume LiF
Fe + 2 LiF (FeF_2)	26.52	73.48
Fe + 3 LiF (FeF_3)	19.40	80.60
Bi + 3 LiF (BiF_3)	41.94	58.06

Table 4.5. Volume percent in converted FeF2, FeF3, and BiF3.

Table 4.5 is the calculated volume percent of metal and LiF in converted FeF_2, FeF_3, and BiF_3. The volume fraction of Fe in LiF is x = 26.52% for FeF_2. It is possible that the measured conductivity in converted FeF_2 is near x_c as it is 3 orders of magnitude away from its pure metal counterpart characterized in the same manner. When compared to theoretical conductivity of Fe metal, FeF_2 is 4 orders of magnitude away. Increasing the fluorine content, as in the case of FeF_3, the volume percent of metal formed from conversion is 19.40%. We can deduce that electronic conductivity would be lower than FeF_2. This is supported by the fact that the rate capability of FeF_3 conversion is considerable less than FeF_2 even though the lithium diffusion is similar. [29] In the case for BiF_3, its conductivity is also 3 orders of magnitude away from deposited Bi metal and 3.5 orders of magnitude away from Bi metal's theoretical value. In addition, BiF_3 has a higher ratio of converted Bi metal to LiF than with the FeF_2. Thus, x is may be further away from x_c and closer to pure Bi metal.

The impact of the high electronic conductivity is represented in the extreme case of thin films with a vertical morphology which requires the electron to diffuse through a large distance >700 nm while the ion diffusion distance <100 nm. In such films we have shown [34] that the electronic conductivity is high enough to maintain facile electrochemical activity, well beyond the 20 nm thought by us and others to be necessary. This suggests that the majority of the challenge related to improving the viability of metal fluoride conversion materials rests in the improvement of the ionic transport as long as contact to the percolation network is maintained throughout the cycling of the metal fluoride conversion material. Indeed, the diffusion of lithium has

been found to be quite low. [35] This may be quite important in guiding future research directions.

The intricate beauty of the percolated network formed in-situ by the process of conversion is clearly driven by a continuous requirement to have an electron transfer at the reaction front. The fact that the percolated pathway is somewhat epitaxial in nature may also improve the electronic conductivity due the lack of defined grain boundaries. The web of nano metal may make such converted composites useful for other applications such as catalysis with effective salt removal or exchange. However, this structure clearly reveals a daunting challenge to replicate for those who wish to fabricate x LiF + Me nanocomposites, i.e. metal fluorides in their prelithiated state for use in nonlithium containing lithium batteries. Finally, the conclusions presented here hold true for the lithiation reaction of the metal fluorides, the delithiation reaction results in a metal fluoride reformed on the surface, bringing forth additional questions regarding the role of electronic transport.

4.5 *Conclusion*

Chemically lithiated FeF_2 and BiF_3 were found to form highly conductive metal nanocomposites of Fe – 2LiF and Bi – 3LiF, respectively. Conductivity for the FeF_2 and BiF_3 converted products were found to be 1 – 8 S/cm and 5 – 9 x 10^{-1} S/cm respectively. Percolation theory suggests that FeF_2 is near its critical volume fraction to allow conductivity and BiF_3 is further away from its critical threshold as conductivity is closer to Bi metal. Even though the conductivity of these converted fluorides is lower than

their pure metals by three orders of magnitude, it is clearly high enough to support significant electronic transport to the reaction front throughout the chemical or electrochemically initiated conversion process during the lithiation reaction.

5 Tracking Gradient Diffusion in Thin Film FeF_2

5.1 *Introduction*

With the rise of portable electronics, there has been a greater demand on the energy storage that powers these devices. Large-scale devices, such as electrical vehicles seek for alternative energy storage with higher capacity at a fraction of the weight. [105] Current Li-ion batteries contain intercalation positive electrodes with high cyclability with minimal structural change. However, only a fraction of their potential capacity could be fully utilized. [106] On the other hand, conversion electrodes can have four times the capacity of traditional intercalation materials by using all of the metal cation's oxidation states. Metal fluorides such as iron fluoride (FeF_2) have shown as a possible material for next generation batteries. [30] [34] [35] As with other metal fluoride materials, FeF_2 has a high reduction potential (E=2.66 V) because of ionic metal–fluorine bond and has the potential of being low cost. The reaction mechanism for FeF_2 as follows: $FeF_2 + 2Li^+ + 2e^- \rightarrow Fe + 2\ LiF$. As both Li-ions and electrons need to be present in order for the reaction to proceed, it is imperative that we have both good electronic and ionic transport. Previous studies have indicated the formation of Fe network in a LiF matrix. [33] Recently, we have shown that this metal network can support electron transport to the reaction front during lithiation. [107] Previous electrochemical diffusion measurements show FeF_2 having a diffusion coefficient of $1x\ 10^{-18}\ cm^2/s$. during lithiation. [35] Conductivity and diffusion are related to each other through the Nerst-Einstein equation:

$$\frac{\sigma_i}{D_i} = \frac{nq^2}{kT} \quad \textbf{(5.1)}$$

σ_i and D_i are conductivity and diffusion coefficient of the mobile species i, n is number density, q is elementary charge, k Boltzmann's constant, and T is temperature. The mobility of electrons is much greater than Li-ions, we assume that lithiation is dependent on Li-ions transport to the reaction front. In this study, we investigate the ionic transport of Li-ion in FeF_2 by chemical lithiation to better understand the limiting factor in the conversion process. A tracer method is used to calculated diffusion.

In tracer diffusion, if assume 1-dimentional diffusion, a layer of radioactive isotope is put on the surface of the material. The surface of the material has a fix concentration and is held constant throughout the experiment. As time progress, the isotopes will diffuse into the bulk material (Figure 5.1a). The diffusion length, x, at a certain concentration can be determined by the amount of time that has elapsed in the relationship:

$$x \approx \sqrt{Dt} \quad \textbf{(5.2)}$$

x is a measurement of the depth of diffusion, t increases by ½ as x increases. This can be applied to a thin sold film with various thicknesses, as less time is required for the mobile species to diffuse through a thin film and more time for a thicker one. Diffusion coefficient can be either determined by the time to diffuse through the film of a known thickness or the difference in diffusion time between different thicknesses. A gradient

thin film of FeF_2 is chemically lithiated to determine ionic transport. Because of the conductive Fe network that is formed during lithiation, we can measure reaction front movement from the resistance between regions. The diffusion of Li-ions is determined by drop in resistance of the film throughout the experiment and their differences between different regions (Figure 5.1b).

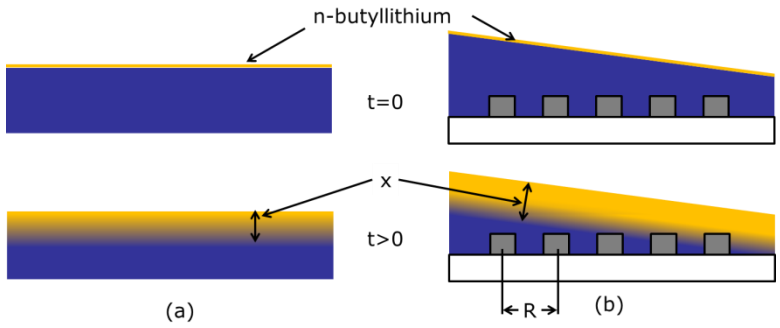

Figure 5.1. 1-dimensional diffusion in a) a simple bar, b) film with a gradient thickness. The concentration at x=0 remains constant during diffusion.

5.2 *Experimental*

In order to find ionic diffusion, a gradient thin film is fabricated with line probes underneath to measure resistance (Figure 5.2). 2 sets of 6 Titanium (Ti) line sensing electrode probes that evenly spaced between each other are deposited onto a glass slide using e-beam vacuum deposition. At each end of the Ti line probe is a square tab that will connect to a scanning digital multimeter. Each probe is spaced 4.5 mm apart from each other and both sets have a 11.65 mm gap between them. Generally, these probes are 50nm thick and are chemically inert during lithiation. Resistance is measured between each probe during chemical lithiation. On top is a gradient film of FeF_2 which was also deposited with an e-beam using glancing angle deposition technique (GLAD).

The difference in thickness from one side to the other can range from 150-250 nm. To prevent the diffusion of Li-ions from the side which can distort results, probes were place in the center of the film and lines do not extend to the edge of the glass slide. The time for Li-ions to diffuse through the sides will take longer than diffusion from the top surface down to the probes. M. Parkinson et al. have shown to form 3-dimensional (3-D) FeF_2 textured films using GLAD by sweeping between various angles. [34]In addition, they have also produced dense films by static deposition.

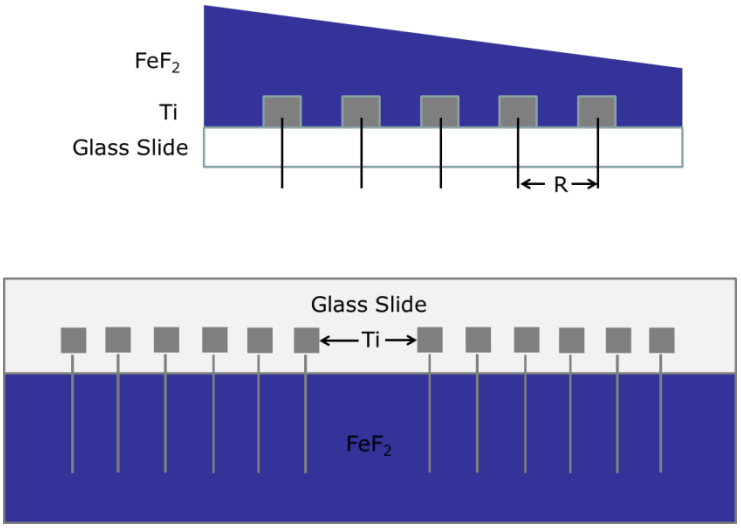

Figure 5.2. Schematic of FeF_2 gradient film. A total of 12 Ti line probes are evenly spaced out on the glass slide with the exception of the 6th and 7th probe where there is a larger gap. Resistance is measured between Ti line probes

The same custom e-beam deposition unit and source material will be used to produce our gradient films. Beforehand, glass slides were cleaned with acetone and then methanol. They were then place onto a substrate holder and secured with Kapton tape. A brass line mask is placed over the glass slide with Kapton tape and the substrate holder is placed in the vacuum chamber at 0°, parallel to the base of the chamber

(Figure 5.3a) . The source material, titanium (99.99% Ti granules Alfa Aesar), was packed in a graphite crucible and is also placed in the vacuum chamber. The chamber was brought down to 3 x 10^{-6} torr and Ti was deposited onto the glass slides. Afterwards, the chamber was vented with nitrogen and then dry air. The substrate holder was removed from the chamber and the mask was removed from the glass slide. The glass slides are stored in a glovebox under an inert atmosphere (argon) before depositing FeF_2

FeF_2 was also deposited using e-beam deposition. Beforehand, FeF_2 powder (Advance Research Center) was dried in a tube furnace under Ar gas at 288 °C for 4 hours to remove any moisture. The Ti line glass slides were remove from the glovebox and placed on the substrate holder along with two clean blank glass slides and secured with Kapton tape. Strips of aluminum were used to mask the Ti tabs. Another strip was used to cover a portion of the of the blank glass slide which would be used later to determine the thickness by profilometry. The substrate holder was placed in the vacuum chamber and set to 60° from the base (Figure 5.3b). The dried FeF_2 was also packed into the crucible and place in the vacuum chamber. The chamber was brought down to pressure and FeF_2 is deposited onto the glass slides. Because of the angle of the substrate holder, the side closest to the source material will become thicker than the side furthest away. After deposition, the chamber was vented and the glass slides are removed and place in a glovebox.

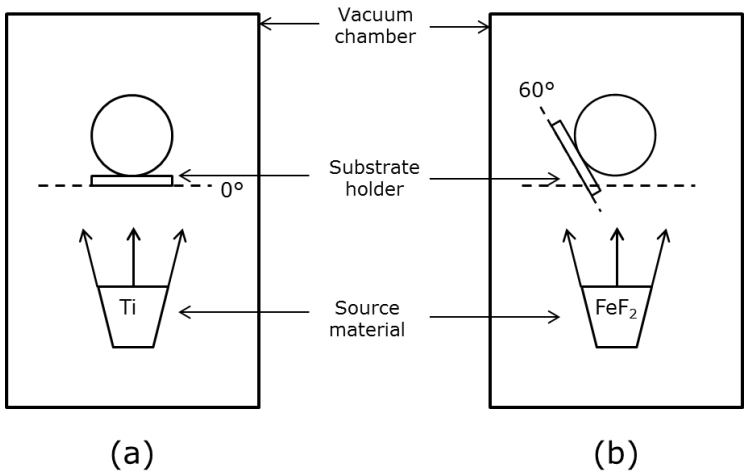

Figure 5.3. Illustration of the position of the substrate holder during the deposition of: (a) Ti, (b) FeF_2.

A Vecco Dektak 150 stylus profilometer was used to determine the thickness of the films. The glass slide has a smooth surface which would be used as a near zero reference point for our measurements. The thickness of the Ti lines was taken before they were put into the chamber for FeF_2 deposition. Four points were measured and the thickness was averaged. The blank slide that had a portion masked out from deposition was used to determine the thickness of FeF_2. Since the film has a gradient thickness, specific measurements were taken where the Ti lines would have been underneath.

Films were chemically lithiated with a 2.5M solution of n-butyllithium in hexane (Sigma-Aldrich). It has a reduction potential of 1 V which will reduce FeF_2 into Fe-metal and LiF. N-butyllithium is reactive when exposed to air and water so chemical lithiation was performed in a glovebox under an inert atmosphere. A custom holder was made to measure the resistance of the probe during chemical lithiation, shown in Figure 5.4. A well is drilled into a Teflon block which will hold both the glass slide and n-butyllithium.

Small holes are drilled on the side which line up with the tabs of the Ti lines. A glass fiber board is fitted with 12 individual gold probes which will connect to the Ti tabs (not shown). Before the glass slide is put into the Teflon holder, the holder is filled with n-butyllithium. It is filled to the point that when the glass slide is put into the holder, the n-butyllithium level is lower than the FeF_2 film line. This is to prevent side diffusion and essentially shorting out all the probes at the same time. The butyllithium is checked with a black glass slide and used to compare with the level of the film. Afterwards the glass slide is placed in and the top is covered with a glass fiber plate and is held in place with two screws.

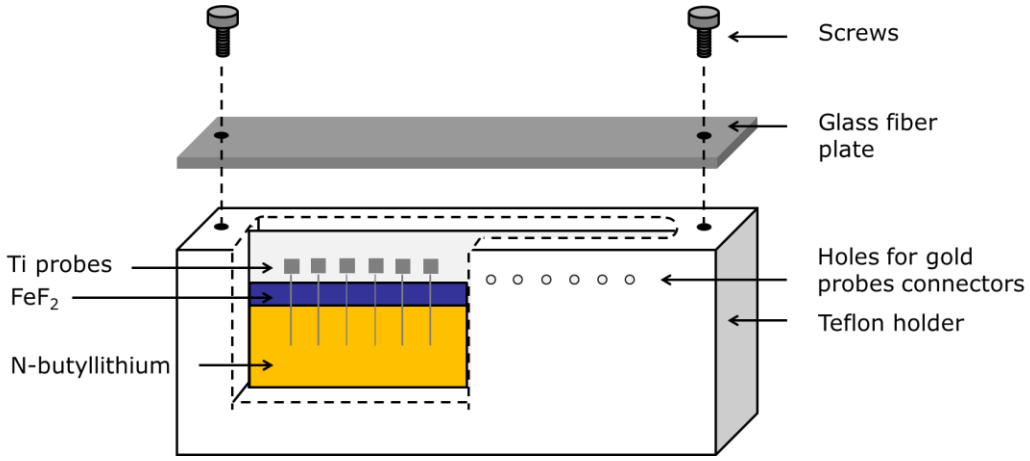

Figure 5.4. Illustration of the glass slide holder used for chemical lithiation.

A 34970A (Agilent) Data Acquisition/Switch Unit coupled with a 34901A 20 Channel Multiplexer (2/4-wire) Module is used to determine the resistance between the probes. The gold pins that connect to each probe leads to the switch unit outside of the glovebox. Each individual probes are labeled from (1) – (12) where (1) has a thinner film

of FeF_2 and (12) has a thicker film of FeF_2. Resistance was taken between each probe every 10 seconds. A total of 11 resistance measurements for each pair of probes ((1-2), (2-3), (3-4),…, (11-12)). Conductivity (σ) can be calculated from resistance using the following equation:

$$\sigma = \frac{1}{R}\frac{l}{ax} \tag{5.3}$$

R is the resistance, l is the distance between the two probes, a is the length of the Ti line that has been exposed to butyllithium and x is the thickness of the film. Because the angle of the thickness gradient is very small (<0.005°), we can assume that the diffusion length is the same as the thickness penetrated. We can substitute eq. (5.2) into (5.3) to get:

$$\sigma = \frac{1}{R}\frac{l}{a\sqrt{Dt}} \tag{5.4}$$

Taking the log of both sides and rearranging the equation we have:

$$\log(R) = -\frac{1}{2}log(t) + \frac{1}{2}log\left(\frac{l^2}{a^2 D\sigma^2}\right) \tag{5.5}$$

We can determine the diffusion coefficient for individual probe sets by plotting the linear region of logarithmic resistance and time and determining the time to fully

convert. The conductivity of a fully lithiated film is assumed to be 1 S/cm based off of previous electronic measurements. [107] The lithiation times were compared to each other and were plotted in thickness vs time$^{1/2}$ and the diffusion coefficient was extracted from the fitted slope.

X-ray diffraction (XRD) was used to verify the composition of the film before and after lithiation. Glass slides were placed in a Bruker D8 Advance diffractometer with CuKα as the source. After lithiation, the glass slide was rinsed with hexanes (anhydrous, 95% Sigma-Aldrich) to remove any remaining salt and then put under vacuum for 15 mins. Afterwards, it is rinsed again with dimethyl carbonate (DMC, Novolyte) and put under vacuum for an additional 15 mins. For both lithiated and pre-lithiated samples, a film of Kapton was placed on top of the slides and sealed with grease while the glass slides were still in the glovebox. This is to protect the film from the environment during XRD scan. Phases were identified using Eva software.

5.3 *Results*

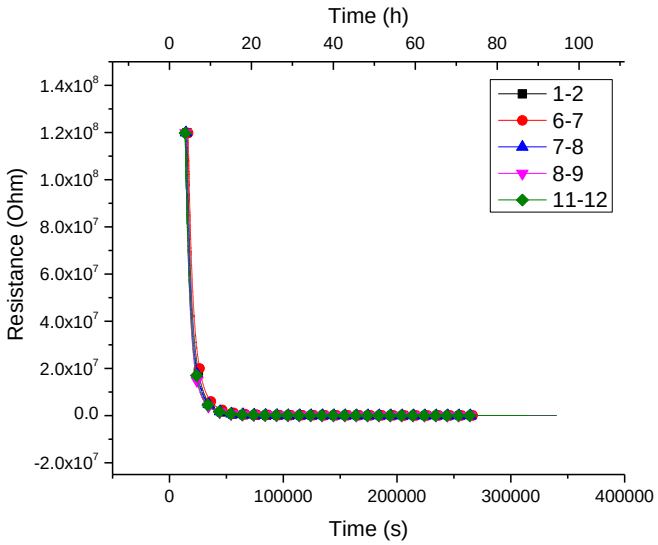

Figure 5.5. Resistance profile of gradient film.

As the gradient glass slide is placed into the holder, the film is uniformly exposed to n-butyllithium. Both thin and thick region of the film are exposed simultaneously and in the same fashion which makes them comparable to each other. Figure 5.5 is the resistance plotted as a function of time for a representative pairs of probes. Some of the probes are not shown because of excessive noise in the data. Generally, all the probes have similar resistance profiles despite the difference in thicknesses. As n-butyllithium interacts with the film and initiates the chemically reduction, we do not detect any measurable resistance at all the probes until t is approximately 4 h where we first detect 1.2 x 10^2 gigaohms (Gohms). Afterwards, their resistance dropped from 1.2 x 10^2 Gohms down to 5 Gohms after 10 hours. After 27 h, the resistance continued to decrease but at a slower rate. This same resistance trend has been seen across with multiple films.

Though there is no confirmation, we assume that with enough time, the resistance would continue to drop until a finite value above zero equating to the intrinsic electronic conductivity enabled by the formation of a complete percolated nanocomposite between the probes. The resistance of thicker regions would have a lower resistance than thinner films as there would be a greater thickness of conductive composite to allow transport of the electrons.

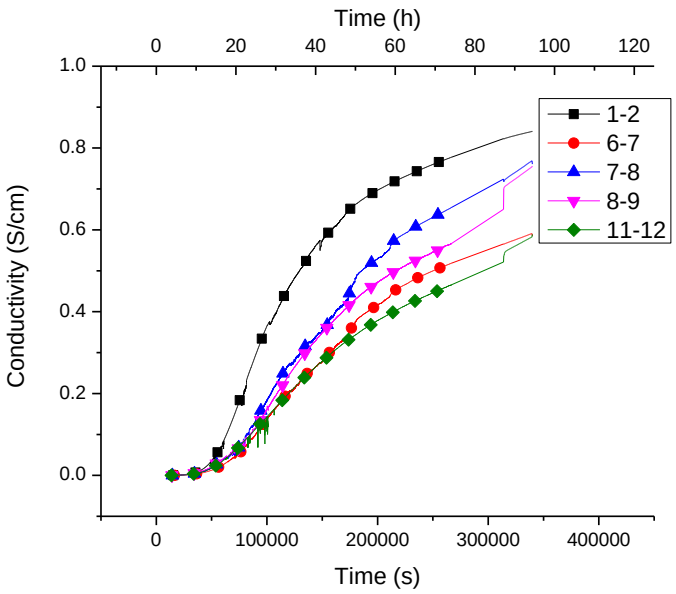

Figure 5.6. Plot of the overall increase in conductivity as n-butyllithium percolates further into the film.

When the probe sets are plotted in terms of conductivity (Figure 5.6), the overall conductivity increases over time. After 90 h of lithiation, conductivity of the probes was greater than 0.5 S/cm and continues to increase. This is within 1 order of magnitude when compared with results from electrochemical impedance spectroscopy (EIS) and direct current (DC) polarization results. [107] After 60 h, the conductivity for the entire

probe sets, with the exception of (1-2), increases nearly the same rate. This is more clearly seen in Figure 5.7a of a log-log graph of resistance vs. time, as the slopes for the individual plots after log(t) = 5.25 become parallel to each other. The diffusion coefficient is determined by fitting this linear portion of the graph as shown in Figure 5.7b for probe 7-8. Table 5.1 list the diffusion coefficients calculated for each probe set. All the probe sets with the exception of (1-2) have a diffusion coefficient of 10^{-20} cm^2/s. The fitted slope was also used to estimate the time to full lithiation. Their times and respective thicknesses were plotted on a thickness vs. $time^{1/2}$ shown in Figure 5.8. Since the plot show a difference in diffusion time from different diffusion length, by fitting the slope of the plot we determined the diffusion coefficient using eq. (5.2). The diffusion coefficient from the fitted line was 10^{-21} cm^2/s. In both cases, the diffusion coefficient found with the thin film was slower than PITT and EIS studies (10^{-18} and 10^{-19} cm^2/s respectively). [35]

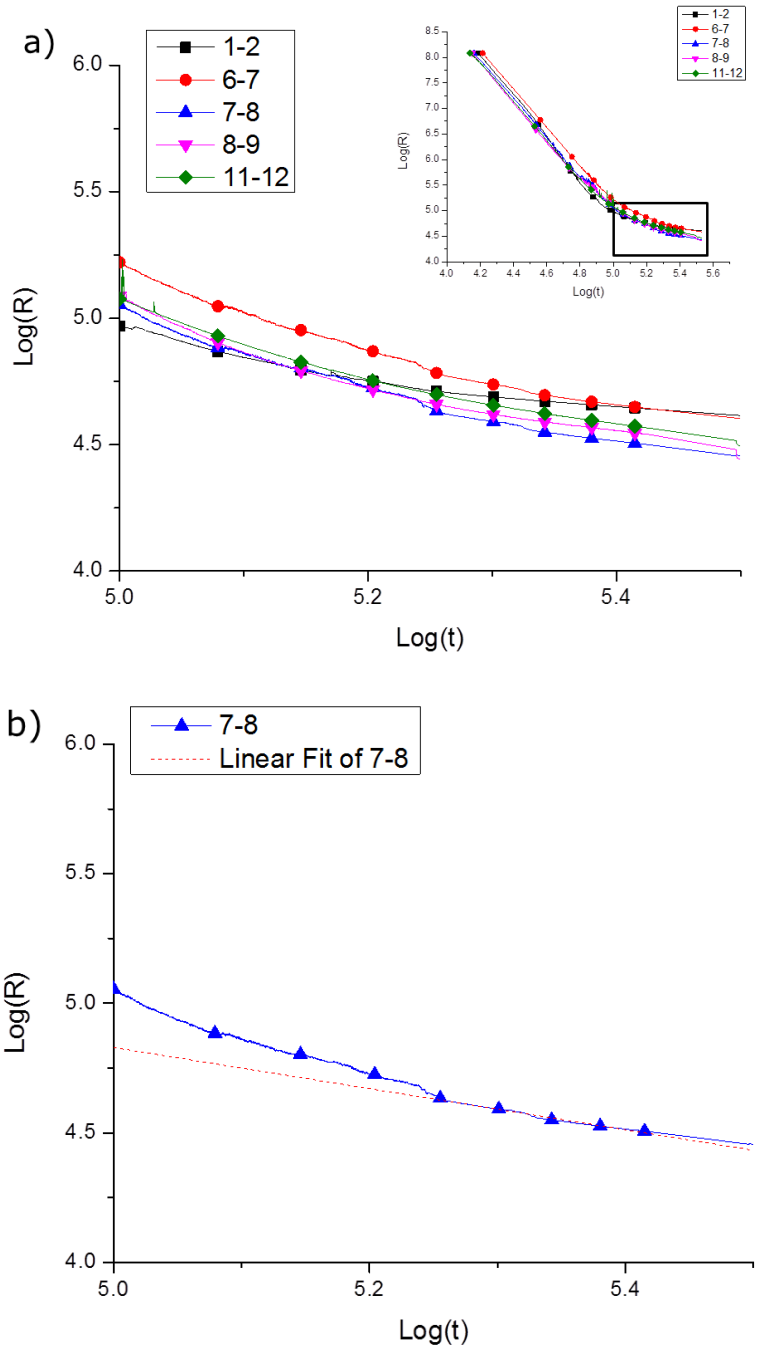

Figure 5.7. (a) Log(R) vs log(t) plot for individual probe sets. The diffusion coefficient for each probe set was determined by the fitting the linear region as shown in (b).

Probe	Thickness (nm)	Diffusion Coefficient (cm^2/s)
1-2	124.9	1.7134×10^{-22}
2-3	135.53	-
3-4	146.17	-
4-5	156.8	-
5-6	167.43	-
6-7	186.51	2.9839×10^{-20}
7-8	205.59	1.2114×10^{-20}
8-9	216.22	8.4604×10^{-20}
9-10	226.85	-
10-11	237.49	-
11-12	248.12	5.51×10^{-20}

Table 5.1. Individual diffusion coefficient calculations for each probe pairs. Some pairs are not shown because of noisy data.

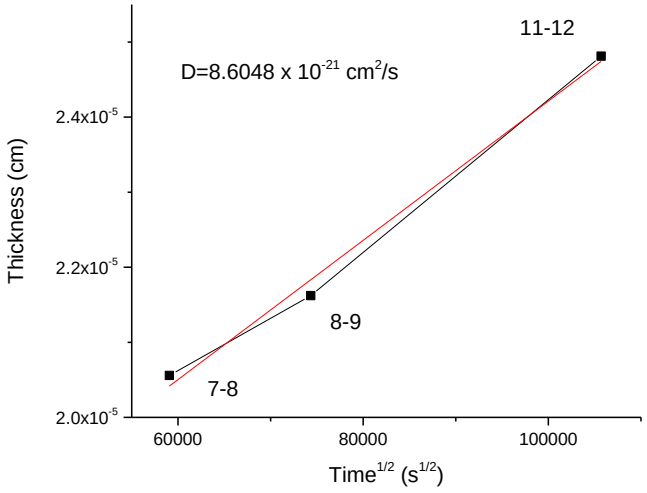

Figure 5.8. Plot of probe pairs in sequence and their fitted time to complete lithiation. The fitted slope was used to determine the diffusion coefficient: 8.6048×10^{-21} cm^2/s.

5.4 *Discussion*

The electrochemical techniques utilized to extract the diffusion coefficients of the reduction reaction in FeF_2 in PITT are based on localized relaxation of nonequilibrium conditions for the case of PITT and slightly longer diffusion distances for the low frequency reactions extracted from the Wardburg diffusion in EIS. In contrast, the gradient technique herein bases the diffusion calculation on much larger scale transport passing through the micro and mesoscale. This requires transport through various morphological features such as film defects, incoherent domain boundaries, etc. These can cumulate to decrease the diffusion coefficient. Previous studies have shown that FeF_2 forms 10 - 30 nm nanocomposites when milled with carbon which allowed it to become electrochemically active. [18]This allows a smaller diffusion length for Li-ions to penetrate through, 5 - 15 nm diffusion length for two sides. In the gradient film, Li-ions have to diffuse through 200 nm of dense FeF_2 from only one side. Perhaps the diffusion rate at a larger scale is significantly slower than smaller scale that it can affect its electrochemical performance. This has been seen with Badway et al. as capacity increases as a function of milling time. [30]

The initial decrease in resistance follows a much higher order relationship (-4.5 vs. -0.5) than the square relationship we expect for an ion diffusion process. This is possibly related to the precipitous decrease in conductivity as the two sensing electrodes become “wired” with a percolation path as the reaction front becomes in

proximity with the sensing electrodes. Afterwards the reaction front proceeds further down in between the electrodes. At this point the front moves forward in a relationship with time that is very close to the square relationship we expect.

As a final note, it should be reinforced that the diffusion number extracted represents the movement of the reaction front. As the conversion reaction is a reconstructive event, it is not solely representative of the transport of the Li^+ but of other species such as Fe^{2+} and F^-.

5.5 *Conclusion*

Gradient films of FeF_2 were used to determine the movement of the reaction front by controlled chemical lithiation. Because of the conductive Fe – 2 LiF matrix that is formed during lithiation, the diffusion of n-butyllithium can be tracked using sensing electrodes. The diffusion coefficient was found to be 10^{-20} cm^2/s for individual probe sets, 10^{-21} cm^2/s when plotted in sequence. The difference in values when compared with PITT and EIS may be from the different methodologies. In addition morphological features found in thin films may also affect values as diffusion is passing through both the micro and mesoscale.

6 Future work

This research has presented several new opportunities for study. Though they were not covered in the thesis, as they would have been outside the focus of the project and/or would require additional time and finances.

In chapter 3, ionic transport in these iron-based fluorides. It would be interesting to see calculated diffusion coefficients with other conversion fluorides such as BiF_3 where they have excellent rate capabilities. One would expect their values to be higher than iron-base fluorides. As it has been indicated before, ionic transport is slower than electronic because of the percolated network that is formed during lithiation. Improvements to ion mobility may be lead to improvements in cycling rates.

Though the percolated network is formed during first lithiation, it is unclear if this structure is maintained from multiple cycles. Conductivity should be measured at different cycle numbers to see if the high electronic transport changes.

Temperature is another factor not considered and should be pursued. If ion mobility is the root cause of the different reaction mechanism, there should be an investigation on how temperature may change the reaction pathway these conversion materials take. By changing the reaction pathway we can effectively reduce hysteresis. As mention previous, hysteresis is common in conversion materials. Reverse step PITT could be applied to those materials to eliminate any nucleation induced overpotential to find their true hysteresis.

Results from chapter 4 and 5 promoted more interest in thicker films. As indicated before, near theoretical capacities of these fluoride materials until made into nanocomposites. Further study into these materials to see if transport scale linearly with thickness. In addition, longer times for chemical lithiation would be needed to fully lithiated these films. For line gradient films, it would be beneficial to show that conductivity between the probes plateau. With thinner films, not only would reduce the time to complete lithiation but would also give diffusion coefficient value comparable to that found with PITT and EIS.

Though it was shown in chapter 4, Li_3Bi seemed to form when a thicker electrode was chemically lithiated. This was not shown to be present in any of the thin films. Fourier transform infrared spectroscopy (FTIR) may be able to reveal its presence. If so, thin films should be repeated with a different reducing agent with a slightly higher reduction potential, perhaps LiI in Acetonitrile with a reduction potential of 2.79 V vs. Li. [108] [109]

7 Summary

In this thesis, we have used various techniques to identify intrinsic properties of iron-base fluorides and related back to their electrochemical performances. Using high resolution PITT studies, we were able to extract out diffusion coefficients to gain a sense of the slow moving reaction front. When compared to EIS results they were found to be within 1 order of magnitude. These voltage steps are small and held for long times (10 mV with 0.4 mA/g cut-off), the reaction mechanism were identifiable during lithiation and delithiation. FeF_2 and FeF_3 clearly showed asymmetry reaction mechanisms in the voltage profile. FeOF have been shown to be more symmetrical indicating a similar reaction mechanism. Reverse step PITT not only removed polarization from hysteresis, it was able to give a more accurate reaction hysteresis by eliminating nucleation induced overpotentials. Results is in agreement of that asymmetrical intrinsic hysteresis is formed from the difference reaction pathways from lithiation and delithiation. PDF analysis shows that there is Fe insertion into LiF structure before the formation of FeF_2 during delithiation.

Electronic conductivity of the percolated Fe – 2 LiF matrix revealed surprisingly high conductance (1 - 8 S/cm). This allows electrons to transfer to the reaction front through the Fe network that is formed during lithiation. It indicates that the limitation is not electronic transport but rather ion mobility. Percolation theory suggests that these FeF_2 is near its critical volume fraction to allow conductivity. It is expected that the conductivity in FeF_3 would be lower because of the decrease in Fe content.

Utilizing the conductive percolated structure, we were able to determine the reaction front movement through a tracer type method. Diffusion is determined by the drop in resistance that is sensed between the line electrodes in the film. The difference in ionic transport between electrochemical and chemical studies may be linked to transport through the micro and mesoscale level.

8 References

[1] J. M. Tarascon and M. Armand, "Issues and challenges facing rechargeable lithium batteries," *Nature*, vol. 414, pp. 359-367, 2001.

[2] D. Linden and T. B. Reddy, *Handbook of Batteries*, 3rd ed.: McGraw-Hill, 2002.

[3] P. G. Bruce, "Energy storage beyond the horizon: Rechargeable lithium batteries," *Solid State Ionics*, vol. 179, pp. 752-760, 2008.

[4] N. Balsara. [Online]. http://www1.eere.energy.gov/vehiclesandfuels/pdfs/merit_review_2008/exploratory_battery/merit08_balsara.pdf

[5] F. Ding et al., "Dendrite-Free Lithium Deposition via Self-Healing Electrostatic Shield Mechanism," *J. Am. Chem. Soc.*, vol. 135, pp. 4450-4456, 2013.

[6] W. Xu et al., "Lithium metal anodes for rechargeable batteries," *Energy Environ. Sci.*, vol. 7, pp. 513-537, 2014.

[7] G. A. Nazri and G. Pistoia, *Lithium Batteries Science and Technology*.: Springer, 2004.

[8] N. Sonobe, M. Ishikawa, and T. Iwasaki, in *35th Battery Symposium*, Japan, 1994, p. 47.

[9] W. A. Schalkwijk and B. Scrosati, *Advances in Lithium-Ion Batteries*.: Springer, 2002.

[10] I. V. Barsukov, C. S. Johnson, J. E. Doninger, and V. Z. Barsukov, *New Carbon Based Materials for Electrochemical Energy Storage Systems: Batteries, Supercapacitors and Fuel Cells*. Dordrecht, The Netherlands: Springer, 2006.

[11] G. Zheng et al., "Interconnected hollow carbon nanospheres for stable lithium metal anodes," *Nat. Nanotechnol.*, vol. 9, pp. 618-623, 2014.

[12] R. Bouchet, "A stable lithium metal interface," *Nat. Nanotechnol.*, vol. 9, pp. 572-573, 2014.

[13] T. D. Bogart, A. M. Chockla, and B. A. Korgel, "High capacity lithium ion battery anodes of silicon and germanium," *Curr. Opin. Chem. Eng.*, pp. 1-8, 2013.

[14] J. O. Besenhard, *Handbook of Battery Materials*. Weinheim: Wiley-VCH, 1999.

[15] D. Aurbach et al., "Design of electrolyte solutions for Lio and Li-ion batteries: a review," *Electrochim. Acta*, vol. 50, pp. 247-254, 2004.

[16] M. Park, X. Zhang, M. Chung, G. B. Less, and A. M. Sastry, "A review of conduction phenomena in Li-ion batteries," *J. Power Sources*, vol. 195, pp. 7904-7929, 2010.

[17] S. S. Zhang, K. Xu, and T. R. Jow, "Low-temperature performance of Li-ion cells with a LiBF4-based electrolyte," *J. Solid State Electrochem.*, vol. 7, pp. 147-151, 2003.

[18] G. G. Amatucci and N. Pereira, "Fluoride based electrode materials for advanced storage devices," *J. Fluorine Chem.*, vol. 128, pp. 243-262, 2007.

[19] Z. Yang et al., "Electrochemical Energy Storage for Green Grid," *Chem. Rev.*, vol. 111, pp. 3577-3613, 2011.

[20] C. Julien, J. P. Pereira-Ramos, and A. Momchilov, *New Trends in Intercalation Compounds for Energy Storage*., 2002.

[21] D. H. Doughty and A. A. Pesaran, "Vehicle Battery Safety Roadmap Guidance," National Renewable Energy Laboratory, Subcontract Report 2012. [Online]. http://www.nrel.gov/docs/fy13osti/54404.pdf

[22] M. M. Thackeray, "Spinel Electrodes for Lithium Batteries," *J. Am. Ceram. Soc.*, vol. 82, no. 12, pp. 3347-3354, 1999.

[23] G. G. Amatucci et al., "Materials' effects on the elevated and room temperature performance of C/LiMn2O4 Li-ion batteries," *J. Power Sources*, vol. 69, pp. 11-25, 1997.

[24] Y. Xia, Y. Zhou, and A. Yoshio, "Capacity Fading on Cycling of 4 V Li/LIMn2O4 Cells," *J. Electrochem Soc.*, vol. 144, no. 8, p. 2593, 1997.

[25] M. M. Thackeray et al., "Structural Fatigue in Spinel Electrodes in High Voltage (4 V) Li/LixMn2O4 Cells," *Electrochem. Solid State Lett.*, vol. 1, no. 1, pp. 7-9, 1998.

[26] A. K. Padhi, K. S. Nanjundaswamy, and J. B. Goodenough, "Phospho-olivines as Positive-Electrode Materials for Rechargeable Lithium Batteries," *J. Electrochem.*

Soc., vol. 144, no. 4, pp. 1188-1194, 1997.

[27] R. J. Brodd, *Batteries for Sustainability*.: Springer, 2012.

[28] A. J. Gmitter, "The Structural and Electrochemical Dynamics of the Electrode-Electrolyte Interphase of Metal Fluroide Nanocomposite Positive Electrodes for Li Batteries," Rutgers University, PhD Thesis 2012.

[29] F. Badway, N. Pereira, F. Cosandey, and G. G. Amatucci, "Carbon-Metal Fluoride Nanocomposites Structure and Electrochemistry of FeF3:C," *J. Electrochem. Soc.*, vol. 150, no. 9, pp. A1209-A1218, 2003.

[30] F. Badway, F. Cosandey, N. Pereira, and G. G. Amatucci, "Carbon Metal Fluoride Nanocomposites High-Capacity Reversible Metal Fluoride Conversion Materials as Rechargeable Positive Electrodes for Li Batteries," *J. Electrochem. Soc.*, vol. 150, no. 10, pp. A1318-A1327, 2003.

[31] N. Pereira, F. Badway, M. Wartelsky, S. Gunn, and G. G. Amatucci, "Iron Oxyfluorides as High Capacity Cathode Materials for Lithium Batteries," *J. Electrochem. Soc.*, vol. 156, no. 6, pp. A407-A416, 2009.

[32] J. Cabana, L. Monconduit, D. Larcher, and M. R. Palacin, "Beyond Intercalation-Based Li-ion Batteries: The State of the Art and Challenges of Electrode Materials Reacting Through Conversion Reactions," *Adv. Energy Mater.*, vol. 22, pp. E170-E192, 2010.

[33] F. Wang et al., "Conversion Reaction Mechanisms in Lithium Ion Batteries: Study of the Binary Metal Fluoride Electrodes," *J. Am. Chem. Soc.*, vol. 133, pp. 18828-18836, September 2011.

[34] M. F. Parkinson, J. K. Ko, A. Halajko, S. Sanghvi, and G. G. Amatucci, "Effect of Vertically Structured Porosity on Electrochemical Performance of FeF2 Films for Lithium Batteries," *Electrochim. Acta*, vol. 125, no. 10, pp. 71-82, 2014.

[35] J. K. Ko et al., "Transport, Phase Reactions, and Hysteresis of Iron Fluoride and Oxyfluoride Conversion Electrode Materials for Lithium Batteries," *ACS Appl. Mater. Interfaces*, vol. 6, pp. 10858-10869, 2014.

[36] N. Clark and K. Kinoshita, "Zinc/Air Technology December 1993 Meeting Report," 1993.

[37] Energy Storage Association. [Online]. http://energystorage.org/energy-

storage/technologies/redox-flow-batteries

[38] C. K. Park, S. B. Park, H. C. Shin, W. I. Cho, and H. Jang, "Li Ion Diffusivity and Rate Performance of the LiFePO4 Modified by Cr Doping," *Bull. Korean Che. Soc.*, vol. 32, no. 1, pp. 191-195, 2011.

[39] A. J. Bard and L. R. Faulkner, *Electrochemical Methods*, 2nd ed. New York: Wiley, 2001.

[40] Metrohm Autolab. [Online]. http://www.ecochemie.nl/download/Applicationnotes/Autolab_Application_Note_BAT03.pdf

[41] W. Weppner and R. A. Huggins, "Determination of the Kinetic Parameters of Mixed-Conducting Electrodes and Application to the System Li3Sb," *J. Electrochem. Soc.*, vol. 124, no. 10, pp. 1569-1578, October 1977.

[42] C. J. Wen, B. A. Boukamp, R. A. Huggins, and W. Weppner, "Thermodynamic and Mass Transport Properties of "LiAl"," *J. Electrochem. Soc.*, vol. 126, no. 12, pp. 2258-2266, December 1979.

[43] W. Weppner and R. A. Huggins, "Electrochemical Investigation of the Chemical Diffusion, Partial Ionic Conductivities, and Other Kinetic Parameters in Li3Sb and Li3Bi," *J. Solid State Chem.*, vol. 22, pp. 297-308, 1977.

[44] B. C. Han, A. Van der Ven, D. Morgan, and G. Ceder, "Electrochemical modeling of intercalation processes with phase field models," *Electrochim. Acta*, vol. 49, pp. 4691-4699, 2004.

[45] Basics of Electrochemical Impedance Spectroscopy. [Online]. http://www.gamry.com/application-notes/basics-of-electrochemical-impedance-spectroscopy/

[46] C. Ho, I. D. Raistrick, and R. A. Huggins, "Application of A-C Techniques to the Study of Lithium Diffusion in Tungsten Trioxide Thin Films," *J. Electrochem. Soc.*, vol. 127, no. 2, pp. 343-350, 1980.

[47] B. E. Conway and B. V. Tilak, "Interfacial processes involving electrocatalytic evolution and oxidation of H2, and the role of chemisorbed H," *Electrochim. Acta*, vol. 47, pp. 3571-3594, 2002.

[48] Substech. [Online].

http://www.substech.com/dokuwiki/doku.php?id=polarization

[49] G. Brunetti et al., "Confirmation of the Domino-Cascade Model by LiFePO4/FePO4 Precession Electron Diffraction," *Chem. Mater.*, vol. 23, pp. 4515-4524, 2011.

[50] W. Dreyer et al., "The thermodynamic origin of hysteresis in insertion batteries," *Nat. Mater.*, vol. 9, pp. 448-453, May 2010.

[51] A. Ponrouch, J. Cabana, R. Dugas, J. L. Slack, and M. R. Palacin, "Electroanalytical study of the viability of conversion reactions as energy storage mechanisms," *RSC Adv.*, vol. 4, pp. 35988-35996, 2014.

[52] V. L. Chevrier, G. Hautier, S. P. Ong, R. E. Doe, and G. Ceder, "First-principles study of iron oxyfluorides and lithiation of FeOF," *Phys. Rev. B*, vol. 87, pp. 094118-1-9, 2013.

[53] R. E. Doe, K. A. Persson, G. Hautier, and G. Ceder, "First Principles Study of the Li-Bi-F Phase Diagram and Bismuth Fluoride Conversion Reactions with Lithium," *Electrochem. Solid-State Lett.*, vol. 12, no. 7, pp. A125-A128, 2009.

[54] R. E. Doe, K. A. Persson, Y. S. Meng, and G. Ceder, "First-Principles Investigation of the Li-Fe-F Phase Diagram and Equilibrium and Nonequilibrium Conversion Reactions of Iron Fluorides with Lithium," *Chem. Mater.*, vol. 20, pp. 5274-5283, 2008.

[55] A. Bunde and J. W. Kantelhardt, *Diffusion and Conduction in Percolation Systems*. Berlin/Heidelberg: Springer, 2005.

[56] M. Sahimi, *Applications of Percolation Theory*.: CRC Press, 1994.

[57] (2014) WolframAlpha. [Online]. http://www.wolframalpha.com/input/?i=percolation%20theory&lk=2

[58] V. K. Pecharsky and P. Y. Zavalij, *Fundamentals of Powder Diffraction and Structural Characterization of Materials*, 2nd ed. New York: Springer.

[59] P. Poizot, S. Laruelle, S. Grugeon, and J. M. Tarascon, "Rationalization of the Low-Potential Reactivity of 3s-Metal-Based Inorganic Compounds toward Li," *J. Electrochem. Soc.*, vol. 149, no. 9, pp. A1212-A1217, 2002.

[60] F. Badway et al., "Structure and Electrochemistry of Copper Fluoride Nanocomposites Utilizing Mixed Conducting Matrices," *Chem. Mater.*, vol. 19, no.

17, pp. 4129-4141, 2007.

[61] M. Bervas, F. Badway, L. C. Klein, and G. G. Amatucci, "Bismuth Fluoride Nanocomposite as a Positive Electrode Material for Rechargable Lithium Batteries," *Electrochem. Solid-State Lett.*, vol. 8, no. 4, pp. A179-A183, 2005.

[62] J. Moskon, J. Jamnik, and M. Gaberscek, "In depth discussion of selected phenomena associated with intrinsic bettery hysteresis: Battery electrode versus rubber balloons," *Solid State Ionics*, vol. 238, pp. 24-29, 2013.

[63] A. S. Gozdz, C. Schmutz, J. M. Tarascon, and P. Warren, "Polymetric Electrolytic Cell Seperator Membrane," *U.S. Patent 5418091*, 1995.

[64] C. Montella, "Discussion of the potential step method for the determination of the diffusion coefficients of guest species in host materials Part I. Influence of charge transfer kinetics and ohmic potential drop," *J. Electroanal. Chem.*, vol. 518, pp. 61-83, 2002.

[65] M. A. Vorotyntsev, M. D. Levi, and D. Aurbach, "Spatially limited diffusion coupled with ohmic potential drop and/or slow interfacial exchange: a new method to determine the diffusion time constant and external resistance from potential step (PITT) experiments," *J. Electroanal. Chem.*, vol. 572, pp. 299-307, 2004.

[66] P. J. Chupas et al., "Rapid-aquisition pair distribution function (RA-PDF) analysis," *J. Appl. Crystallogr.*, vol. 36, pp. 1342-1347, 2003.

[67] P. J. Chupas, K. W. Chapman, and P. L. Lee, "Applications of an amorphous silicon-based area detector for high-resolution, high-sensitivity and fast time-resolved pair distribution function measurements," *J. Appl. Crystallogr.*, vol. 40, pp. 463-470, 2007.

[68] A. P. Hammersley, S. O. Svensson, M. Hanfland, A. N. Fitch, and D. Hausermann, "Two-Dimensional Detector Software: From Real Detector to Idealised Image or Two-Theta Scan," *High Pressure Res.*, vol. 14, pp. 235-248, 1996.

[69] A. P. Hammersley, "FIT2D: An Introduction and Overview; ESRF internal report ESRF97HA02T," European Synchrotron Research Foundation, Grenoble, France, 1997.

[70] X. Qiu, J. W. Thompson, and S. J. L. Billinge, "PDFgetX2: a GUI-driven program to obtain the pair distribution function from X-ray powder diffraction data," *J. Appl. Crystallogr.*, vol. 37, p. 678, 2004.

[71] C. L. Farrow et al., "PDFfit2 and PDFgui: computer programs for studying nanostructure in crystals," *J. Phys.: Condens. Matter*, vol. 19, p. 33, 2007.

[72] N. Yamakawa, M. Jiang, B. Key, and C. P. Grey, "Identifying the Local Structures Formed during Lithiation of the Conversion Materials, Iron Fluoride, in a Li Ion Battery: A Solid-State NMR, X-ray Diffraction, and Pair Distribution Function Analysis Study," *J. Am. Ceram. Soc.*, vol. 131, pp. 10525-10536, 2009.

[73] K. Xu and C. A. Angell, "High Anodic Stability of a New Electrolyte Solvent: Unsymmetric Noncyclic Aliphatic Sulfone," *J. Electrochem. Soc.*, vol. 145, no. 4, pp. L70-L72, 1998.

[74] P. Liu, J. J. Vajo, J. S. Wang, W. Li, and J. Liu, "Thermodynamics and Kinetics of the Li/FeF3 Reaction by Electrochemical Analysis," *J. Phys. Chem.*, vol. 116, pp. 6467-6473, 2012.

[75] K. M. Wiaderek et al., "Comprehensive Insights into the Structural and Chemical Changes in Mixed-Anion FeOF Electrodes by Using Operando PDF and NMR Spectroscopy," *J. Am. Ceram. Soc.*, vol. 135, pp. 4070-4078, 2013.

[76] F. Cosandey, D. Su, M. Sina, N. Pereira, and G. G. Amatucci, "Fe valence determination and Li elemental distribution in Lithiated FeO0.7F1.3/C nanocomposite battery materials by electron energy loss spectroscopy (EELS)," *Micron*, vol. 43, pp. 22-29, 2012.

[77] M. T. Sougrati, J. C. Jumas, N. Pereira, and G. G. Amatucci, "to be published," 2013.

[78] M. D. Levi, K. Gamolsy, D. Aurbach, U. Heider, and R. Oesten, "Determination of the Li ion chemical diffusion coefficient for the topotactic solid-state reactions occuring via a two-phase or single-phase solid solution pathway," *J. Electroanal. Chem.*, vol. 477, pp. 32-40, 1999.

[79] M. D. Levi, E. Markevich, and D. Aurbach, "Comparison between Cottrell diffusion and moving boundary models for determination of the chemical diffusion coefficients in ion-insertion electrodes," *Electrochim. Acta*, vol. 51, pp. 98-110, 2005.

[80] F. Decker et al., "Li+ Distribution into V2O5 Films resulting from Electrochemical Intercalation Reactions," *J. Braz. Chem. Soc.*, vol. 19, pp. 667-671, 2008.

[81] A. Dell'Era and M. Pasquali, "Comparison between different ways to determine diffusion coefficient and by solving Fick's equation for spherical coordinates," *J.*

Solid State Electrochem., vol. 13, pp. 849-859, 2009.

[82] C. R. Fell, K. J. Carroll, M. Chi, and Y. S. Meng, "Sythesis-Structure-Property Relations in Layered, “Li-excess” Oxides Electrode Materials Li[Li1/3-2x/3NixMn2/3−x/3]O2 (x = 1/3, 1/4, and 1/5).," *J. Electrochem. Soc.*, vol. 157, pp. A1201-A1211, 2010.

[83] M. D. Levi et al., "Solid-State Electrochemical Kinetics of Li-Ion Intercalation into Li1-xCoO2: Simultaneous Application of Electroanalytical Techniques SSCV, PITT, and EIS.," *J. Electrochem. Soc.*, vol. 146, pp. 1279-1289, 1999.

[84] Y. Rho and K. Kanamura, "Li+-Ion Diffusion in LiCoO2 Thin Film Prepared by the Poly(vinylpyrrolidone) Sol−Gel Method," *J. Electrochem. Soc.*, vol. 151, pp. A1406-A1411, 2004.

[85] C. Delacourt, M. Ati, and J. M. Tarascon, "Measurement of Lithium Diffusion Coefficient in LiyFeSO4F," *J. Electrochem. Soc.*, vol. 158, pp. A741-A749, 2011.

[86] J. Li, X. Xiao, F. Yang, M. W. Verbrugge, and Y. Cheng, "Potentiostatic Intermittent Titration Technique for Electrodes Governed by Diffusion and Interfacial Reaction," *J. Phys. Chem. C*, vol. 116, pp. 1472-1478, 2012.

[87] R. A. Huggins, "Principles determining the potentials and capacities of electrochemical cells," *NATO Sci. Ser., 3*, vol. 85, pp. 21-46, 2000.

[88] R. A. Huggins, "Reference electrodes and the Gibbs phase rule," *Solid State Ionics*, vol. 136-137, pp. 1321-1328, 2000.

[89] R. A. Huggins, "The relation between the Gibbs phase rule and reference electrodes," *Ionics*, vol. 4(1 & 2), pp. 129-140, 1998.

[90] P. Liao, J. Li, and J. R. Dahn, "Lithium Intercalation in LiFe2F6 and LiMgFeF6 Disordered Trirutile-Type Phases," *J. Electrochem. Soc.*, vol. 157, pp. A355-A361, 2010.

[91] P. Polzot, S. Laruelle, S. Grugeon, L. Dupont, and J. M. Tarascon, "Nano-sized transition-metal oxides as negative-electrode materials for lithium-ion batteries," *Nature*, vol. 407, pp. 496-499, 2000.

[92] H. Li, G. Richter, and J. Maier, "Reversible Formation and Decomposition of LiF Clusters Using Transition Metal Fluorides as Precursors and Their Application in Rechargeable Li Batteries," *Adv. Mater.*, vol. 15, no. 9, pp. 737-739, 2003.

[93] J. F. Al-Sharab, J. Bentley, F. Badway, G. G. Amatucci, and F. Cosandey, "EELS compositional and valence mapping in iron fluoride-carbon nanocomposites," *J. Nanopart. Res.*, vol. 15, no. 4, pp. 1500/1-1500/12, 2013.

[94] Y. Ma and S. H. Garofalini, "Atomistic Insights into the Conversion Reaction in Iron Fluoride: A Dynamically Adaptive Force Field Approach," *J. Am. Chem. Soc.*, vol. 134, no. 19, pp. 8205-8211, 2012.

[95] I. V. Antonets, L. N. Kotov, S. V. Nekipelov, and Y. A. Golubev, "Nanostructure and Conductivity of Thin Metal Films," *Solid-State Electron.*, vol. 74, pp. 306-309, 2004.

[96] G. I. Frolov, V. S. Zhigalov, A. I. Pol'skii, and V. G. Pozdnyakov, "Investigation of electric conductivity of nanocrystalline cobalt films," *Fiz. Tverd. Tela (S.-Peterburg)*, vol. 38, no. 4, pp. 1208-1213, 1996.

[97] A. F. Mayadas and M. Shatzkes, "Electrical-Resistivity Model for Polycrystalline Films: the Case of Arbitrary Reflection at External Surfaces," *Phys. Rev. B: Condens. Matter Mater. Phys.*, vol. 1, no. 4, pp. 1382-1389, 1970.

[98] A. J. Gmitter et al., "Formation, dynamics, and implication of solid electrolyte interphase in high voltage reversible conversion fluoride nanocomposites," *J. Mater. Chem.*, vol. 20, pp. 4149-4161, 2010.

[99] M Bervas et al., "Investigation of the Lithiation and Delithiation Conversion Mechanisms of Bismuth Fluoride Nanocomposites," *J. Electrochem. Soc.*, vol. 153, no. 4, pp. A799-A808, 2006.

[100] J. Sangster and A. D. Pelton, "The Bi-Li (Bismuth-Lithium) System," *J. Phase Equilib.*, vol. 12, no. 4, pp. 447-450, 1991.

[101] W. Weppner and R. A. Huggins, "Thermodynamic Properties of the Intermetallic Systems Lithium-Antimony and Lithium-Bismuth," *J. Electrochem. Soc.*, pp. 7-14, 1978.

[102] W. M. Haynes, *CRC Handbook of Chemistry and Physics*, 95th ed.: CRC Press, 2014.

[103] A. V. Mischenko and V. E. Fedorov, "Reaction of Cluster Niobium Chalcogenides with n-butyllithium," *Russ. Chem. Bull.*, vol. 36, no. 9, pp. 1789-1790, 1987.

[104] B. Abeles, H. L. Pinch, and J. I. Gittleman, "Percolation Conductivity in W-Al2O3

Granular Metal Films," *Phys. Rev. Lett.*, vol. 35, no. 4, pp. 247-250, 1975.

[105] J. B. Goodenough and Y. Kim, "Challenges for Rechargeable Li Batteries," *Chem. Mater.*, vol. 22, pp. 587-603, 2010.

[106] M. S. Whittingham, "Lithium Batteries and Cathode Materials," *Chem. Rev.*, vol. 104, pp. 4271-4301, 2004.

[107] J. K. Ko, A. Halajko, M. F. Parkinson, and G. G. Amatucci, "Electronic Transport in Lithiated Iron and Bismuth Fluoride," Manuscript submitted for publication.

[108] T. Shiratsuchi, S. Okada, J. Yamaki, S. Yamashita, and T. Nishida, "Cathode performance of olivine-type LiFePO4 synthesized by chemical lithiation," *J. Power Sources*, vol. 173, pp. 979-984, 2007.

[109] W. I. Jung, M. Nagao, C. Pitteloud, A. Yamada, and R. Kanno, "Synthesis of LixMnO2 by chemical lithiation in an aqueous media," *J. Power Sources*, vol. 195, pp. 3328-3332, 2010.